ELECTROPHORETIC DEPOSITION OF POLYMER FUNCTIONALIZED SWNT

THE ELECTROPHORETIC DEPOSITION OF CONJUGATED POLYMER FUNCTIONALIZED CARBON NANOTUBES FOR PHOTOVOLTAIC APPLICATIONS

By TRAVIS CASAGRANDE, B.Eng.Mgt.

A Thesis Submitted to the School of Graduate Studies in Partial Fulfilment of the Requirements for the Degree Master of Applied Science

MASTER OF APPLIED SCIENCE (2011) **McMaster University**
(Materials Science and Engineering) Hamilton, Ontario

TITLE: The Electrophoretic Deposition of Conjugated Polymer Functionalized Carbon Nanotubes for Photovoltaic Applications

AUTHOR: Travis Casagrande, B.Eng.Mgt. (McMaster University)

SUPERVISORS: Professor Gianluigi Botton and Professor Igor Zhitomirsky

PAGES: xiii, 192

Abstract

The experimental research described within this thesis combined the materials of conjugated polymers and carbon nanotubes with the fields of electrophoretic deposition (EPD) and organic solar cells. Prior to these contributions, soluble conjugated polymers and carbon nanotubes that have been functionalized by them had not yet been deposited by EPD from solution or by using non-toxic solvents. Additionally, EPD had not yet been utilized to deposit the active layer in a solid organic photovoltaic device.

The electrophoretic deposition of soluble conjugated polymer functionalized carbon nanotubes from non-toxic solvents was achieved through an iterative process of experimentation and technique refinement. The developed EPD technique utilized the high pH region in the vicinity of the cathode substrate to neutralize positively charged weak polyelectrolyte macromolecules. Their functional groups were protonated using a minimized amount of a weak acid which also enabled their solubility. The deprotonation of the positively charged quaternary ammonium functional groups changed them into neutrally charged tertiary amines which were insoluble in the water-ethanol mixture. This mechanism facilitated the formation of coatings that were predictable and uniform in appearance and thickness.

Control over coating thickness was demonstrated by producing coatings that spanned the range of 100 nm to 10 μm. These coatings were produced by adjusting the applied voltage, solution concentration, and tuning the duration of deposition. Characterization involved scanning electron microscopy, atomic force microscopy, optical profilometry, absorption spectroscopy, and the quartz crystal microbalance.

Techniques for the fabrication of a photovoltaic device using an active layer produced by EPD were established though modifications of general organic photovoltaic device fabrication procedures. These modifications involved the redesign of a photolithographic etching pattern for ITO, the addition of an insulating barrier strip, aluminum electrode layer thickening, and the switch from LiF to BCP for the top buffer layer.

Acknowledgements

I wish to express sincere gratitude to my supervisors Dr. Gianluigi Botton, Dr. Igor Zhitomirsky, and Dr. Alex Adronov for their helpful discussions and advice throughout my experimentation. I am also thankful to have been given the opportunity to participate in their fascinating and innovative fields of research.

The staff at the Canada Center for Electron Microscopy was very helpful in the specimen preparation and characterization work that was conducted within their facilities, and I am especially thankful of Dr. Steve Koprich, Andy Duft, Dr. Glynis de Silveira, and Chris Butcher.

This project would not have been possible without the efforts of Dr. Fuyong Cheng and Patigul Imin to synthesize the polymer material that was central to all my experiments. In addition, I wish to thank them for spending their own time preparing multiple iterations and batches of the polymer when requested.

I am grateful to Dr. Kirill Skupov for his assistance during the adaptation of ITO cleaning and photolithography procedures. I also appreciate the helpful and interesting discussions during the photovoltaic device fabrication and our travels to and from the Xerox Research Center of Canada (XRCC).

The help of Avery Yuen, Nathan Bamsey, and Richard Klenkler from XRCC was essential to enable the photovoltaic device fabrication and testing experiments. I truly appreciate the fact that they took time out of their busy schedules to teach me about their lengthy procedures and did so for nothing in return.

I am thankful to the Natural Sciences and Engineering Research Council of Canada for awarding me with the Postgraduate Scholarship that helped to make this project possible.

Finally, I would like to thank my parents for their continuous support during my many years of study at McMaster University.

Table of Contents

List of Figures

1. Introduction

1.1 Background

One of the most important challenges facing the current and future generations is dealing with climate change by developing strategies to avoid, reduce, and delay its impacts. In their Fourth Assessment Report in 2007, the Intergovernmental Panel on Climate Change, using stronger words than ever before confirmed that "warming of the climate system is unequivocal".[1] Based on the latest culmination of data in climate change research the IPCC concluded "it is extremely likely that human activities have exerted a substantial net warming influence on climate since 1750",[2] and that the largest contribution is from burning fossil fuels.[3]

The effect of the warming is that large-scale climate events will occur and some have the potential to cause very large impacts.[4] However, many of these impacts can be avoided, reduced or delayed by significant reductions in greenhouse gas emissions.[4] A transition to zero or low greenhouse gas emitting technologies is required to achieve this, and it is no longer environmentally sustainable to continue to extract the world's fossil fuels at current rates.[5] While there is not one single best solution to reduce emissions from the energy sector, there are several available options with mass adoption of photovoltaic cells being one of them.[5] This transition to low or zero greenhouse gas emitting power generation technologies is currently limited by high costs, environmental barriers, and social barriers that all restrict growth.[5] More investments into research and development are required to overcome the technical barriers by for example improving efficiency and cost effectiveness of these technologies.[5]

In the case of photovoltaic cells, cost in most applications is a price per performance measure such as dollars per kilowatt, rather than an absolute price. When cost is measured in this form, the two distinctly different ways to improve it are by reducing the absolute price or by improving the photovoltaic efficiency which increases the power generated.

Recent updates in the solar cell efficiency records show 25% power conversion efficiency for traditional p-n junction single crystal silicon wafer photovoltaic cells.[6] The maximum possible efficiency for the p-n junction photovoltaic cell is approximately 31%, which is commonly known today as the Shockley-Queisser limit.[7] There is not much more room for major improvement in the efficiency of this design so significant cost improvements will have to come from a reduction in materials and processing costs.

Rapidly increasing growth of the solar cell market has resulted in a supply shortage of solar grade silicon, which has driven up its price.[8] This puts into question the ability for silicon wafer solar cells to achieve costs that are low enough for large scale worldwide adoption in the short term until the wafer supply catches up with demand. However, non-wafer based technologies such as thin-film devices are not as affected by the silicon wafer supply. It is likely that only the best of the thin-film photovoltaic devices will eventually be able to achieve the low costs that are required for wholesale electricity generation and the devices will need to have improved efficiency, with the materials being abundant, non-toxic, and durable.[9]

While the high efficiency and material abundance addresses the issues of high cost, the toxicity and durability are part of the environmental barriers to solar cell growth. Some non-silicon types of photovoltaic devices such as Ga-As have already been well developed and many other semiconductor combinations are in the early to mid level research phases. While high efficiencies can be achieved, many of these devices use

semiconducting elements that are very low in abundance on earth such as Ga, As, In, Cd, Te, Se, etc. This will not be practical for global mass adoption due to the inevitable scarcity of the raw materials, although they will always have their purpose in high efficiency niche application such as in the aerospace industry. Toxicity is also an important environmental barrier and significantly limits the use of harmful materials such as cadmium due to outright bans or regulations that require heavier and more expensive encapsulation.[9]

Other environmental barriers are simply due to the nature of solar cells in that their power output depends on the sun's presence and light intensity. The resulting lack of constant power output sparks discussion about the ability of solar cells to complement the rigid baseline power supply.[10] Despite its inherent variability, one of the strengths of solar power is that its output tends to correlate highly with peak electricity demand in warm seasons.[1112], This is partly due to the world-wide adoption of air conditioning as well as refrigeration, and the fact that power demand spikes when the light from the sun is most intense. [12] In public and commercial buildings the electricity demand during daytime is approximately twice the demand during the night and this is very consistent throughout the year, making localized and building-integrated solar cells a very appropriate power source with the peak power output matching peak demand. [12] In this case the baseline power is complemented by the solar cell power profile and reliance on conventionally generated electricity can be significantly reduced. [11]

The variation in solar power is an issue because of the inflexibility of a typical power grid which is highly centralized and relies on baseline power sources that have a minimum capacity they must maintain during operation.[10] Calculations have shown that 120 GW of the 700 GW of power demand in the USA could be supplied by photovoltaic

systems without a change to the grid or losses due to excess power. [11] It has been predicted that as grid technologies advance, photovoltaic systems could supply up to 50% of the annual US power demand. [11] This would require a very flexible power grid, but by using high density energy storage in conjunction with photovoltaic systems, even baseline power could be supplied by renewable energy and thus replace much of the traditional baseline power sources, resulting in a sustainable system.[13] This is no small task because major improvements in battery technology are likely also needed and that is a field with its own set of challenges.

In addition to all the cost and environmental barriers, there are many social barriers that will need to be addressed through better public communication of science and through progressive policy development that focuses well beyond the short term. Some examples of key social issues are the impact of global warming denialism on public perception, the economic and political strength of the petroleum industry, and the common accounting practice of ignoring the costs of externalities when assessing fossil fuels.

Traditional single crystal silicon wafer p-n junction photovoltaic cells are approaching their maximum efficiency and with wafer prices not likely to decrease significantly, there is little room left for major improvement. The second generation of photovoltaic cells evolved from the need to reduce the material costs by using thin-film technology rather than single crystal silicon wafers. Some of these devices still utilize silicon but it is polycrystalline or amorphous, which essentially trades some efficiency for major cost savings. The GaAs thin film devices slightly outperform Si with a record efficiency of 26.1%, and some other materials are also close to that.[6] However, even if the efficiency was much higher, as is the case for third generation devices that utilize multiple

junction layers to cover a broader solar spectrum, the raw material abundance for non-silicon semiconductor photovoltaic devices is a major limiting factor to rapid growth and widespread adoption. This is where the appeal of organic solar cells emerges because they are carbon-based and thus have the potential for very low material cost in comparison to inorganic devices.

Organic photovoltaic devices use polymer thin-films formed from abundant raw materials which are low cost and usually non-toxic. Polymers have a wide range of chemical flexibility due to chemical synthesis methods compared to inorganic semiconductors which enables the various properties to be adjusted and controlled for optimization. Additionally, the substrates can be made from flexible materials which enable large scale mass production techniques such as roll-to-roll continuous processing, while other processing advantages include the utilization of solution processing and the possibility of printing technologies.[14] Organic devices can also take advantage of mixing or layering to combine materials with different absorption profiles to capture a broader portion of the solar spectrum. The absorption coefficients of organic semiconductors are high relative to that of inorganic materials, but one of the biggest challenges is that the carrier mobility is very low in comparison.[15]

One of the ways to improve the carrier mobility is by introducing higher mobility materials into the polymer thin film that can act as charge carrier highways. Carbon nanotubes are widely known as highly conductive nanoscale molecular fibers with a high aspect ratio and these properties are ideal for improving the mobility in polymer films. They are also electron acceptors and act as a dissociation site for excitons, which are both important elements of bulk heterojunctions type organic photovoltaic devices.[16] One problem is that unmodified carbon nanotubes are insoluble and this makes it difficult to

separate individual nanotubes from their bundles and to evenly disperse them in the polymer film. Due to the small diffusion length of excitons, it is important for nanotubes to be very evenly dispersed, therefore solubility is an asset.

Carbon nanotubes can be made soluble with various functionalization techniques. These typically involve either the covalent attachment of soluble functional groups or polymer chains, or the use of noncovalent bonding methods such as adsorption of functional molecules or π-π wrapping of functional molecules or polymer chains.[17] While the covalently bonded functional groups can alter the electronic structure of the nanotube, the π-π wrapping method tends to preserve the electronic structure.[18] Therefore, in an application where the conductivity is important such as in organic photovoltaic devices, the non-covalent π-π wrapping method is the superior approach for nanotube functionalization.

Conjugated polymer films for the active layer of organic solar cells have been fabricated using an assortment of solution based wet processing techniques such as spin coating, doctor blading, screen printing, ink jet printing, layer-by-layer, spray deposition, or electrophoretic deposition, with spin coating by far being the most common of these techniques.[15] In the case of carbon nanotube films, there is a smaller variety of reported successful fabrication techniques and these are spin coating, layer-by-layer, electrophoretic deposition, and vacuum filtering.[19, 20] As with polymer films, spin coating is also the most common technique for the formation of carbon nanotube films.

While spin coating is a fast and very common technique, it has a very high amount of wasted materials with the majority of the material being ejected off the substrate immediately. The technique is also limited in its scale up potential and in the range of thickness and control.

Electrophoretic deposition (EPD) is a potentially superior technique because there is very little wasted material, there is little restriction to the shape or size of the substrate, the film thickness is controllable over a broad range, and the technique can be expanded to large scale processes.

Despite the potential of this technique, there has been little reported utilization of electrophoretic deposition to deposit films of functionalized carbon nanotubes, especially in photovoltaic applications. There are some studies where EPD was used to deposit films of conjugated polymers but only from a non-solvent colloidal suspension rather than a solution and using toxic solvents such as acetonitrile and toluene. To the best knowledge of the author, soluble conjugated polymers have not been deposited by EPD from a solution. Conjugated polymers have also not been previously deposited by EPD using non-toxic solvents such as water and ethanol. Carbon nanotubes that are functionalized with soluble conjugated polymers have not yet been deposited by EPD. Additionally, EPD has not yet been utilized to deposit the active layer in a solid organic photovoltaic device, with or without carbon nanotubes. These gaps in the fields of electrophoretic deposition and organic solar cells will be addressed through this thesis.

The research efforts on these topics are motivated by concerns for environmental sustainability which create the need for advances in photovoltaic technology that could some day be fulfilled through organic photovoltaic devices. Perhaps this could be accomplished by utilizing the unique properties of carbon nanotubes and by applying the untapped techniques of electrophoretic deposition towards photovoltaic device fabrication.

1.2 Objectives

The following are the primary objectives of the work described in this thesis and are new contributions that have not previously been reported in the literature:

1) Develop electrophoretic deposition techniques to deposit films of a soluble conjugated polymer from non-toxic solvents and extend the technique to deposit films containing carbon nanotubes that have been non-covalently functionalized with the conjugated polymer.

2) Further develop the deposition process in order to achieve appropriate film quality and to demonstrate control over film thickness and morphology.

3) Apply the electrophoretically deposited coatings to the application of the active layer in a solid organic photovoltaic device. Adapt common experimental methods of organic photovoltaic device fabrication to the unique constraints of the specific EPD process and coating material. Adapt laboratory procedure learned from the Xerox Research Center of Canada (XRCC) to enable device fabrication in the available laboratory facilities within McMaster University.

2. Literature Review

2.1 Solar Cell Variables and Working Principles

This section will briefly explain the variables that are important to solar cell characterization and performance evaluation.

The efficiency of a solar cell can be measured in a few ways and each provides a different piece of information. The quantum efficiency can be measured as internal or external and while both measure the amount of charge carriers generated by the known amount of input photons at each wavelength, they both have a unique purpose.

The external quantum efficiency, EQE, also known as the incident photon to current efficiency, IPCE, is the fraction of photons that resulted in collected charge carriers at each wavelength, and is typically plotted as percent of photons converted to charge carriers as a function of wavelength or energy across the whole solar spectrum.[21] These measurements do not filter out the effects of light reflection, photon transmission, or charge carrier recombination, all of which prevent some photons from being converted and collected as charge carriers.

The internal quantum efficiency, IQE, can be thought of as a correction to the EQE in that it only considers photons that were absorbed, and measures the fraction of those photons that are collected as charge carriers. [21] Therefore reflected and transmitted photons are removed from the EQE to calculate the IQE. Both quantum efficiencies can be measured, but the IQE is determined indirectly by measuring the reflected photons and the transmitted photons at each wavelength and removing their consideration from the EQE to give the IQE.

The quantum efficiency is useful to characterize the photon to current performance of the device across the energy of the whole solar spectrum, and it provides useful information about low absorption regions of the spectrum. It is important to note that this is purely a measure of current and does not take into account the voltage, therefore does not provide information about the actual power output of the device. With a low band gap material, more photons across the spectrum will be converted to electrons but because of thermalization, they will not provide a voltage larger than the size of the band gap. A high band gap material results in a larger voltage, but the current is lower because low energy photons can not be absorbed. Because of these competing factors, there exists an optimum band gap where the balance between more current and more energy per charge carrier maximizes the power output of the device, since power is the product of current and voltage.

The most important efficiency measurement which characterizes the overall performance of the cell is the power conversion efficiency. This is simply the fraction of incoming power, P_{in}, from sunlight that is converted to outgoing electrical power, P_{out}, through the photovoltaic process.

$$\eta_{PCE} = \frac{P_{OUT}}{P_{IN}} \qquad \text{(EQ1)}$$

The power conversion efficiency is typically calculated from the values at key points on the current vs. voltage graph, which is likely the most important and most common form of solar cell characterization. A typical current vs. voltage graph is illustrated in Figure 1 showing both the dark and illuminated cases.

In the dark the photovoltaic cell behaves similar to a rectifying diode in that the current is only high in the forward bias direction and there is only current when a bias is

applied to the circuit. Under illumination the photovoltaic cell produces current and the illuminated I-V curve can be approximated as the superposition of the dark current curve and the short circuit current, I_{SC}.[22] The short circuit current is the current through the device under illumination when the applied voltage across the device is zero.

Another important variable is the open circuit voltage, V_{OC}, which is the voltage across the device when the resistance is infinite, measured practically by having the circuit open between the contacts.

The I-V curve of an ideal photovoltaic cell is highly "square" in shape with the curved part approaching to the point (V_{OC}, I_{SC}). The slope at lower voltages should be approaching zero, and the slope at the open circuit voltage should be approaching infinity. Since the power output of the device is the product of the voltage and the current, the most efficient devices approach this ideal square shape, and there is an important measurement of the "squareness" of the I-V curved called the fill factor.

The fill factor, FF, is measured by determining the maximum power point, MPP, which is the point along the I-V curve that maximizes the product of V and I, which visually maximizes the area of the rectangle bound by the origin, and the maximum power point, show in Figure 1 as the shaded rectangle.

$$FF = \frac{\max(VI)}{V_{OC} I_{SC}} = \frac{V_{MPP} I_{MPP}}{V_{OC} I_{SC}} \qquad \text{(EQ2)}$$

The fill factor can also be thought of as the percentage of the area of the outer rectangle defined by V_{OC} and I_{SC} that is covered by the inner rectangle, defined by the MPP.

The power conversion efficiency can be calculated from the I-V curve using the maximum available power from the maximum power point as the power output expressed in terms of the three most important characteristics of the photovoltaic device; V_{OC}, I_{SC}, and FF.

$$\eta_{PCE} = \frac{V_{MPP} I_{MPP}}{P_{IN}} = \frac{FF(V_{OC} I_{SC})}{P_{IN}} \qquad \text{(EQ3)}$$

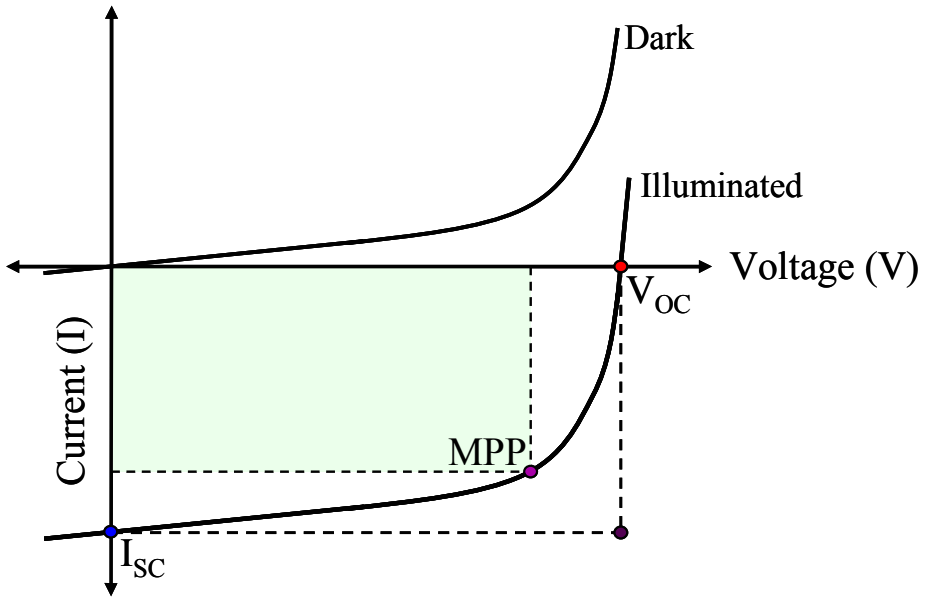

Figure 1 - Illustration of a typical current vs. voltage curve showing the dark and illuminated cases.

Since the current depends on the illumination and therefore the area of the device surface perpendicular to the light source, the current is often expressed as current density, J, and the input power from the light source is expressed as power density. While initially measured as I-V curves, most are typically reported as J-V curves and the short circuit current is reported as short circuit current density, J_{SC}.

The deviation of the I-V curve from ideality is often a result of high series resistance and low shunt resistance which both have the effect of reducing the fill factor as illustrated in Figure 2. Series resistance, R_S is the resistance to current flow through the

layers of the device, the contacts, and the electrodes.[22] High series resistance can become a major problem when the photocurrent is high such as under intense illumination from solar concentration.

Low shunt resistance, R_{Sh}, represents leakage currents such as those around the edges of the device or through small short circuits within the device and it is a problem in devices that exhibit poor rectification properties.[22] High quality photovoltaic devices have a low series resistance and a very high shunt resistance, resulting in a high fill factor.

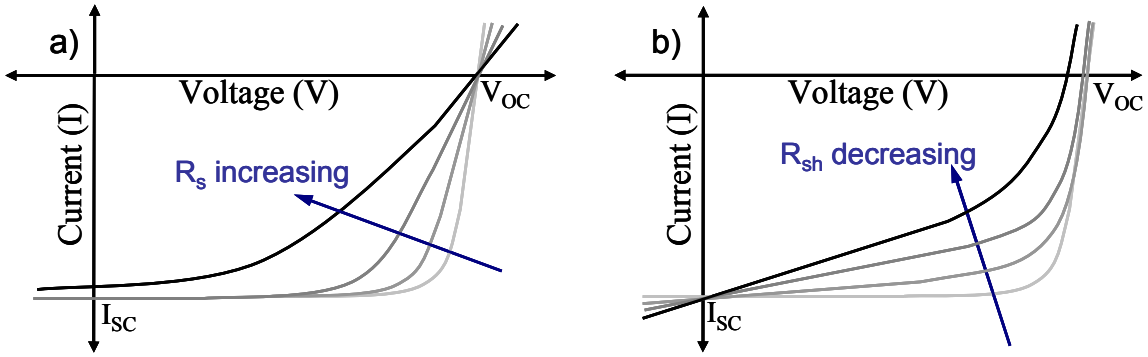

Figure 2 – An illustration of the effects of parasitic resistance on the I-V curve. a) Series resistance. b) Shunt resistance. [Redrawn from J. Nelson 2003[22]]

2.2 Traditional Photovoltaic Cells

In order to understand the mechanisms of organic photovoltaic cells and the purpose for their existence, it is helpful to have a basic understanding of traditional inorganic semiconductor-based photovoltaic cells. The traditional solar cell, depicted schematically in Figure 3, is a single crystal silicon wafer or a polycrystalline silicon substrate. The device is typically fabricated by p-doping the whole substrate and then n-doping the top side by diffusion or ion implantation at a concentration above that of the base p-type dopant to create a p-n junction. A solid metal electrode is formed on the base of the substrate and a fine metal grid electrode is placed on the top side with enough open space to let most of the light pass through. An anti-reflective coating is added to the top surface

to increase efficiency and encapsulation techniques are applied to the solar cell modules to increase durability and lifespan.

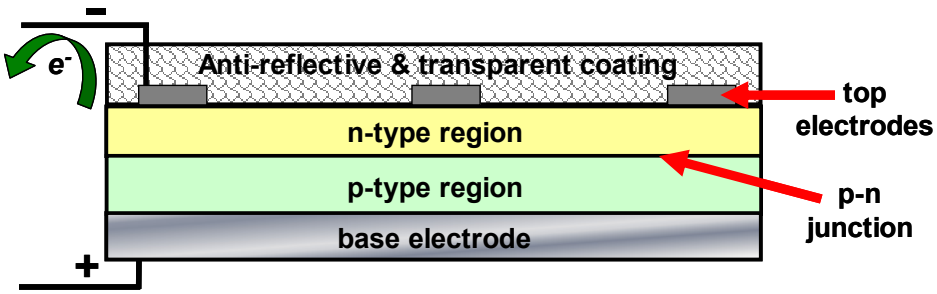

Figure 3 - Schematic of the traditional photovoltaic device structure.

The common photovoltaic cell works by the semiconductor material absorbing light, which causes an electron in a low energy state to be excited into a high energy state, directly producing charge carriers. The charge carriers move in opposite directions through an external circuit thus producing an electric current. Within the p-n junction, there is a built in electric field that assists the flow of holes and electrons to their respective low energy and high energy contacts.[23] However, this directional motion is primarily a result of selective contact, where the n-type region allows the free motion of electrons in the excited states (conduction band) and the p-type region allows the free motion of holes in the ground state (valence band).[23] This phenomenon is depicted generally by Figure 4a and specifically for p-n junction devices in Figure 4b.

This traditional style of solar cell accounts for approximately 85% of the commercial market share as of 2007.[24] The single crystal silicon wafer cell is the most efficient of the traditional style and the recent record laboratory efficiency has reached 25%, with the best commercial modules now exceeding efficiencies of 21%.[6] These numbers approach the 31% theoretical maximum efficiency limit for p-n junction solar cells under one Sun illumination as determined by Shockley and Queisser in 1961, which arises from the assumption that any energy from a photon that is in excess of the band gap will be lost to

thermalization.[7, 25] Since there is little remaining room for improvements in efficiency, performance can only be significantly improved by reducing costs or through a dramatically different device structure that shatters the 31% barrier. The design of such a device can be conceived by considering the most significant efficiency loss mechanisms in the p-n junction solar cell.

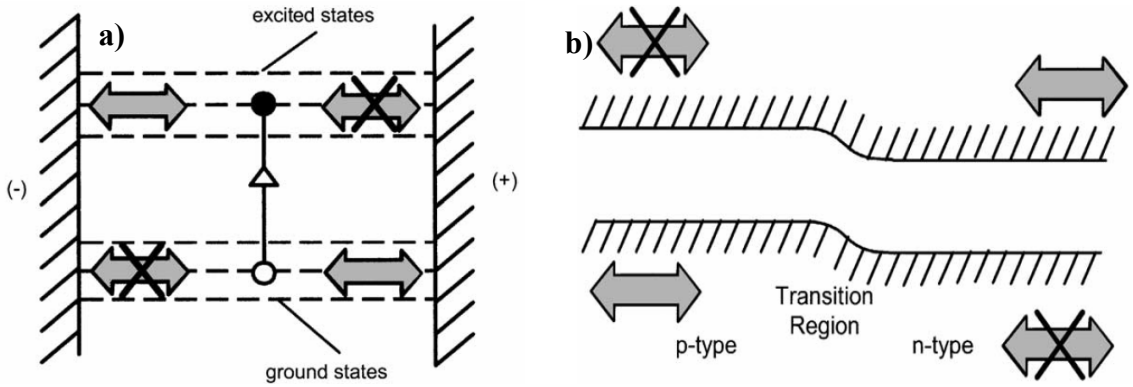

Figure 4 - a)General selective contact to the excited states on one side and ground states on the other. b)Selective contact in a p-n junction showing that electrons travel freely in the n-type region while holes travel freely in the p-type region.[23]

The major efficiency loss mechanisms in a p-n junction solar cell are illustrated in Figure 5. The first energy loss is the transmission of low energy photons that are not energetic enough to excite an electron across the band gap. This is an important issue for a solar cell because the solar spectrum has a significant amount of energy in the infrared spectrum below the band gap of silicon and none of that that energy is harvested. The amount of lost energy can be visualized by Figure 6, a plot of the solar energy spectrum with an overlay of the amount that is absorbed by a silicon solar cell. The second energy loss mechanism is the thermalization of electrons with an energy level above the bottom of the conduction band. Any photon with more energy than the band gap will excite a ground state electron to a point above the bottom of the conduction band and the energy in excess of the band gap will be converted to phonons almost immediately. This is the most significant energy loss mechanism and it alone reduces the maximum possible

conversion efficiency to approximately 44%.[27] The third and fourth losses are the decreases in energy level at the p-n junction and at the contacts. Finally, the fifth efficiency loss mechanism is the occasional recombination of electron-hole pairs.

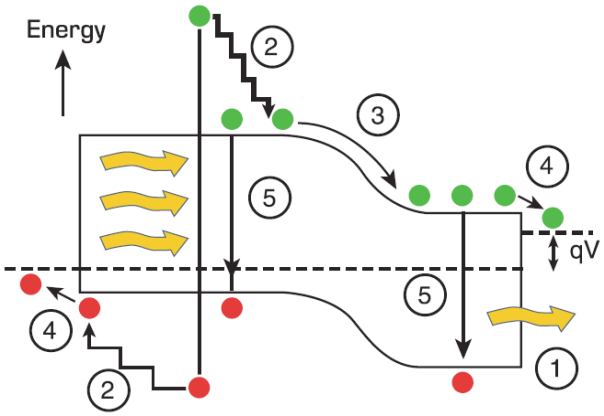

Figure 5 - Efficiency loss mechanisms in a p-n junction solar cell.[26]

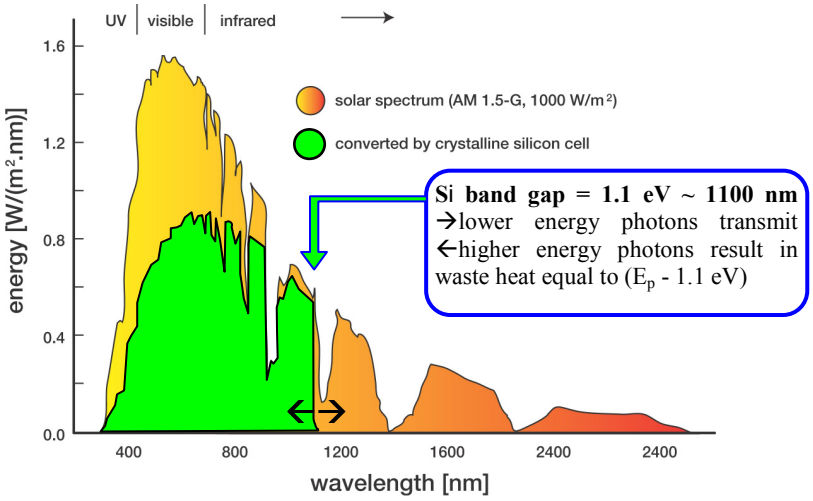

Figure 6 - The solar energy spectrum with the absorption spectrum of silicon showing the amount of sunlight converted by a silicon solar cell.[28]

The most promising approaches to circumvent the traditional efficiency barrier address the photons with either excess energy beyond the band gap or insufficient energy to cause photoexcitation. One of the approaches, commonly referred to as “hot carrier” is

to extract high energy charge carriers before thermalization can occur, which would be possible if the thermalization process can be dramatically slowed.[26]

A different approach seeks to manipulate the yield of electrons from photons of different energies. While photons with an energy just above the band gap would behave normally, two lower energy photons could provide enough energy to excite one ground state electron into the conduction band if for example there was an intermediate band halfway up the band gap, and it has been suggested that quantum dots can be used to form this type of intermediate band solar cell.[29] The electron yield could also be increased if thermalization is slowed enough for impact ionization to occur frequently, which is the process where a high energy "hot" electron in the conduction band imparts some of its energy to knock a bound electron from the ground state into conduction band, resulting in 2 charge carriers from just one high energy photon.[30] This has been proposed for nanostructures where quantization effects occur because quantum confinement changes the relaxation dynamics of "hot" electrons and can result in a slow cooling rate.[30]

The final and seemingly most common approach is to use different semiconductor materials to obtain more than one band gap. This enables the harvesting of photons with different energy levels using band gaps just below the photon energies in a stacked structure called a tandem cell or a multi-junction cell. Using a triple junction cell as a general example, the top layer has the largest band gap and is typically designed to absorb light from the UV spectrum while the rest of the photons transmit through to the middle junction. The visible spectrum photons are absorbed by the middle junction and the remaining infrared portion of the solar spectrum transmits through to be absorbed by the bottom junctions with the smallest band gap. An example of this structure has been fabricated by Spectrolab Inc. with the layered structure depicted schematically in Figure

7a. The band gaps of the materials used in this design are 1.89eV, 1.42eV, and 0.67eV for $GaInP_2$, GaAs, and Ge respectively.[31] The graph in Figure 7b depicts the quantum efficiencies of each layer over the solar light spectrum and it is clear that the choice of materials are well suited to efficiently absorb most of the photons in the solar spectrum. Spectrolab Inc. has the current world record for solar cell efficiency at 41.6% using a triple junction GaInP/GaInAs/Ge configuration at a concentration intensity of 364 suns.[6]

Concentrating direct sunlight onto solar cells usually increases the power conversion efficiency because increasing the current has the effect of increasing the open circuit voltage and the maximum power point shifts resulting in an increased fill factor.[32, 33]

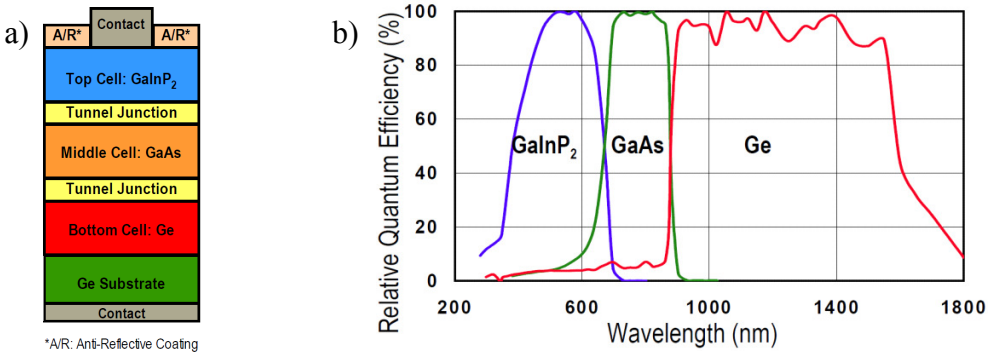

Figure 7 - A triple-junction solar cell fabricated by Spectrolab Inc. a) Schematic cross section. b) Quantum efficiencies of each junction as a function of the wavelength of incoming sunlight.[34]

In addition to achieving higher efficiencies, solar concentration techniques can also dramatically reduce the cost of the power generation because lenses and mirrors are much less expensive than the photovoltaic device. This allows the device itself to be better optimized because the drastically reduced device area justifies the use of the most expensive materials and optimization features. The only major drawback of solar concentrating is the additional costs of increasing the system complexity because it is necessary to have a solar tracking system to ensure direct 90º sunlight at all times, and a cooling system is required to maintain a low device operating temperature under intense

concentrated sunlight.[31] There is a point where efficiency as a function of solar concentration peaks to a maximum, but it is also important to consider the increasing cooling system costs and other structural factors. Therefore there will be a point of maximum practicality for the ideal solar concentration amount which may be at a lower intensity than the point of maximum power conversion efficiency. Solar concentration also increases the maximum possible power conversion efficiency limit. The traditional p-n junction 31% efficiency limit is raised to 41% if solar concentration is considered.[26] When the device is no longer limited to one p-n junction, many of the efficiency loss factors can be mitigated so the traditional efficiency limit can be greatly surpassed and the maximum efficiency rises to 67% under one sun intensity, or as high as 86.8% using solar concentration.[26]

2.3 Conjugated Polymers

One of the biggest drawbacks of semiconductor solar cells is their high upfront cost of manufacturing. Additionally, with the low material abundance of most semiconducting elements, it is important to seek other methods of producing solar cells with more common materials. Carbon-based conjugated polymers are an attractive prospect for both low cost manufacturing and material abundance. These polymers typically have a backbone of alternating single and double covalent bonds in a sp^2 hybridized orbital structure. The sp^2 hybridization structure consists of 3 co-planar σ-bonds which are separated by 120º and a p_z orbital that is orthogonal to the σ-bond plane. Due to energy minimization, this may result in electron delocalization of the π-bonds from the parallel p_z-orbitals of the atoms in the backbone. This path of alternating or delocalized π-bonds is called a conjugated system. While the alternating bond structure is common, the only requirement is that a path along the backbone exists such that each atom in the path has a

p_z-orbital, therefore atoms with lone pairs such as oxygen, nitrogen, and sulfur can also be a part of the conjugated system.

To become highly conductive, conjugated polymers need to be doped, typically through oxidation which gives them p-type hole conducting properties and they function as electron donors.[15] Without doping they are either insulating or semi-conducting. Some polymers can be doped to become n-type electron conductors and will act as an electron acceptor. The dopants in conjugated polymers do not assume substitutional positions as in semiconductor doping but instead they create polymer salts through a redox reaction where the "dopant" accepts or donates an electron to the polymer.[35]

The conduction mechanism of conjugated polymers is complicated by the fact that most conjugated systems are not fully composed of a delocalized pathway. Peierls' Theorem states that a one-dimensional metal is unstable and will result in dimerization, which in this case is alternating single and double bonds with longer and shorter bond lengths respectively, and this distortion causes an energy gap to form.[35] This energy gap is why conjugated polymers are intrinsically insulating or semiconducting rather than acting as a one-dimensional metal utilizing a delocalized conducting pathway.

The key to the conduction mechanism relies around defect sites that occur when different variations of the alternating single and double bonds meet at a point. This is most easily illustrated with Polyacetylene, which was the first polymer that was made to be conducting and likely the most thoroughly studied. The structure is a simple carbon chain with alternating single and double bonds and can take on two orientations which are a mirror image. The two isomers have equal energy and the double bonds can be switched to obtain the other form without a loss of energy, but a defect arises when the two orientations meet as illustrated in Figure 8.[35] This can occur for example when the cis

structure isomerizes to the more stable trans orientation at different locations and an A-type bond sequence can meet a B-type bond sequence to form a relatively stable free radical defect called a soliton, which can travel freely along the chain.[35] This electron exists in a unbound state at an energy level between the two energy bands and is responsible for the intrinsic semiconducting properties of polyacetylene.[35]

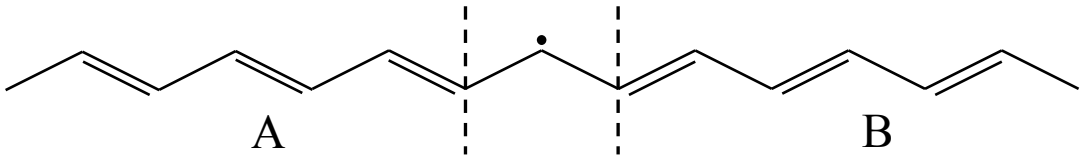

Figure 8 – Polyacetylene structure (trans), showing the soliton free radical defect that occurs when two different alternating single and double bond sequences meet.

Polyacetylene can be doped to become either a p-type or n-type semiconductor, and the redox doping reaction either removes the free radical to create a positive soliton or adds another electron to create a negative soliton, both shown in Figure 9. At high enough doping levels, the soliton regions begin to overlap and broaden the midgap energy band which can eventually overlap with the valence and conduction band, thus turning polyacetylene into a metal-like conductor.[35]

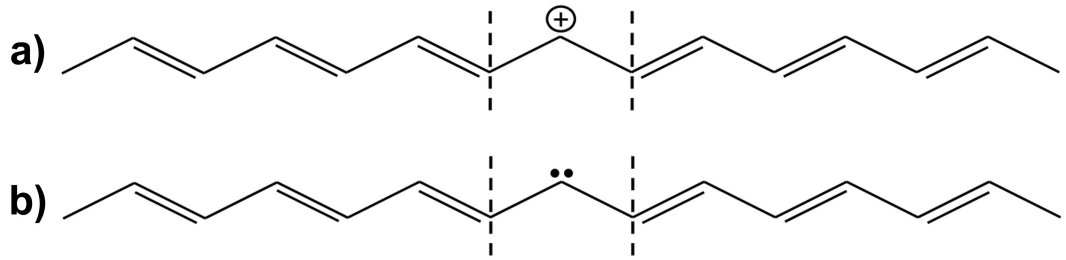

Figure 9 - Doped polyacetylene structure (trans) showing a) p-type and b) n-type doping, resulting in a positive soliton and negative soliton respectively.

A slightly different conduction mechanism exists in many other polymers and this can be explained by describing the case of poly(p-phenylene) where two isomers of the structure (Figure 10) are not equal in energy, with the benzenoid form (a) being lower energy than the quininoid form (b), and there is an energy barrier that must be overcome

to switch between the two.[35] A soliton is formed where the two isomers meet, but due to the energy barrier of switching isomers, the soliton is trapped and falls into a relaxed state of equilibrium by polarizing its environment, forming a defect called a polaron.[35] If two polarons are close they will share the polarization field and it is energetically favorable for them to remain paired, thus forming a bipolaron. Polarons and bipolarons move by a hopping motion because they must overcome an energy barrier rather than being able to travel freely.[35]

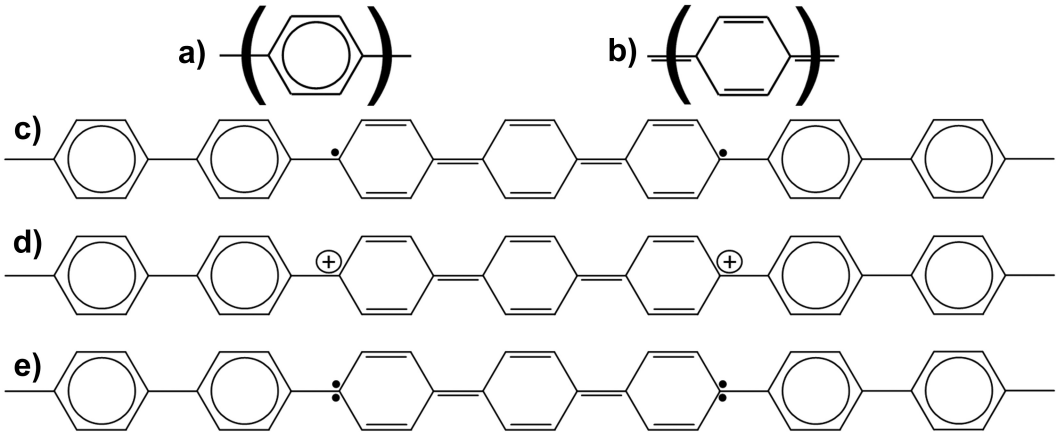

Figure 10 - Poly(p-phenylene) structure and conduction mechanism. a)benzenoid isomer. b)quininoid isomer. Two isomeric structures. c)unstable neutral solitons at the points where the two forms meet. d) stable p-type bipolaron. e) stable n-type bipolaron.

As with solitons, polarons and bipolarons can be doped. Doping in poly(p-phenylene) increases the occurrence of the quininoid structure because it has a lower ionization potential and a larger electron affinity than the aromatic form.[36] This has the result of significantly increasing the density of bipolarons. If the density of bipolarons is high enough, the overlap of midband bipolaron energy states creates a wide energy band that can eventually overlap with the valence and conduction bands, providing the mechanism for metallic intrachain conduction.[36]

Intrachain conduction is only part of the conducting mechanism, with the other being interchain conduction which describes how charge carriers move to other chains, and is

likely the rate limiting step in polymer conductivity.[36] There are several mechanisms of interchain conduction and they depend on factors such as the crystallinity of the polymer, the amount of π-π interactions between chains, the distance between metallic states, the presence of doping ions between the chains, and the amount of doping.

Defects in the polymer chain structure such as kinks or high angle rotations can cause breaks in the π-conjugation network, creating distinct separated blocks known as conformational subunits.[37] In the crystalline regions of the polymer or anywhere there are cofacial conformational subunits, the chains can be oriented such that there are strong π-π interactions that effectively enable conduction along the two-dimensional conjugated sheet.[38] This occurs by an electronic coupling mechanism that is similar to Förster resonant energy transfer (FRET) and it is a very efficient energy transfer process.[37]

The effect of doping on interchain conduction is that at light or moderate doping, conduction often occurs through a hopping mechanism, while at a high doping amount the conducting mechanism behaves more metallically.[39] Hopping is a phonon-assisted tunneling phenomenon between localized electronic states (polarons and bipolarons), and it occurs much more readily in crystalline regions compared to disordered regions.[39] The degree of doping determines the density of regions that act in a metallic state, and tunneling can occur between these metallic islands if the distance between them is appropriately close.[39] Doping can also introduce dopant ions between polymer chains which can act as a bridge that transfers carriers.[40]

In addition to their interesting electronic properties, conjugated polymers are typically capable of absorbing light. The part of the structure that is responsible for light absorption is called a chromophore, and in the case of conjugated polymers it is the same π-conjugated region of alternating single and double bonds that is responsible for the

conduction mechanism. The light absorption properties can be locally modified by the morphology of the polymer chain conformation which can result in a broadening or shifting of the absorption spectrum.[37]

Photon absorption in a conjugated polymer requires that the energy of the photon is large enough to cause the excitation of an electron above the energy gap in the chromophore. This excited electron is bound to its corresponding ground state hole, creating a quasi-particle called an exciton. The excited electron-hole pair has a large binding energy E_B, that must be overcome in order to separate the two bound charges. The exciton binding energy in conjugated polymer systems has been reported to span the range of 0.05 eV to 1.1 eV.[41] The energy gap for photon absorption is the optical gap E_{go}, which is the difference between the highest occupied molecular orbital (HOMO), a π bonding orbital, and the lowest unoccupied molecular orbital (LUMO), a π^* anti-bonding orbital.[41] This usually differs from the conventional semiconductor electronic energy gap E_{ge}, by the following relation[41]:

$$E_{ge} = E_{go} + E_B \qquad \text{(EQ4)}$$

The exciton binding energy can also be influenced by exciton trapping, phonon coupling, and interchain interaction, and the exact nature of the exciton state is still under debate.[14, 42] In some cases excitons appear to diffuse relatively freely through the polymer chains in the π-conjugated system, while in other cases they may be localized in a neutral bipolaron with one positive and one negative charge, called a polaron-exciton, as illustrated in Figure 11.[40] In this case the exciton adopts the hopping type movement restriction of bipolarons. The actual excited state dynamics are controlled by the influence of electron-phonon coupling which causes localization (polaronic behaviour), versus the

competing effect of electronic coupling from interchain π-π interactions which causes delocalization (FRET behaviour).[42]

Figure 11 - Polaron-exciton in poly(p-phenylene).

Excitons in the excited state can recombine to the ground state radiatively to generate photons (fluorescence), can decay non-radiatively to create phonons, or they can become trapped in defect sites.[41] The lifetime of excitons before they recombine is typically in the range of picoseconds to nanoseconds, thus they have a limited distance in which they can travel before recombination occurs.[41] Exciton motion is usually described and successfully modeled to a first approximation as a Brownian random walk,[14, 43] therefore the average distance before recombination is referred to as the average exciton diffusion length and it ultimately depends on the morphology of the materials as well as the electronic structure.[41] For conjugated polymers this length is in the range of 5-70 nm, but for most practical purposes the average exciton diffusion length is usually below 20 nm and 10 nm is typical.[1541] In applications that utilize excitons such as in a photovoltaic cell, the electron and hole charges must be separated and collected before recombination can occur. This imposes a morphological constraint such that the nanostructure should be designed so most excitons are able to be separated before they have traveled the full exciton diffusion length.

Charge separation can occur at trap sites in the bulk material, under the influence of an external electric field, and most commonly at an interface between two materials of different potentials where one acts as an electron donor and the other acts as an electron acceptor.[14] In the donor/acceptor interface, the electron moves into the LUMO of the acceptor materials, while the hole remains in the HOMO of the donor material.[41] Ideally

there should be a donor/acceptor interface every 10 nm in order to efficiently separate most of the exciton charges so that they can be collected in a circuit to do electrical work.

2.4 Organic Solar Cells

2.4.1 History and device structure

The key features that motivate organic solar research are the use of non-toxic and abundant carbon-based material, the low production cost potential through the utilization of solution processing, and the potential application of large scale film production techniques. Additionally, the high chemical flexibility of polymers due to chemical synthesis methods enables the control and optimization of the material properties.

The first generation of organic solar cells were a single layer device prepared by thermal evaporation using organic dye molecules such as cyanines or porphyrins.[44] This organic material was sandwiched between two metal layers which were thin enough to allow some optical transparency and possessed different work functions, often aluminum or indium for the low work function cathode while gold, silver, or ITO glass was used for the high work function anode.[44] The rectifying behaviour in the device came from the voltage difference between the work functions of the two electrodes resulting in asymmetry in the electron and hole contacts to the π and π^* molecular orbitals respectively.[15] Using an aluminum/merocyanine/silver device structure, an external power conversion efficiency of approximately 0.7% was achieved in 1978.[44]

In the single layer device, the organic layer was typically a p-type semiconductor and a Schottky barrier formed between the organic layer and the low work function aluminum cathode.[15] The depletion region in the organic layer at the aluminum contact provides an electric field to facilitate the charge separation of the photogenerated excitons, so that the

electrons can travel to the aluminum contact and the holes can travel through the p-type organic material to the high work function metal contact on the other side.[15] Due to the restrictions of the exciton diffusion length in organic material being typically below 20 nm, only excitons generated within 20 nm of the aluminum contact have a chance at the charge being collected. A schematic diagram of this single layer device structure is illustrated in Figure 12.

The next major advance in organic photovoltaic devices was the implementation of a structure that physically resembles the p-n junction from inorganic semiconductor solar cells, called a bilayer heterojunction. In a device reported in 1986 that achieved 1% efficiency, the photoactive layer was a bilayer of p-type copper phthalocyanine with a n-type perylene tetracarboxylic derivative on top, and this was sandwiched between a silver thin film as the top low work function cathode and with ITO glass as the bottom high work function anode.[45] This result held the top performing spot for organic solar cells for the next 14 years while the field of conjugated polymers was developing.[15]

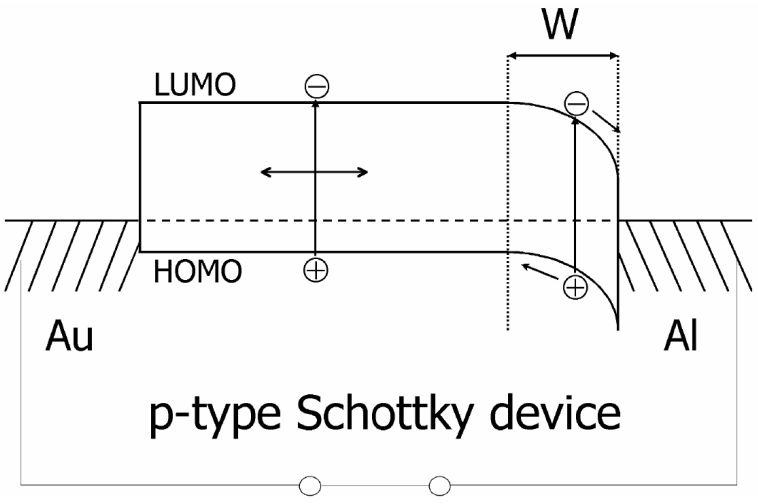

Figure 12 - Energy band diagram for a single layer organic solar cell, showing the depletion layer, W, at the edge of the cathode where exciton dissociation can take place.[15]

In the bilayer heterojunction device, photons enter through the ITO side since it is a transparent conducting electrode, and excitons that are created by photoexcitation within the 10-20 nm exciton diffusion distance from the donor/acceptor interface can be dissociated into a free electron and hole.[21, 46] Charge transfer, illustrated in Figure 13, occurs at the donor-acceptor interface because the acceptor has a higher electron affinity while the donor has a lower ionization potential.[15] If the exciton is generated in the donor material near the interface an electron will be transferred to the LUMO of the acceptor, while in the other case if an exciton is generated in the acceptor material a hole will be transferred to the HOMO of the donor.

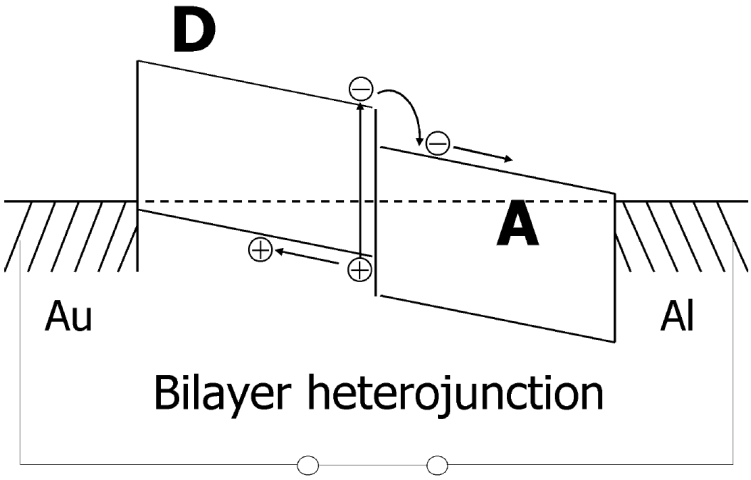

Figure 13 Energy band diagram for a bilayer heterojunction organic solar cell, showing photoinduced charge transfer at the donor/acceptor interface.[15]

The major advantage of the bilayer heterojunction structure is that separated electrons travel freely within the n-type acceptor and the holes travel freely in the p-type donor material, which significantly reduces charge recombination.[15] As with the single layer device, the efficiency of the bilayer heterojunction is limited by the size of the exciton diffusion length on each side of the donor-acceptor interface. Therefore the film needs to be thin enough that a large number of photons are absorbed within the region of the

donor/acceptor interface because all other photon absorption will be lost to recombination, and this lowers the quantum efficiency.[46]

The device structure that is most commonly utilized today originated from the observation of photoinduced charge transfer from illuminated conjugated polymers to C_{60} molecules when C_{60} was blended with a conjugated polymer.[15] If a polymer is blended with enough C_{60} molecules to create a bicontinuous network, the polymer/C_{60} interface acts as a reliable exciton dissociation site due to the local differences in potential. The dissociated charges are transported separately with the electron traveling through the electron conducting C_{60} network and the hole travels through the p-type polymer network. This type of device structure is called a bulk heterojunction and can be described as taking the donor/acceptor concept of the bilayer heterojunction and finely mixing the two layers to create a very large donor/acceptor interfacial area spread throughout the volume of the photoactive layer blend.

The bulk heterojunction concept is not limited to C_{60}, but any mixture of a donor material and an acceptor material that are good conductors of holes and electrons respectively, where the blend forms a bicontinuous network and exciton charge separation spontaneously occurs at the donor/acceptor interface. This device structure is illustrated schematically in Figure 14, showing a continuous donor/acceptor interface for exciton dissociation throughout the thickness of the organic layer.

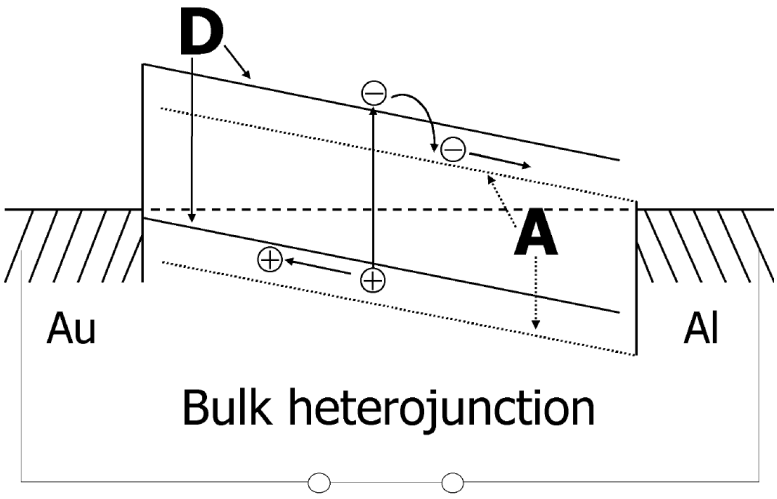

Figure 14 - Schematic of a bull heterojunction device, showing the continuous donor/acceptor interface and conduction paths through throughout the photoactive layer.[15]

The bulk heterojunction is typically considered the superior design because absorption can take place anywhere in the thickness of the photoactive layer as long as there is a nearby donor/acceptor interface within the exciton diffusion length. If the materials form a well networked structure then conduction of the dissociated charges to their respective electrodes can occur efficiently through separate paths, but the biggest advantage of the bulk structure is in the high exciton diffusion and dissociation efficiencies.

2.4.2 The origin of the quantum efficiency

The power conversion efficiency of organic photovoltaic devices is experimentally determined in a similar way to traditional solar cells but the differences in the photovoltaic mechanism are evident when the quantum efficiency is broken down into parts. The external quantum efficiency is the product of the efficiencies of the serial steps in the organic photovoltaic mechanism from an incoming photon to a successfully collected electron. These steps are photon absorption, exciton diffusion, charge separation, and charge collection.

The probability that an incoming photon gets absorbed is called the absorption efficiency, η_{abs}, and it depends on many factors. The reflective properties of the surface, the material's absorption spectrum and absorption coefficient, the thickness of the photoactive layer, and the amount of non-absorbing material in the in the photoactive layer all contribute to the absorption efficiency.[15]

After absorption, the exciton needs to diffuse to a surface where dissociation can take place and this is typically at a donor/acceptor interface. The exciton diffusion efficiency, η_{ED}, is a measure of the probability that a photogenerated exciton successfully reaches a donor/acceptor interface before recombination occurs.[47] This probability depends on the exciton conducting properties of the absorbing material as described earlier in the conjugated polymers section. The phenomena that affect the movement of excitons can be folded into the average exciton diffusion length. Other important factors include the trap density because traps can induce recombination, and the nanoscale morphology of the donor and acceptor materials because if the exciton travels along a pathway that spans a distance larger than the exciton diffusion length then it is not very likely to reach a donor/acceptor interface before recombination occurs.

Once diffused to a donor/acceptor interface, a photogenerated exciton can dissociate according to the probability of charge separation and transfer to the acceptor. This probability can be described as the charge transfer efficiency, η_{CT}.[47] At the donor/acceptor interface the exciton can dissociate because there is a driving force from the difference in potential between the two materials. The electron is transferred to the LUMO of the acceptor while the hole remains in the HOMO of the p-type donor material. The charge transfer efficiency typically approaches 100% if the energy offset between the HOMO of the donor and the LUMO of the acceptor material exceeds the exciton binding energy.[47]

After exciton dissociation, the electron travels through the acceptor material to the cathode while the hole travels through the donor material to the anode. These charge carriers are driven by the difference in the work functions of the electrodes which creates an internal electric field, as well as a diffusion current caused by a charge carrier concentration gradient.[15] Thin devices in the range below 100nm tend to be mostly driven by the field drift while thick devices are more dominated by the diffusion current due to screening of the electric field.[15] The efficiency of this process is called the charge collection efficiency, $\eta_{CC,}$ which is the fraction of photogenerated and dissociated charge carriers that are collected at the electrodes.[47] This efficiency tends to be very high and can approach 100% in the bilayer heterojunction structures because the photogenerated electrons and holes are spatially separated in the acceptor and donor material respectively, and if the mobilities are sufficiently high then recombination is not likely.[47] However, in the bulk heterojunction the charge collection efficiency is typically much lower than 100% because spatial overlap can occur between photogenerated electrons and holes leading to recombination, and dead end pathways can lead to trapping.[47] The presence of percolating donor and acceptor pathways is important for efficient charge collection in the bulk heterojunction structure.

The product of the efficiencies of the 4 steps from input photons to collected charges gives the external quantum efficiency. As discussed previously, the external quantum efficiency is the internal quantum efficiency plus the effects that reduce absorption such as reflections and transmissions. The following equation shows the quantum efficiencies in terms of the described serial steps:

$$\eta_{ext} = \eta_{abs} \times \eta_{\text{int}} = \eta_{abs} \times \eta_{ED} \times \eta_{CT} \times \eta_{CC} \qquad \text{(EQ5)}$$

2.4.3 Materials

As the field of organic electronics grew from its infancy, some of the materials and methods became common enough to be considered as standard. While most inorganic solar cells use a metal grid cathode as the side of the device to receive the incoming light, it became common to utilize the opposite side for this purpose in organic devices, and a transparent film is used instead of a grid. A grid electrode is not very practical in organic solar cells because of the low conductivity of organic material and the large lateral distances that charges would have to travel to reach the electrode compared to the film thickness. Indium oxide doped with tin oxide, typically referred to as indium tin oxide (ITO), is regularly used as the transparent anode film in organic devices. ITO is commercially available and usually coated onto a glass substrate, although it is possible to use other transparent substrates such as a Polyethylene terephthalate (PET) film, which enables the device to be highly flexible.[14]

The work function of commercial ITO varies but it is usually reported at approximately 4.7 eV, and it can be increased by surface treatment.[48] Oxygen plasma cleaning, UV ozone treatment, and a few other less common surface treatment methods have been used to increase the work function of ITO up to 5.0 eV, and this improvement is loosely attributed to the removal of carbon contamination, the change of surface chemical composition, or the possible formation of a surface dipole layer.[41, 48, 49] The removal of carbon contamination by UV ozone treatment is beneficial in all cases but the optimal treatment of the ITO surface depends on the other materials used in the device so there is no clear best approach.[41]

Before the photoactive layer is formed, a buffer layer is often deposited on the ITO surface to improve the power conversion efficiency. The most common buffer layer is a

polyelectrolyte complex called poly(3,4-ethylenedioxythiophene):poly(styrenesulfonate) or PEDOT:PSS, shown in Figure 15. PEDOT is a positively charged conjugated polymer resembling a modified polythiophene structure whereas PSS is a negatively charged polymer that is used to stabilize PEDOT in aqueous solution. PEDOT:PSS has a high work function around 5.2 eV, acceptable transparency and conductivity, and can be spin coated to form a thin film with a smooth surface.[50]

A layer of PEDOT:PSS between the ITO and the active material improves the diode quality of the device, which contributes to a higher fill factor.[14] The buffer layer also acts a hole transport layer, an exciton blocker, protects the photoactive layer from oxygen, and smoothes the known defects of the ITO surface that would normally become traps.[21] It is important to optimize the thickness of the PEDOT:PSS layer because thick layers have lower transparency and increase the series resistance of the device, but if the layer is too thin it will contain more pin holes.[41] PEDOT:PSS films should be annealed to drive off water and improve the conductivity, but the thermal treatment also needs to be optimized since the annealing schedule and atmosphere affect the surface properties such as roughness.[50]

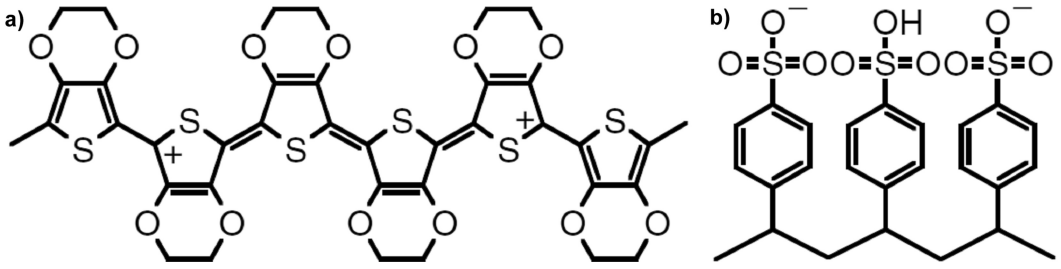

Figure 15 - Chemical structure of a)PEDOT and b)PSS.[50]

On the other side of the organic photovoltaic device, the low work function electrode is commonly an aluminum thin film formed by thermal vacuum evaporation deposition, with a work function of 4.28 eV.[41] Other low work function metals such as silver, indium,

magnesium and calcium are occasionally used, but the more reactive metals are usually followed by a protective layer of a relatively stable metal such as silver.[41]

Similar to the anode side, a buffer layer is often deposited between the photoactive layer and the low work function electrode. One of the most common is a very thin (~0.6 nm) layer of lithium fluoride (LiF), deposited by thermal vacuum evaporation. The precise role of LiF is unclear because the deposit is not thick enough to form a closed layer over the organic active layer, but it has been shown that the cathode metal work function can be reduced as a result of the thin LiF layer and it also increases the contact efficiency between the two layers.[15, 46] The LiF layer commonly results in an improved fill factor and open circuit voltage and thus a slightly higher power conversion efficiency.[14, 51] It has been suggested that the charge transfer across the interface is due to the formation of a dipole moment across the organic/metal junction from either orientation with Li^+ adhering to the organic side and F^- to the metal electrode, or chemical reactions.[41 51] It is important to control the thickness of the LiF layer because it is an electrical insulator and when it is beyond 1 or 2 nm the layer begins to have negative effects on the device performance. [41 51]

Bathocuproine (BCP) is another documented option for the buffer layer under the low work function electrode. BCP films are deposited by thermal evaporation to a typical thickness of 10 nm, and similar to LiF, optimization is important because there exists a thickness where the film begins to have harmful effects on the device properties.[47, 52] BCP is an exciton blocking layer and also forms a passivating layer that is suspected of preventing the diffusion of aluminum into the organic material, eliminating unfavorable reactions with C_{60}.[47, 52] Some studies have shown that BCP can improve the device rectification, increase the short circuit current, and increase the open circuit voltage,

which results in the increase of power conversion efficiency.[52] [41] It was demonstrated with an ITO/subphthalocyanine/C_{60}/BCP/Al device that the 10 nm BCP layer increased the power conversion efficiency from 0.05% to 3.0%, and the improvement was suggested to be mostly a result of the increase in V_{OC}.[52]

The most important layer of the organic photovoltaic device is the photoactive layer where the photon absorption, exciton diffusion, exciton dissociation, and charge transport all take place before the charges move into the electrodes. Most modern organic devices use a bulk heterojunction structure with the donor and acceptor materials blended together. While there is wide assortment of organic materials that have been utilized for this purpose and reported in the literature, only a few of these materials are regularly used as part of the standard toolkit for organic solar cells.

The most widely used donor materials are derivatives of poly(p-phenylene vinylene) (PPV) such as MDMO-PPV[A] and MEH-PPV[B], derivatives of thiophene chains such as P3HT[C] and P3OT[D], the dye molecule zinc or copper phthalocyanine (ZnPc or CuPc), and the occasional derivatives of fluorine backbones such as PFB[E].[15, 21, 46, 53]

The standard acceptor material used in almost every bulk heterojunction device is PCBM[F] which is a derivative of the buckminsterfullerene C_{60}, with the functionalization primarily to increase solubility so that it can be mixed and deposited using solution processing. Underivatized C_{60} can also be used in small molecule bulk heterojunction

---

[A] MDMO-PPV is poly[2-methoxy-5-(3',7'-dimethyloctyloxy)-1,4-phenylene vinylene]
[B] MEH-PPV is poly[(2-methoxy-5-(2'-ethylhexyloxy)-p-phenylene) vinylene]
[C] P3HT is poly(3-hexylthiophene)
[D] P3OT is poly(3-octylthiophene)
[E] PFB is poly(9,9'-dioctylfluorene-co-bis-N,N'-(4-butylphenyl)-bis-N,N'-phenyl-1,4-phenylenediamine)
[F] PCBM is 1-(3-methoxycarbonyl) propyl-1-phenyl[6,6]C_{61}

devices fabricated using thermal evaporation such as in CuPc:C_{60} devices. C_{60} can be electrochemically reduced by up to 6 electrons and thus is a high affinity electron acceptor.[46] Fullerene acceptor devices require a bicontinuous network of both the donor and acceptor material, and the onset of photocurrent has been shown to appear at approximately 17 wt% PCBM, which corresponds closely to the percolation threshold for spherical metal particles in a continuous matrix.[14]

Beyond fullerenes, some n-type conjugated polymers or other small molecules have been utilized for the acceptor material in bulk heterojunction devices, although they do not typically perform as well as fullerene acceptor devices. The most common are perylene and its derivatives, CN-MEH-PPV[G], and F8BT[H].[14, 15, 53-55]

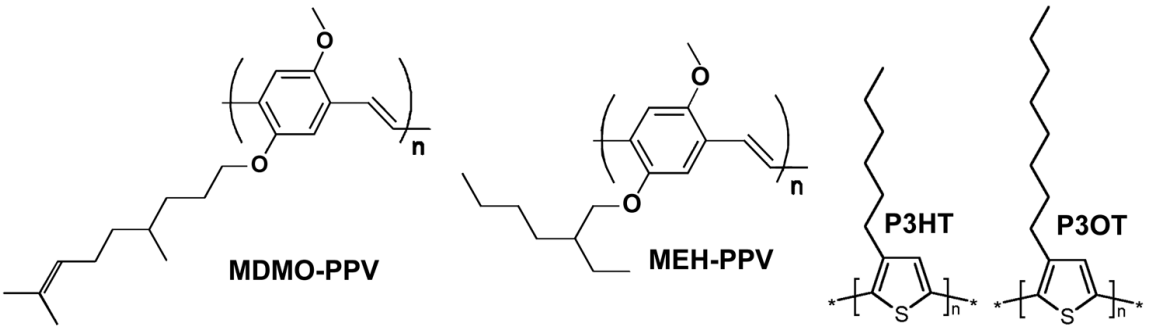

Figure 16 - Chemical structure of MDMO-PPV, MEH-PPV, P3HT, and P3OT. [images adapted[15, 21]]

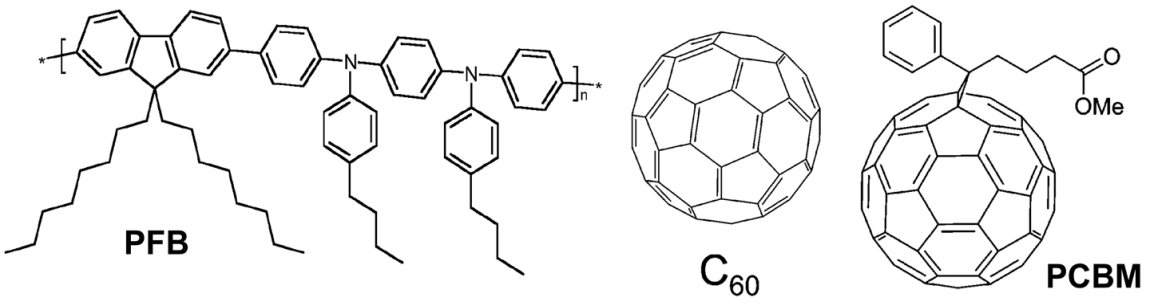

Figure 17 - Chemical structure of PFB, C_{60} and PCBM. [images adapted[15, 46]]

[G] CN-MEH-PPV is poly-[2-methoxy-5-(2'-ethylhexyloxy)-1,4-(1-cyanovinylene)-phenylene]
[H] F8BT is poly(9,9'-dioctylfluoreneco-benzothiadiazole)

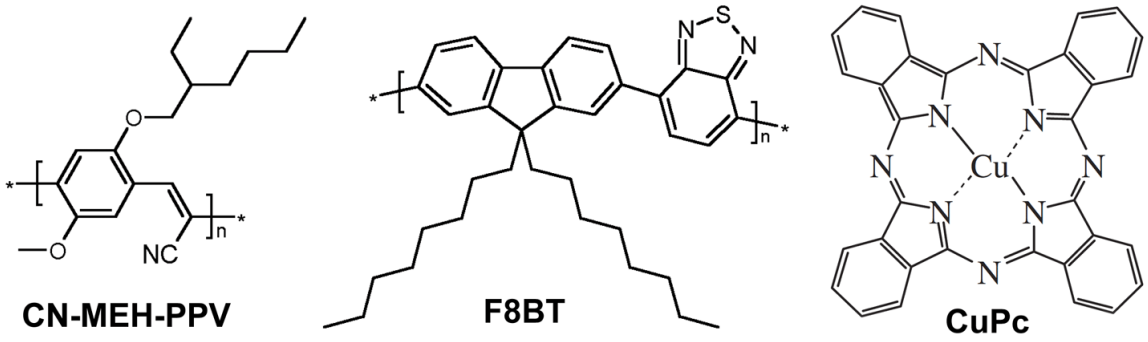

Figure 18 - Chemical structure of CN-MEH-PPV, F8BT, and CuPc. [images adapted[15, 54]]

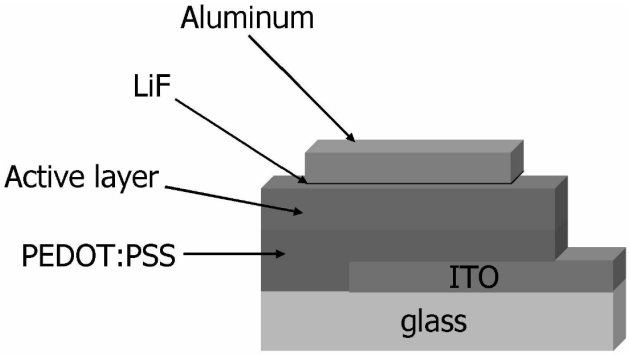

Figure 19 - The physical structure of a typical laboratory quality organic solar cell.[15]

A typical organic solar cell structure appears as depicted in Figure 19, and this device is fabricated in the following manner:

- Commercially produced ITO-coated glass is cleaned with a rigorous cleaning process and the surface is often modified by techniques such as UV-ozone exposure, plasma cleaning, or chemical treatments. Photolithography is often used to partially etch the ITO surface.
- A buffer layer may be deposited on the ITO surface. Soluble polymer materials such as PEDOT:PSS are usually spin cast, while insoluble small molecule materials may be thermally evaporated in a vacuum.
- The active layer is deposited as a thin film similarly to the buffer layer before it. Soluble polymer films are formed by wet processing techniques with spin coating being the standard method, while small molecules are most often thermally evaporated. A bilayer heterojunction will have two separate film formation steps,

most often with the donor material first and followed by the acceptor material. Some devices are designed with an inverted structure, depending on the work function of the materials and the electrodes. A bulk heterojunction film will be fabricated in a single step using either a solution processed mixture of the donor and acceptor materials, or the co-thermal evaporation of the two materials from their pure states.

- The top electrode is most commonly formed by thermal evaporation from the pure metal state. If a buffer layer such as LiF or BCP is desired, it will be deposited prior to the top electrode and usually using the same deposition technique without breaking vacuum between the two steps.

2.5 Carbon Nanotubes in Organic Solar Cells

Since C_{60} fullerenes became the standard acceptor material in bulk heterojunction organic solar cells, it is a logical step to extend the application to carbon nanotubes, another nanoscale carbon allotrope. The conductivity properties of carbon nanotubes are vastly superior to those of fullerenes, and due to their extremely high aspect ratio and nanoscale width, they behave as one-dimensional quantum wires with conduction occurring in well separated and discrete electron states.[56, 57] Single walled carbon nanotubes (SWNTs) should be an ideal material for bulk heterojunctions because they act as electron acceptors with a very high surface area, they provide a driving force for exciton dissociation at a polymer/nanotube interface, and they can form a percolating network at low concentration for efficient charge collection.[16, 58]

Pure carbon nanotubes are limited in their application because of their inherent insolubility in all solvents and because they spontaneously form bundles due to π-π stacking, both of which affect their ability to be finely dispersed in a matrix material. Fortunately some of the functionalization chemistry that was originally developed for fullerenes can also be applied to the nanotube geometry. Two major approaches to SWNT

functionalization are the covalent attachment of chemicals through reactions onto the nanotube surface, and the noncovalent adsorption or wrapping of functional molecules or polymers.[17]

SWNTs that are subjected to an acid purification process end up with defects being introduced at the ends and some defects created on the side walls, with carboxyl group typically forming at these defect sites.[17, 59] These carboxyl sites can be utilized for chemical reactions to attach further functional groups to impart some solubility.[59] Direct covalent sidewall functionalization is not as easy as with fullerenes due to nanotubes having less curvature, but it is possible with highly reactive species.[59] While there is evidence that nanotubes can tolerate a limited amount of defects before losing their electronic properties, much of the covalent functionalization that provides solubility has a negative effect on the conductivity properties.[17, 59]

Perhaps the most promising functionalization techniques are those of noncovalent interactions from species such as surfactants, polymers, polycyclic aromatic hydrocarbons, and biomolecules.[17] The noncovalent method is based on van der Waals forces or π-π stacking and it is an attractive technique because no defects are introduced and the electronic structure of the extended sp^2 hybridized π network is not disrupted.[59, 60] Supramolecular functionalization offers large surface coverage which can be utilized to impart high solubility and various other properties to the nanotube.[60] Species with aromatic groups such as conjugated polymers are especially effective because of extensive π-π stacking interactions with the SWNT surface and due to their coplanar geometry they adopt either a helical wrapping or a straight chain bonding interface.[17, 61, 62]

The conjugated polymer functionalization of SWNTs is of great interest to organic photovoltaic research because if the electron accepting nanotubes are intimately attached

to polymer donor materials then the donor/acceptor interfacial area is very high. This large interface should result in a device with high charge transfer efficiency. Despite the high expectations, there is relatively little research about organic photovoltaic devices with an active layer composed of conjugated polymer functionalized SWNTs in comparison to the standard polymer/C_{60} blends, and the performance thus far is vastly inferior.

2.6 Progress in SWNTs Used in Organic Solar Cells

The most widely published and cited research group studying the use of carbon nanotubes/conjugated polymer composite films in photovoltaic devices appears to be that of Dr. Emmanuel Kymakis and his supervisor Prof. Gehan Amaratunga. Their first study on the topic[63] was a blend of P3OT with <1% SWNT deposited by spin coating onto ITO and covered with a thermally evaporated aluminum top electrode. An ultrathin layer of P3OT was deposited between the ITO and the photoactive layer to prevent the ohmic contact of the nanotubes with the ITO.

In a typical metal-insulator-metal diode model (MIM), the open circuit voltage V_{OC}, of the device is the difference between the work functions of the two metal electrodes. The expected V_{OC} for their device based on the aluminum work function at 4.3 eV and ITO at 4.7 eV was no higher than 0.4 V, but the experimental result was 0.75 V. They proposed that the nanotube percolation network formed ohmic contact with the aluminum electrode, so the metal-insulator-metal setup was actually ITO-P3OT-SWNT and the V_{OC} would then be the difference between the work function of ITO and SWNT. In this case the maximum possible SWNT work function is 3.95 eV under the MIM model, which is within the 3.4 to 4.0 eV stated range for the work function of SWNTs that are assumed to be metallic.

The V_{OC}, I_{SC}, and FF were all considerably increased compared to the pure polymer device and while the resulting power conversion efficiency was only 0.04%, it was over 1000 times larger than that of the same device without SWNTs. They attribute the improvement to the introduction of internal polymer/nanotube junctions which act as dissociation centers and to the continuous pathway for the electrons to travel through the nanotube network to the top electrode.

In a follow-up study[64], Kymakis tested the effect of varying the metal of the top electrode with work functions from 4.3 to 5.1 eV to confirm that it does not have a strong effect on the V_{OC}. In all cases the resulting V_{OC} was much larger than the difference between the work functions of the two electrodes and there was no change in polarity when gold was used, which has a work function on the opposite side of that of ITO, 0.4 eV above. The V_{OC} was only weakly dependent on the metal electrode and there is a slight trend of increasing V_{OC} with increasing top metal work function. The work function difference between the electrodes varied from -0.4 to +0.4 eV using the different metals, while the resulting V_{OC} range spanned only a 0.1 V margin from 0.65 to 0.75 V.

In this study they also revised their theory of the V_{OC} origins, citing an investigation of polymer-fullerene devices where the V_{OC} was highly dependent on the LUMO of the fullerene which suggested that there was Fermi level pinning between the top electrode and the fullerene. They inferred that the upper limit for the V_{OC} can be determined by the difference between the HOMO of the polymer and the LUMO of the fullerene. Extending this theory to the P3OT/SWNT device they state that the HOMO of P3OT is 5.25eV and the work function of SWNTs is 4.5 eV, which is within the possible range they provided in the previous study. The 0.75 V difference between the P3OT HOMO and the work function of the SWNTs matches the maximum V_{OC} they obtained with an aluminum

electrode and is only a few electron volts larger than the V_{OC} obtained with the other lower work function metal electrodes they tested. They conclude that the V_{OC} can be estimated from the energy difference between the HOMO of the polymer and the work function of SWNTs, that the pinning mechanism between SWNTs and the negative electrode is plausible, and that the V_{OC} is only weakly dependent on the work function of the negative electrode.

A few years later Kymakis and Amaratunga published another study[65] where they used a 40 nm layer of PEDOT:PSS between the ITO and the active layer instead of the ultrathin P3OT layer. In this work they experimented with varying the SWNT concentration from 0.25 to 5.0 wt% and found that a maximum efficiency occurs at 1% SWNT with the resulting power conversion efficiency being 0.1%. Although the V_{OC} was the same as in their previous work, this result was a slight improvement in efficiency. At SWNT concentrations higher than 1%, they suggest that the photocurrent decreases due to a lower photogeneration rate because photoexcitation only occurs in the P3OT and not the SWNTs, but the SWNT concentration was sufficiently high enough for charge collection to occur.

The next improvement[66] in their ITO/PEDOT:PSS/P3OT:SWNT/Al device came from experimenting with heat treatment after the deposition of the aluminum layer. They varied the annealing temperature using 40ºC, 75ºC, 120ºC, and 200ºC, keeping in mind the P3OT glass transition temperature is 100ºC, and the P3OT melting temperature is 187ºC.

The hole mobility in polythiophene is known to dramatically increase when it is annealed above it's glass transition temperature due to the increase in the degree of ordering so an increase in I_{SC} was expected. The results from the 5 minute annealing

batches showed that the I_{SC} increased with annealing temperature until the 200ºC test where it was much less than the non- annealed device. The V_{OC} was not affected by annealing except in the 200ºC test where it also dropped considerably. The best results were obtained at 120ºC which is above the glass transition temperature and below the melting temperature with the resulting power conversion efficiency at 0.22%.

Additionally, they found a red shift in the absorption spectrum after annealing above the glass transition temperature due to the P3OT changing to an ordered phase with a higher crystallinity. The crystallite size increases with temperature, giving the P3OT morphology a longer average conjugation length which causes the red shift.

As for annealing times it was found that at 120ºC the device efficiency increased sharply up to a maximum efficiency between 5 and 10 minutes, and then declined at a slower rate. Beyond 25 minutes, the efficiency drops below the value before annealing started and the damage is irreversible.

The results from the Kymakis and Amaratunga P3OT:SWNT devices demonstrate the feasibility of conjugated polymer functionalized carbon nanotube blends as the bulk heterojunction layer in an organic solar cell. However, the performance is still more than one order of magnitude lower than a comparable device using fullerenes as the acceptor material. It was suggested[66] that the limited performance can be attributed to the presence of a substantial amount of metallic chirality nanotube and that they can provide a pathway for unwanted electron-hole recombination due to the lack of a band gap. They went on to suggest that a device containing SWNTs with mostly semiconducting chirality could have the nanotube concentration increased to be closer to the percolation threshold, which is between 4 and 11 wt%, without causing additional recombination and a higher photocurrent would be achieved due to a higher exciton diffusion efficiency.

Bulk heterojunctions using SWNTs have been studied by a few other research groups and it is useful to compare the different approaches and results. In a study by J.A. Rud, et. al.[67], they utilized a water soluble derivative of polythiophene (Sodium poly[2-(3-thienyl)-ethoxy-4-butylsulfonate]), blended it with SWNTs, and deposited a film onto fluoride-doped tin oxide (FTO) by drop casting, with the aluminum top electrode deposited by sputtering. The thickness of the active layer was measured to vary between 2.5 and 8.5 μm, and this large thickness was necessary to prevent complete shunting caused by the conductive SWNT network.

After being drop cast, the SWNTs were aligned during curing using an external electric field and this resulted in a higher I_{SC} compared to the device without the alignment step. The I_{SC} and V_{OC} of this device was very low and despite no fill factor or power conversion efficiency being reported, the efficiency could be roughly estimated and is likely to be a few orders of magnitude lower than that of the Kymakis and Amaratunga devices. Despite the poor device performance, the study feasibly demonstrated the use of water-soluble materials and the alignment of nanotubes using an external electric field to improve the photocurrent.

S. Kazaoui, et. al.[68] fabricated two different ITO/PEDOT:PSS/ polymer:SWNT/Al devices using P3OT and MEH-PPV for the different polymers. The active layer films were deposited by either spin coating or drop casting, and the films were relatively thick, ranging from 0.5 to 1.5 μm, which was likely designed to prevent shunting. The P3OT device resulted in a low V_{OC} at 0.32 V but strangely a very high I_{SC}. Conversely, the MEH-PPV device resulted in a 0.64 V V_{OC} and a very low I_{SC}. While efficiency and fill factor were not explicitly reported in this study, the fill factors can be approximated from

the I-V curves to be relatively low for both devices, thus both devices can be expected to have a power conversion efficiency value below the results of Kymakis and Amaratunga.

The V_{OC} results from this study are not consistent with the 0.75 V result from the Kymakis and Amaratunga devices also using a P3OT:SWNT blend. The hypothesis that the V_{OC} is a strong function of the difference between the HOMO of the polymer and the work function of the SWNTs would predict that the results from different groups using the same materials should be closer than what was demonstrated here. Even more interesting is that HOMO level of MEH-PPV is 4.9 eV[69] which is lower than that of P3OT, but the MEH-PPV device in this study had a much larger V_{OC} despite the smaller difference between the HOMO of the polymer and the work function of SWNTs. It is clear that there must be other underlying factors that strongly influence the V_{OC} of these devices that are still yet to be explained.

An additional experiment in this study was the fabrication of two MEH-PPV:SWNT devices using SWNTs from different growth techniques. They reported that HiPco SWNTs resulted in approximately double the V_{OC} and I_{SC} of the same device using CoMoCat SWNTs, and they suggested that the difference might be attributed to HiPco SWNTs absorbing light from deeper into the infrared range.

The use of flexible substrates was demonstrated by B.J. Landi, et. al.[70] in their study of polymer:SWNT solar cells on flexible ITO coated PET instead of the more common ITO coated glass as the bottom electrode. A mixture of P3OT with 1% SWNTs was prepared with mixing and ultrasonication steps. A pure P3OT layer was formed on the ITO surface by spray deposition, followed by the bulk P3OT:SWNT layer which was also formed by spray deposition, and the device was capped with an aluminum electrode. The ITO/P3OT/P3OT:SWNT/Al device produced a 0.98 V V_{OC}, which is considerably higher

than the results of Kymakis and Amaratunga using P3OT:SWNTs. They suggested the relatively high V_{OC} might be explained by differences in the purity and defect density of the SWNTs, but no further details were provided. The reported I_{SC} was lower than the Kymakis and Amaratunga results, and since the fill factor appears to be considerably lower from an estimate using the I-V curve, it is likely that the power conversion efficiency is still lower than the Kymakis and Amaratunga results despite having a high V_{OC}.

R.L. Patyk, et. al.[71] fabricated a hybrid device combining both the bilayer and bulk heterojunction concepts. Polybithiophene (PBT) with a 160 nm layer thickness was electrochemically deposited on an FTO substrate. SWNTs were purified by HNO_3 treatment which adds carboxylic groups to defects and edges, and these defect sites were further functionalized by 2(2-tienyl)ethanol (TIOPH). The nanotubes were dispersed in toluene and mixed with P3OT to create a 5 wt% nanotube amount in the TIOPH-SWNT:P3OT blend. This blend was spin coated with a 200 nm layer thickness onto the PBT surface. The top electrode was thermally evaporated aluminum and a second device was prepared with a calcium/aluminum electrode.

In this FTO/PBT/P3OT:TIOPH-SWNT/Al structure, photoexcitation can occur in both the PBT and the TIOPH-SWNT:P3OT layers. However, exciton dissociation will likely only occur at the interface between the two layers and at any SWNT:P3OT interface. Hole conduction occurs in the polymers while the SWNTs act as electron charge transporters. The use of PBT and its 160 nm layer thickness was chosen because it had been reported elsewhere in a FTO/PBT/Al device of the same thickness to produce a high V_{OC} at 2 V. An additional purpose of the PBT layer is that the insertion of a

continuous polymer layer between the FTO electrode and the layer containing metallic SWNTs was expected to hinder the occurrence of low shunt resistance.

The results from this FTO/PBT/P3OT:TIOPH-SWNT/Al device was a V_{OC} at 1.02 V with the power conversion efficiency at 0.38%. The same device with the Ca/Al electrode resulted in a higher performance with the V_{OC} at 1.81 V and the power conversion efficiency at 1.48%. While a higher V_{OC} was expected because calcium has a very low work function at 2.9 eV, the result was similar to the work of Kymakis and Amaratunga with different electrodes in that the change of electrode work function affected the V_{OC} by less than the difference between the Ca and Al work functions. These results produced a relatively high power conversion efficiency for a polymer:SWNT device and demonstrate the successful application of calcium electrodes to significantly improve the device properties.

From all these examples of the recent developments in organic solar cells using polymer:SWNT bulk heterojunctions, it is clear that the field is still very young. The results from such device fabrication studies are generally not well understood and the types of explanations for the underlying mechanisms that get reported are merely hypotheses and suggestions with little or no data to support them. At this proof-of-concept stage in the field, any device that functions as a solar cell, no matter how poorly, is worthy of publishing and becomes an important contribution towards developing a basic understanding of the mechanisms that take place in these devices. There is no scientific consensus to explain the exact origin of the open circuit voltage or to calculate its magnitude. Short circuit current densities are typically just fractions of those from well established organic solar cell devices, which themselves are still a young technology in

comparison to inorganic solar cells. Fill factors are usually low and the devices have poor rectification properties as well as high series resistance and low shunt resistance.

Efficiencies below 1% are still normal for SWNT bulk heterojunctions while the best organic solar cell as of the April 2010 efficiency tables publication has reached 7.9% efficiency.[6] This record is from the same research group that recently reported a 7.4% device using a ITO/PEDOT:PSS/ PTB7:$PC_{71}BM$/Ca/Al structure and the newer record is likely very a similar design.[72] The structure of PTB7 is provide in Figure 20 and it is a very well optimized polymer with tailored HOMO/LUMO levels and strong absorption properties in the most intense range of the solar spectrum. [72] For a structure that may have the potential to out-perform fullerenes, carbon nanotubes device research has a lot of catching up to do.

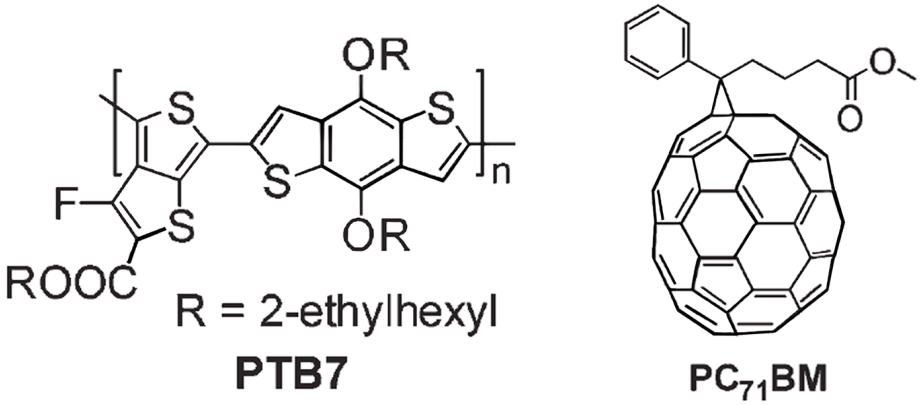

Figure 20 - The structures of PTB7 and PCBM using the C_{71} fullerene.[72]

It is not clear which materials will become the top performers because there are still many other hidden variables that limit the device performance. However polythiophene derivatives appear to be a popular choice at the moment in both SWNT devices and in more established fullerene devices. Methods of nanotube functionalization and solution preparation also vary with each research group since there is no clear best practice. A variety of film fabrication techniques have been deployed and although spin coating

appears to be the most common for laboratory cells, larger scale and more precise fabrication techniques such as inkjet printing are likely to become the preferred method for commercialization. Among the other film fabrication techniques, electrodeposition has received little attention in this application despite its many strong attributes.

2.7 Electrophoretic Deposition

Electrodeposition generally refers to the process of coating an electrode by using an applied electrical potential difference to move and deposit charged species. Deposition can occur on either the negative cathode or the positive anode depending on the charge of the suspended material. Electrodeposition can be subdivided into electrolytic deposition (ELD) and electrophoretic deposition (EPD). Electrolytic deposition, most commonly known as electroplating, utilizes a current to drive redox reactions involving ions from a metal salt solution to produce a metal or ceramic coating on one of the electrodes. Electrophoretic deposition, depicted in Figure 21, uses a power supply to apply an electric field which drives the motion of charged particles through a solvent towards an electrode substrate where deposition can occur. Ceramics, small molecules, metals, alloys, polymers, macromolecules and composites of those materials have all been deposited using electrophoretic deposition techniques.[73-75]

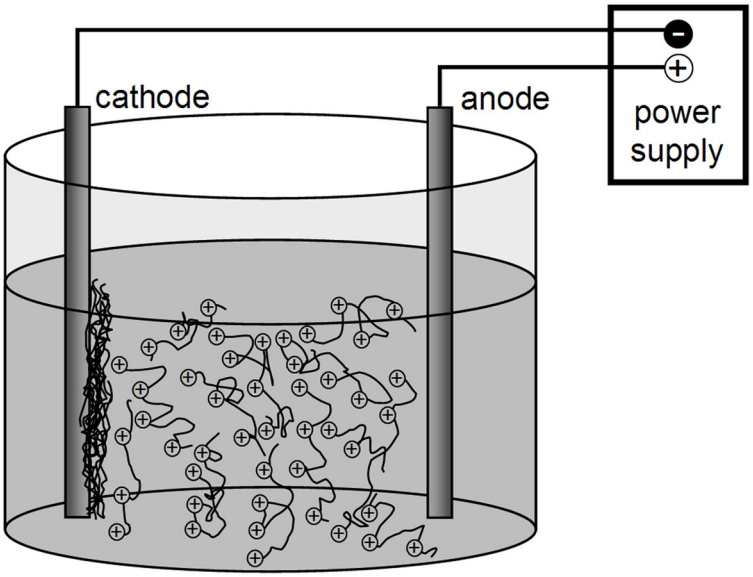

Figure 21 - Schematic diagram of the general electrophoretic deposition setup, depicting the cathodic deposition of positively charged polyelectrolytes from solution in a beaker.

Electrophoresis is the motion of charged particles in a stable suspension under the influence of an electric field, but it is not responsible for deposit formation of the material at the substrate electrode. There are a variety of mechanisms that can cause the formation of a film and it is not as simple as putting a suspension of charged material between two electrodes and expecting a nice coating to be produced.

Deposition mechanisms may involve such phenomena as particle accumulation and coagulation, flocculation, charge neutralization, cross linking, gelling, and electrode reactions.[74, 76] The control of such mechanisms require the manipulation of solvents, pH, the use of additives, and tuning the deposition parameters such as voltage, current density, temperature, time, and the distance between electrodes. The application of deposition strategies is best illustrated by examples.

2.7.1 Examples of polymer electrophoretic deposition

Electrophoresis requires charged materials in a stable suspension, so the deposition of polymers typically requires that they carry a charge. A polymer that contains charged

functional groups is called a polyelectrolyte and just like acids or bases, polyelectrolytes can be classified as strong or weak. Strong polyelectrolytes have functional groups that dissociate completely in solution and their ionization is constant across nearly all pH values.[75] However, only a portion of the ionizable functional groups of a weak polyelectrolyte are ionized and the degree of ionization is determined by the pH of the solution.[75]

An example of a strong polyelectrolyte is Poly(diallyldimethylammonium chloride) (PDDA) and the reason for it's high ionic strength is that it contains a quaternary ammonium cation group which holds a positive charge and completely dissociates over a wide pH range.[74] If the polymer has lower degree amine functional groups it becomes a weak polyelectrolyte because the nitrogen atoms can be protonated in the presence of acid and because there is a variable degree of pH-dependent protonation.[75] At higher pH, the polycation groups can be deprotonated to become neutrally charged as demonstrated in the following reactions[75]:

Amine-polyelectrolyte protonation:

$$\text{polymer} \bullet NH_2 + H_3O^+ \rightarrow \text{polymer} \bullet NH_3^+ + H_2O \quad \text{(EQ6)}$$

Amine-polyelectrolyte deprotonation:

$$\text{polymer} \bullet NH_3^+ + OH^- \rightarrow \text{polymer} \bullet NH_2 + H_2O \quad \text{(EQ7)}$$

Some examples of weak polyelectrolytes with primary amine functional groups are poly(vinylamine) (PVA), poly(allylamine hydrochloride) (PAH), and chitosan (CHIT), while poly(ethyleneimine) (PEI) is a weak polyelectrolyte containing all secondary amines, and the branched form of PEI contains primary, secondary, and tertiary amines.[75]

Electrophoretic deposition experiments of pure PDDA result in no deposit formation because while electrophoresis is responsible for charge transport and increasing the concentration of PDDA at the cathode, there is no mechanism for deposition since there is

strong electrostatic repulsion between polymer chains.[75] To overcome this, Zhitomirsky and Petric[76] found a way to deposit PDDA by co-deposition starting from the addition of metal salts.[76] Metal hydroxide particles were produced from cathodic electrolytic reactions and the oppositely charged PDDA adsorbs on the surface of the particles resulting in the heterocoagulation of the hydroxide-PDDA composite on the cathode with the polymer acting as a binder.[76] This ceramic particle electrosynthesis and PDDA co-deposition is not limited to metal hydroxides and has also been demonstrated with oxides such as iron oxide.[77]

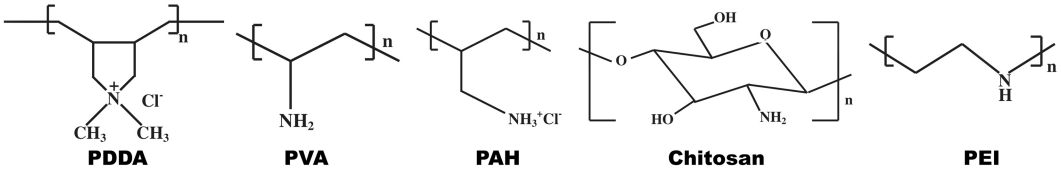

Figure 22 - Chemical structure of some amine-based polyelectrolytes.[75]

Before discussing the deposition of weak polyelectrolytes, it is important to understand the electrochemical reactions that occur at the electrodes. Some reactions consume H^+ such as $2H^+ + 2e^- \rightarrow H_2(g)$, and result in a minor local pH increase. The more dominant reduction reactions consume water and electrons to produce hydroxide and these significantly increase the pH locally at the cathode, for example the reduction of water, dissolved oxygen, or ions containing oxygen such as nitrate or perchlorate[74]:

$$2H_2O + 2e^- \rightarrow H_2(g) + 2OH^- \quad \text{(EQ8)}$$

$$O_2(aq) + 2H_2O + 4e^- \rightarrow 4OH^- \quad \text{(EQ9)}$$

$$NO_3^- + H_2O + 2e^- \rightarrow NO_2^- + 2OH^- \quad \text{(EQ10)}$$

Even if the pH of the bulk solution is acidic, the pH within 100-200 μm of the cathode surface has been reported to be up to 12 as a result of these reduction reactions.[74] However, the net pH of the bulk doesn't change significantly because there are similar

oxidation half cell reactions that occur in the vicinity of the anode surface such as the electrolysis of water which produces H^+ resulting in a local pH decrease at the anode:

$$2H_2O \rightarrow O_2(g) + 4H^+ + 4e^- \quad \text{(EQ11)}$$

The EPD of many weak polyelectrolytes such as PVA, PAH, CHIT, and PEI utilizes their pH dependent solubility as described by Zhitomirsky[75]. An acidic solution can be used to establish a high degree of amine group protonation and thus a solution of highly positively charged polyelectrolytes. Upon applying voltage between the two electrodes, electrophoresis will carry the cationic polyelectrolytes towards the cathode where there is a local high pH region. The protonated amine groups will be deprotonated by the OH^- ions at the cathode surface and then the polymer will become insoluble and coagulate to form a film on the surface of the cathode. While anionic polyelectrolytes appear to be less common, a similar but opposite approach can also be applied to deposit negatively charged weak polyelectrolytes in an alkaline solution onto the anode due to the loss of solubility in the low pH region.

Sometimes even neutrally charged material can be deposited if it can interact favorably with additives. Zhitomirsky and Petric[76] found a way to deposit polyvinyl alcohol (a neutral polymer) on the cathode using borax and boric acid additives. Within the low pH region of the cathode it was found that the boric acid reacts with OH^- to produce tetrahydroxyborate ions $B(OH)_4^-$, and borax can also generate some $B(OH)_4^-$ naturally in solution as demonstrated in the following reactions:

Boric acid reacting with hydroxide: $B(OH)_3 + OH^- \leftrightarrow B(OH)_4^-$ (EQ12)

Borax in aqueous solution: $Na_2B_4O_7 + 7H_2O \rightarrow 2B(OH)_3 + 2B(OH)_4^- + 2Na^+$ (EQ13)

The tetrahydroxyborate reacts with polyvinyl alcohol to form a complex with inter-chain cross linking as illustrated in Figure 23 and subsequently, the polymer gels and forms a deposit on the cathode. The complex formation creates a negative charge but the electrostatic repulsion between complexes is effectively screened by the free Na^+ ions from borax dissolution.

The application of electrophoretic deposition to conjugated polymers has received very little attention. The research group of Tada and Onoda appears to be the only group actively studying this specific application of EPD. Their early studies[78, 79] began with the deposition of poly(3-octadecylthiophene) (PAT18) which is a conjugated polymer similar to the well known P3HT and P3OT but with side chains that are 18 carbons in length instead of 6 or 8. The technique involves the creation of colloidal suspensions rather than solutions. PAT18 is soluble in toluene and a 1.0 $g \cdot L^{-1}$ solution was prepared. This was added to acetonitrile, which is not a solvent for PAT18, and the result was a stable 0.1 $g \cdot L^{-1}$ colloidal suspension of PAT18 in 90% acetonitrile with the polymer being enveloped by toluene.

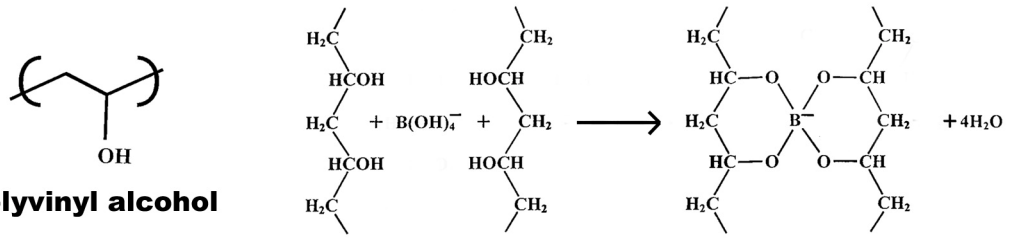

Figure 23 - The chemical structure of polyvinyl alcohol and the complex formation with tetrahydroxyborate.

Photoluminescence spectra indicated that solidification of PAT18 in suspension had occurred. Further confirmation that solid colloidal particles formed is that no deposition occurred in a pure toluene solution, even at very high (200 V across 5 mm) applied electric field, indicating no mechanism for deposition. In the toluene/acetonitrile colloidal

suspension of solid PAT18 particles, electrophoretic deposition occurred on the negative electrode when the applied voltage exceeded 50 V, indicating that the colloidal particles were likely positively charged.

This deposition technique differs significantly from solution-based techniques because the solidification and film formation steps are decoupled. In solution-based EPD and in spin coating the solidification of the material occurs while the film is forming. However in the non-solvent colloidal suspension method, the solidification of PAT18 particles occurs upon mixing the solution with the non-solvent. The film formation is a second step with the application of an electric field and subsequent electrophoresis of the solid particles towards the electrode where they are heavily concentrated, likely to the point where the acetonitrile is squeezed out and a solid film forms. It was suggested[80] that when the acetonitrile evaporates from the surface upon drying, a small amount of residual toluene remains and it may partially dissolve the surface of the polymer particles which enables them to bond together and form an adherent film.

Tada and Onoda extended this colloidal suspension approach to three other conjugated polymers[80-82]; poly(9,9-dioctylfluorenyl-2,7-yleneethynylene) (POFE), poly[(9, 9-dioctyl-2,7-divinylene fluorenylene)-alt-{2-methoxy-5-(2-ethylhexyloxy)-1,4-phenylene}] (PDOF-MEHPV), and MEH-PPV. C_{60} was also deposited by this method as well as mixtures of C_{60} and the various conjugated polymers in their experiments. The electrophoretic deposition of these species resulted in films on the positive electrode, indicating that the colloidal particles are negatively charged in suspension. Their co-deposition of conjugated polymer with fullerenes demonstrates the application of this EPD technique to donor-acceptor organic devices.

Tada and Onoda's non-solvent colloidal suspension EPD technique has clear advantages over spin coating. Much thicker coatings can be formed using a low concentration of polymer compared to the thickness of films that can be fabricated by spin coating with very high concentrations of polymer.[83] Additionally, the process is very efficient in terms of material consumption. It was found that up to 98% of the polymer in suspension could be deposited onto the substrate, and this is vastly superior to spin coating where the majority of the material is immediately spun off and wasted.[84]

Compared to EPD in water or alcohol solvents, much higher voltages can be used because toluene and acetonitrile do not contain any ionic species and no electrochemical reactions occur at the electrodes.[85] However, any advantages of these solvents are offset by their toxicity which may reduce large scale feasibility.

2.7.2 Examples of carbon nanotube electrophoretic deposition

Films of carbon nanotubes have also been fabricated using an assortment of EPD techniques. While there are more examples than with conjugated polymers, the use of EPD for nanotube coatings is still relatively new. In most reports, the deposition mechanism is not well understood and often there is no attempt to explain exactly how film formation occurs.

In a study by Du, et. al,[86] multi-walled carbon nanotubes (MWNT) were suspended in mixed acetone-ethanol solutions with added iodine. No current flow or deposition occurred in pure ethanol with added iodine, but electrophoresis and deposition occurred successfully in the presence of acetone and was dependent on a reaction between acetone and iodine. It was found that iodine reacts with acetone in a double displacement reaction to produce HI, which then dissociates to produce H^+ and I^- ions.[86, 87] It was suggested that H^+ adsorbs to the MWNT surface giving the MWNTs the positive charge required to

move towards the cathode under the influence of the electric field where much of the adsorbed hydrogen atoms as well as free H^+ ions get reduced and combine to form H_2 gas, leaving the neutral nanotubes to coagulate and bundle together.[86]

Large 70 μm pores were found in the MWNT films at high acetone concentration (100% and 2:1), but when the acetone-ethanol concentration ratio was 1:1 the pores were nearly eliminated with only 1 μm sized pores remaining. At lower acetone concentrations the deposition rate was much lower and there was poor adhesion to the substrate. It was suggested that the porosity is the result of the formation of H_2 gas at the cathode during deposition. The decrease in porosity as the acetone concentration decreased is likely the result of less free H^+ ions in solution. The iodine most likely does not react with ethanol and therefore less acetone should result in less H^+ ions and ultimately less H_2 generation at the cathode.

Another unique approach is that of Kamat et. al,[88-90] where the deposition mechanism is claimed to be the result of nanotube polarization. SWNTs were mixed in a THF solution with Tetraoctylammonium bromide (TOAB) which dissociates into a quaternary ammonium cation and Br^- in solution. The TOAB solublizes the nanotubes in THF to form a stable suspension after ultrasonication, with the nanotubes still persisting in bundles. It was suggested that the electric field aligns and polarizes the SWNTs such that the end pointing towards the cathode is more positive and the end pointing towards the anode is more negative. They go on to hypothesize that the free bromide anions in the solution are electrostatically attracted to the positive end of the SWNTs and therefore screen the positive charges such that the nanotubes have a net negative charge and move under the influence of the electric field towards the anode. It was also suggested that the

TOAB rearranges itself to accommodate the dipole and this enables aggregation when the nanotubes are gathered at the electrode.

It was found that at very high electric fields the nanotube bundles would align in aggregation parallel to the field such that large visible tendrils grew outward from the positive electrode towards the opposite electrode until the field was turned off.[90] This phenomenon further supports the explanation of polarization and dipole attraction between different bundles.

The most commonly demonstrated[91-96] EPD technique to create carbon nanotube films is very similar to the previously described deposition of weak polyelectrolytes. Molecules, macromolecules, or polymers with functional groups containing pH dependent solubility can be attached to the nanotube surface through covalent or non-covalent bonding. The functionalization typically imparts sufficient solubility to the nanotube as well exfoliation of individual nanotubes from their bundles due to electrostatic and steric repulsion. The charge of the functional molecule enables the electrophoresis of the nanotube towards the oppositely charged electrode. Deposition can occur if the pH is locally modified at the working electrode because the charge is sensitive to excess H^+ or OH^-. Lewis acids and bases can also be used in the charging and deposition mechanic in addition to the more common Brønsted acids and bases.

There are many applications where carbon nanotube films do not need high purity or the nanotubes are used to enhance the properties of the matrix material. A common strategy in the EPD of carbon nanotubes that has been reported[97-102] is the co-deposition with other materials. This method utilizes an excess of polymers or ceramic particles that are charged in solution or stable suspension and are capable of attaching to the nanotube surface. The applied electric field acts on the charged species to cause the electrophoresis

of both the functional material and the attached nanotubes towards the oppositely charged electrode. The deposition mechanism is usually controlled by the same mechanism used for the functional material without nanotubes, but in some cases the nanotubes can enhance the film formation by for example being receptive to H-bonding from hydroxide ions attached to the electrode surface.[102]

There is a notable study by Itoh, et. al,[103] where SWNTs and conjugated polymers were co-deposited using the previously described non-solvent method of Tada and Onoda. SWNTs and P3OT (or MEH-PPV) were each dispersed separately in toluene by ultrasonication, and then measured amounts were poured into acetonitrile which is not a solvent for the materials. A colloidal suspension formed with the SWNTs and P3OT enveloped by toluene in the acetonitrile solution. Deposition occurred on the negative electrode and it was suspected to be due to positive charging of P3OT in the same film formation mechanism as in the Tada and Onoda studies. It is important to note that the nanotubes were not likely separated from their bundles or very well functionalized and the resulting film structure is likely to be clusters of SWNT bundles surrounded by P3OT matrix material rather than a finely mixed film of individual SWNTs. After nanotube alignment induced by an applied external electric field during a heat treatment, the resulting film of nanotubes surrounded by the conducting polymer demonstrated field emission properties.

2.8 Literature Gaps and Potential Contributions

From thorough investigation it is apparent that there are many gaps in the current literature in the topics that are directly relevant to the work that is discussed in this thesis. While the electrophoretic deposition of polymer is not new, it appears that only the group of Tada and Onoda has demonstrated the use of EPD in the formation of conjugated

polymer films as well as Itoh[103] who adopted their technique of the colloidal suspension in a non-solvent. The EPD of conjugated polymers from solution has not yet been demonstrated and nether has the EPD of conjugated polymers using non-toxic solvents.

Carbon nanotubes have been electrophoretically deposited in water, and polymer functionalized carbon nanotubes have also been deposited. However, there appears to be no published results of the EPD of carbon nanotubes that are functionalized with conjugated polymers. While the work of Itoh et. al.[103] comes close with their co-deposition using a colloidal suspension in a non-solvent, the nanotubes do not appear to be functionalized. The deposition of conjugated polymer functionalized carbon nanotubes is also yet to be demonstrated from solution and using non-toxic solvents.

There is also very little information about the use of EPD in organic solar cells. There are some studies that utilized EPD in the fabrication of photoelectrochemical cells and dye-sensitized solar cells, but there appears to be no published application of electrophoretic deposition for the fabrication of the active layer in a solid-state organic photovoltaic cell.

The work in this thesis addresses these gaps in the current literature by demonstrating the EPD of a conjugated polymer from solution in non-toxic solvent, as well as the EPD in similar conditions of carbon nanotubes that are functionalized with a conjugated polymer. These EPD techniques are then applied to the fabrication of films for the application of the photoactive layer in a bulk heterojunction organic solar cell. The efforts here will enable progress in the device fabrication by establishing procedures and recommending further courses of action based on preliminary device fabrication experiences.

3. Materials and Methodology

3.1 Materials

3.1.1 Conjugated polymers

The long term project plan extending well beyond the work involved in this thesis is for the implementation of 4 different conjugated polymers as the electron donor material into a bulk heterojunction organic solar cell with carbon nanotubes as the acceptor material. Each of the planned polymers has a different absorption peak so that the composite will be capable of absorbing the majority of light from the solar spectrum spanning from infrared to ultraviolet. The proposed conjugated polymers (Figure 24) have been synthesized by the Adronov group in the department of Chemistry & Chemical Biology at McMaster University. Due to the quaternary ammonium cation functional groups, all of these polymers are strong polyelectrolytes and carry a positive charge. The expected maximum absorption peaks and band gaps for these structures are given in the figure, showing broad coverage across the solar spectrum.[I]

Multiple conjugated polymers could be implemented into a single device in a layered method or in a mixed bulk method. Electrophoretic deposition is capable of fabricating both a multi-layer bulk heterojunction structure and co-depositing the materials for a mixed bulk heterojunction.

[I] Absorption values are estimated from the solution data of similar structures that have been reported. (Research Proposal from Dr. Alex Adronov: Dept. of Chemistry and Chemical Biology, McMaster University, 2008.)

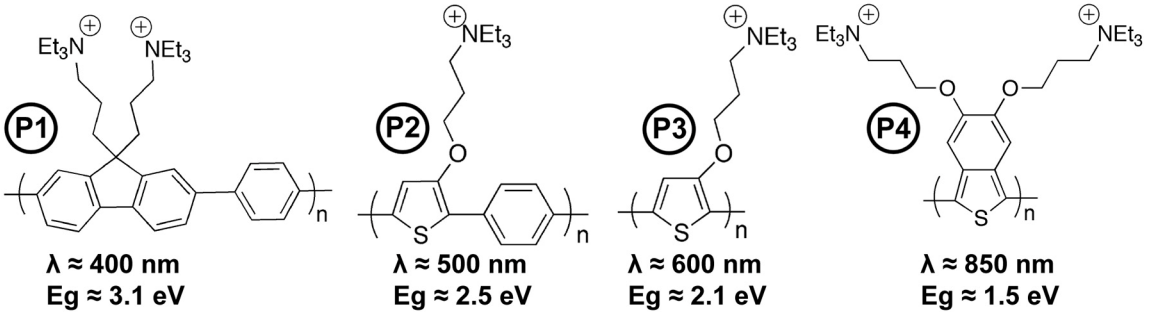

Figure 24 - Conjugated polymers synthesized by the Adronov group, showing the expected approximate maximum absorption wavelength and band gap for each. (Adronov 2008)

Since photons carrying less energy than the band gap of a material are transparent to that material, a layered structure could be utilized with the highest band gap material on the top layer followed by the lower energy level materials in decreasing order. In this construction, each layer absorbs the light of energies at and above its band gap but without the excessive thermalization losses as previously described in the literature review. With each of the four polymers able to functionalize SWNTs, the four active layers could be a bulk heterojunction composed of free conjugated polymer and polymer functionalized SWNTs for each polymer type, forming a bicontinuous network of donor and acceptor material.

Instead of four unique layers, the mixed bulk heterojunction method would be one layer containing a fine mixture of all four types of free conjugated polymers and polymer-functionalized SWNTs. It is suspected that energy transfer from the highest energy gap to the lowest energy gap polymer could occur efficiently through a Förster-type resonant energy transfer (FRET) mechanism.

Before these long term experiments can become a possibility, it is first necessary to establish the successful deposition of one of these polymers and of SWNT composites as well as the development of preliminary procedures for photovoltaic device fabrication using these materials. The polymer that is utilized in the work of this thesis is P1 from

Figure 24 and also a slightly modified version of P1. Both P1 and the variant were designed, synthesized, and provided by the Adronov group.

3.1.2 Carbon nanotubes

The purified grade single-walled carbon nanotubes (SWNTs) used in this work were synthesized using the high pressure carbon monoxide (HiPco) method by Carbon Nanotechnologies, Inc. of Houston, Texas. SWNTs were not modified prior to functionalization with the conjugated polymer. This is notable because SWNTs are occasionally covalently functionalized with small carboxylic acid groups at defect sites and also shortened by acid cutting.

3.1.3 Substrates for electrophoretic deposition

Electrophoretic Deposition was performed onto a variety of substrate materials depending on the needs of the experiment. The various materials are stainless steel, ITO-coated glass, platinized silicon wafer, and gold-coated quartz crystal.

Rolled stainless steel sheet was used for general electrophoretic deposition experimentation to keep costs down in the scenarios where the substrate properties were not important beyond being conductive and corrosion resistant.

Indium tin oxide (ITO) coated glass substrates were utilized for the development of photovoltaic device fabrication procedures, some scanning electron microscope (SEM) surface and cross sectional imaging, coating absorption spectroscopy, and optical profilometry thickness measurements. The substrate is rigid, smooth, transparent, and the ITO surface is electrically conductive. ITO is a solid solution typically composed of 90 wt% In_2O_3 and 10 wt% SnO_2.

Platinum coated silicon wafers were used to create SEM cross sectional specimens. The advantage of this substrate material is that the wafer can be cleaved in a straight line to create a reasonably flat cross sectional specimen and without significantly damaging the deposited material. The 150 nm platinum coating top layer provides a conductive surface to enable electrophoretic deposition, and there is also a 30 nm titanium layer for adhesion followed by a SiO_2 base layer.

A gold coated AT-cut quartz single crystal substrate from Seiko was utilized in the in-situ microbalance experiments. Small changes in the mass of the material deposited on the surface of the crystal cause changes in the crystal's vibrational frequency, which can be measured and used to calculate the change in mass in small time interval steps.

3.1.4 Additional materials for device fabrication

Organic photovoltaic device fabrication requires additional materials to be deposit as buffer layers. Poly(3,4-ethylenedioxythiophene):poly(styrenesulfonate) (PEDOT:PSS) obtained from H.C. Stark goes by the trade name "Baytron P". This material was used as a buffer layer between the ITO and active layer and it was deposited by spin coating onto ITO-coated glass.

Lithium Fluoride (LiF) and Bathocuproine (BCP) crystals were deposited by thermal evaporation onto the active layer of the photovoltaic device as a buffer layer to the top electrode. Pure aluminum pellets were also thermally evaporated to form the top electrode layer of the devices.

3.2 Methodology

3.2.1 Electrophoretic deposition setup

Electrophoretic deposition (EPD) took place at room temperature in a 50 mL beaker[J] (for most experiments) with a Teflon specimen holder sitting on top of the beaker. There were electrically conductive clips to hold the electrodes on the bottom side of the holder and they were connected on the top side to the power supply by alligator clips and wires. For cathodic EPD, the anode was a 30 mm x 50 mm platinum sheet and the cathode substrate was 35 mm x 50 mm. The distance between the two parallel sheet electrodes was 14 mm, and approximately 30% to 70% of the electrode was submerged in the solution, depending on the liquid volume.

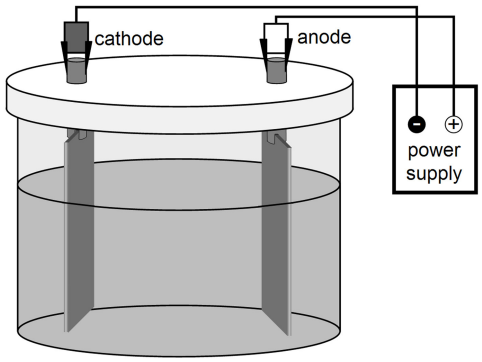

Figure 25 - Setup of electrophoretic deposition experiments.

Deposition was performed under constant voltage conditions with the voltage range typically between 5 V and 80 V. Deposition times varied from 30 seconds to 15 minutes.

[J] The ideal beaker size is much larger than the 50 ml beaker because larger beakers (such as a 500 mL) enable the use of larger volumes of the suspension. This practice increases the ratio of excess material to deposited material so that the concentration of the materials in suspension does not change significantly during the deposition experiment or across multiple deposition experiments using the same liquid. However, it was not practical to follow this convention due to the limited quantity of polymer that was available and also due to the need to perform many experiments with different concentrations which required that many different batches were produced.

The solution was typically a water-ethanol mixture varying from 17%:83% to 2%:98% measured by volume, although a wider variety of mixing proportions were initially tested.

3.2.2 Functionalization of SWNTs with polymer

The following was found to be the most effective procedure for the polymer functionalization of single walled carbon nanotubes: 15 mg of single walled carbon nanotubes was added to 100 mL of ethanol in a flask and placed in an ultrasonic bath for 20 minutes to disperse the nanotubes. After the 20 min dispersion, one hour was set on the ultrasonic bath and while the nanotube suspension was being sonicated, 50 mL of 6.0 $g \cdot L^{-1}$ protonated polymer aqueous solution was slowly added to the flask to ensure thorough mixing of dispersed single walled nanotubes with the functionalizing polymer. After the long ultrasonication the nanotubes were fully functionalized by the polymer and the resulting solution was poured into centrifuge tubes and spun for 30 min at 5000 RPM. Following this, the centrifuge tubes were removed with care to avoid shaking the mixture and were left to settle over night. The next day the soluble part of the mixture was extracted by pipette into sealable vials while the small amount of insoluble solid remnants remained settled at the bottom of the centrifuge tube. The resulting solution was 150 mL of 2.0 $g \cdot L^{-1}$ polymer containing 0.1 $g \cdot L^{-1}$ (5%) functionalized carbon nanotubes in a 2:1 mixture of ethanol to water by volume.

3.2.3 Scanning electron microscopy

The microstructure of coating surfaces and cross sections was investigated primarily using a JEOL JSM-7000F scanning electron microscope (SEM). Surface specimens were prepared by simply attaching the coated substrate or a cut piece of it to an aluminum SEM stub held down by silver paste, carbon tape, or copper tape. Cross sectional specimens

were most often deposited on platinized silicon wafer and were prepared for SEM by using a tungsten carbide scriber to press down at the edge of the wafer to crack and cleanly fracture the substrate and coating along a cleavage plane. Ideally the specimens were fractured into thin bars with parallel edges that can be placed on edge onto the SEM stub so that the cross section is level and facing upward. Unfortunately the fracturing rarely produced perfectly shaped edges and the specimens needed to be carefully angled and supported in order to maintain a reasonably flat cross section edge. Staples (cut in half) and layers of carbon tape were often used to align and stabilize the cleaved specimen pieces and silver paste was used to stick them in place and to establish electrically conducting paths from the aluminum stub to the cross section surface.

All SEM specimens were sputter coated with 4-8 nm of platinum using the Gatan Precision Etching Coating System (model 682) to improve surface conductivity and increase electron yield. Imaging the carbon-based coatings without a platinum top coating was found to be very ineffective, even at a low acceleration voltage and beam current.

The SEM was typically operated at a very low acceleration voltage in order to minimize beam damage effects and to decrease the electron penetration distance to increase the spatial resolution. A range of acceleration voltages were experimented with but 1.5 kV was eventually found to be the most effective without sacrificing the brightness beyond a reasonable amount. The low voltage was also paired with a short working distance, in the range of 3.5 mm to 6 mm to achieve a high resolution. A higher working distance was occasionally used when a larger depth of field was required. To further reduce beam damage the alignment, focusing, and astigmatism corrections were always performed slightly to the side of the region that was to be captured in an image.

SEM was often used to measure the thickness of deposited coatings. This was achieved by capturing images of the cross section and then later loading them into graphics software containing a measuring tool. By measuring the scale bar of the SEM image in terms of pixels and using it as a reference length, the thickness (or any other feature size) can be calculated after its pixel length has also been measured. The thickness data that were obtained from SEM image measurements are averages of all the thickness measurements at multiple random locations across the whole image. Additionally, the coatings were generally flat enough that there was very little variance across the individual measurements.

3.2.4 Atomic force microscopy

The microstructure was occasionally studied with an atomic force microscope (AFM) using the Digital Instruments Nanoscope IIIa Multimode AFM, controlled by the Nanoscope v512r5 software.

Nanoscale variations in height are detectable and measurable because of the size, sensitivity, and accuracy of the tip. Specimen preparation is simple and no coatings are required so there is little risk of altering the specimen due to preparation techniques. Additionally, since the data is acquired from the movement of the tip rather than utilizing a powerful electron beam, there are no beam damage effects or difficulties obtaining sharp image data of light elements. Occasionally the interaction of the tip with the specimen can produce artifacts but they are usually easy to detect and are most often a symptom of a damaged AFM tip rather than a damaged specimen. When operated in tapping mode or non-contact mode there is little to no effect to the specimen and the surface usually remains undamaged. Since the factors that produce artifacts in the SEM are different from those in the AFM, the AFM can be useful for verification of SEM data

when there is concern that top coatings and beam damage have potential to manipulate the surface appearance of SEM specimens.

The specific AFM had the option of being equipped with either the "E" scanner for high resolution work with a 15 μm × 15 μm maximum scan range and 3 μm depth limit, or the "J" scanner with a 150 μm × 150 μm maximum scan range and 5 μm depth limit. Both scanners were utilized and selected depending on the needs of the experiment. Tapping mode was used with the E scanner and contact mode was used with the J scanner. Scan rates were typically at or below 0.5 Hz and standard AFM tips were used.

AFM data is displayed in a 512×512 pixel square with a color map for the third dimension. The height data was recorded simultaneously with the deflection data (contact mode) or amplitude data (tapping mode). Both the deflection and amplitude provide the same information but they are measured in different ways due to the nature of the tip movement in the different AFM modes. Deflection data is a measure of how much the tip bends in contact mode and amplitude data is a measure of the amplitude of the tip's oscillation frequency in tapping mode. Both deflection and amplitude changes occur as a result of the changes in height while the tip is scanning and therefore measure the slope, or essentially the derivative of the height data. The deflection/amplitude data does not show a difference between plateaus at different heights, it is insensitive to gradual height changes, and it is very sensitive to variations in height over small distances because they have large slopes. Small hills or valleys are especially observable because the slope changes quickly from a large positive to a large negative value and the color contrast of the two extremes allows finer scale topography to be easily observable. Deflection/amplitude is therefore an appropriate complement to the height data, where gradual changes in height are easily detected but small variations in height are effectively

washed out because the height color map spans a large scale. The deflection/amplitude data also provides a pseudo-natural looking appearance because the data mimics the effect of light shadowing of surface topography.

3.2.5 Quartz crystal microbalance

Study of the deposition rate was conducted using a Quartz Crystal Microbalance, QCM 922 (Princeton Applied Research) controlled by the WinEchem software. The QCM records the change in resonant frequency and resonant resistance of gold-coated AT-cut quartz crystal substrate as material is deposited. The resonant frequency change is proportional to the change in mass of the deposited material; therefore the system can be used to monitor the mass gained vs. time in-situ for an EPD experiment. The resonant resistance is a measure of the fluid viscosity at the interface of the coating surface.

The measured change in resonant frequency can be converted to the change in mass by manipulation of the Sauerbrey equation[104]:

$$\Delta f = -\frac{2f_0^2}{A\sqrt{\rho_q \mu_q}}\Delta m \qquad \text{(EQ14)}$$

where,

$\Delta f \equiv$ the difference between the unloaded and loaded frequencies, $f_0 - f_L$

$f_0 \equiv$ the resonant frequency of the unloaded quartz crystal resonator

$A \equiv$ the active crystal surface area (0.2 cm^2)

$\rho_q \equiv$ the density of quartz (2.648 $g \cdot cm^{-2}$)

$\mu_q \equiv$ the shear modulus of quartz (2.947×1011 $g \cdot cm^{-1}s^{-2}$)

$\Delta m \equiv$ the total mass gained over the active crystal surface area

The QCM device is calibrated for the 9MHz resonant frequency, it is sensitive to frequency changes as small as 0.1 Hz, and it samples as fast as every 0.1 seconds.[105] This

translates to a mass sensitivity in the $ng \cdot cm^{-2}$ range, which is sensitive enough to detect mass changes below the amount of a monolayer of polymeric material or metal.[104]

In the Sauerbrey equation the deposited coating is treated as an extension of the thickness of the quartz crystal. Without additional corrective terms to account for the different acoustic impedance of the coating, the equation is only valid when the frequency change is less than 2% of the uncoated resonant frequency.[104] The equation also assumes that the coating is rigid, has a sharp interface, and possesses an even mass distribution across the crystal surface.[106]

Despite the theoretical constraints, it is still common to apply the standard unmodified Sauerbrey equation to experiments involving non-ideal test conditions. The possibility of error, even when it is likely to be small, is often acknowledged by referring to the resulting mass data as the "Sauerbrey mass" rather than implying that the results are a measurement of the true mass. Regardless of the possible existence of error, the relative comparison between different test runs under similar conditions remains unaffected by the deviation from ideal coatings and surroundings.

The experimental setup, shown schematically in Figure 26, is similar to regular EPD experiments except that the negative terminal of the power supply is connected to the QCM device instead of directly to the electrode substrate. The QCM device ensures that the working electrode is at ground potential and connects it internally through the Teflon specimen holder to the quartz crystal cathode substrate with 0.2 cm^2 area exposed to the solution. In addition to transmitting the current, the QCM device collects data and outputs it to a computer which records and displays the data in real-time.

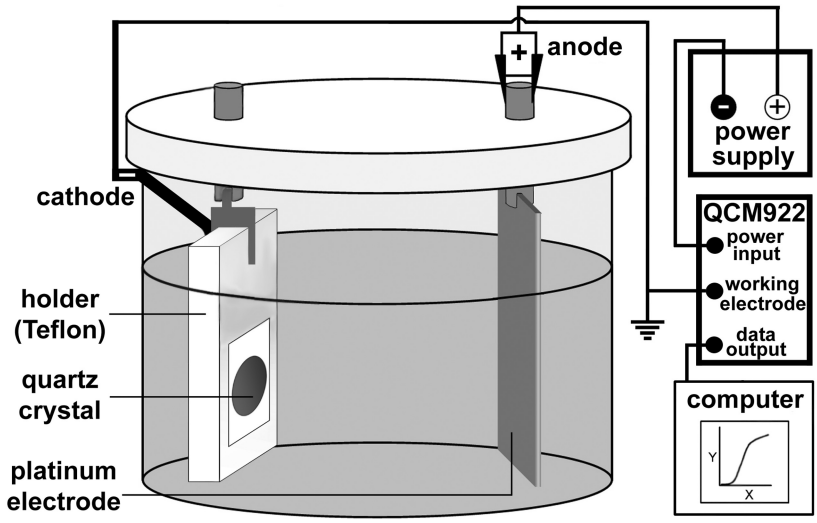

Figure 26 - Schematic of an EPD experiment utilizing QCM.

3.2.6 Absorption spectroscopy

The absorption characteristics of polymer functionalized carbon nanotube coatings were measured using a Varian Cary 50 Bio UV-Visible Spectrophotometer. Absorption spectroscopy was utilized to determine the absorption characteristics across the visible spectrum and slightly into the UV spectrum of electrophoretically deposited coatings with different thicknesses.

The spectrophotometer was calibrated using a blank ITO coated glass substrates to establish the baseline zero and a beam blocker was used to calibrate the full absorption condition. This ensured that the minor absorption effect of the substrate is not included in the absorption data from the coatings.

Absorbance data can be converted to transmittance by utilizing the relationship $A = -\log_{10} \mathrm{T}$. Data presented in this format results in a cleaner looking graph because high absorption spike artifacts from the noisy data of thick coatings are reduced to nearly zero in the conversion. The percent transmittance also utilizes a simple 0-100 percent scale that is easier to interpret compared to absorption data.

4. Results and Discussion

4.1 Cationic Polymer Functionalized Carbon Nanotubes

4.1.1 Introduction

Initial electrophoretic deposition (EPD) experimentation was conducted using a solution of polymer functionalized carbon nanotubes prepared by the Adronov group in the department of Chemistry & Chemical Biology at McMaster University. Using an ultrasonic bath, they mixed single walled carbon nanotubes (SWNTs) in water with a solution of the conjugated polymer that was introduced in the Materials and Methodology section as P1 and is also depicted structurally in Figure 27. After thorough functionalization the suspension was centrifuged to remove any remaining excess nanotubes and other insoluble material and they extracted the soluble part of the solution. The resulting macromolecule is positively charged due to the quaternary ammonium cation on the end of each side-chain.

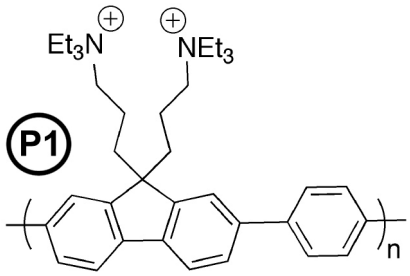

Figure 27 - Cationic conjugated polymer "P1", synthesized by the Adronov group.

Preliminary electrophoretic deposition experiments focused on a range of different conditions using a trial an error iterative approach. Initial conditions were chosen based on the adaptation of common variable ranges that have been found to be successful EPD approaches within the Zhitomirsky research group.

The experimentation was an iterative process by which the results of previous experiments were used to influence the selection of variables for the next experiments. For example in the choice of substrate surface area, the observation that a larger substrate produced a better quality coating led to the adoption of a larger substrate for all further experiments.

Due to the limited quantity of material solution available, especially in the early experiments, a small beaker enabled more experiments to be performed by consuming less material, and this required that the electrodes were also small in order to fit the beaker. Initial experiments attempting a 3 minute deposit at various voltages were performed with 8 mL of solution in a 10 mL beaker using a 5.0 cm × 1.2 cm stainless steel substrate with approximately 1.4 cm^2 exposed to the solution as the deposition surface. These experiments were repeated using a larger substrate with 12 mL of solution in a 20 mL beaker using a 5.0 cm × 2.5 cm substrate with approximately 3.7 cm^2 exposed to the solution as the deposition surface. While the resulting coatings from both sets of experiments were poor quality, the coatings on the larger substrate had a smaller proportion of their surface area affected by edge effects, and they also appeared to have less bubble marks.

4.1.2 Description of experiments

EPD was attempted using the fully concentrated solution, a 25% concentration diluted with high purity water, and two different concentrations diluted with ethanol. For each concentration condition, a variety of voltages between the electrodes were tested ranging from 5 V to 60 V and set to deposit for a fixed time of typically 3 minutes. Deposit time was also varied in some additional shorter and longer duration tests ranging from 1 minute to 10 minutes. Selections of the coatings that resulted from these

preliminary experiments are displayed using photographs in Figure 28, Figure 29, and Figure 30.

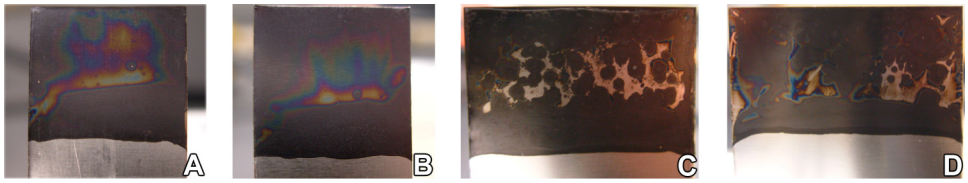

Figure 28 – Photos of the best coatings from the full concentration (as received) EPD experiments. Specimen A and B were deposited for 3 minutes while C and D were deposited for 4 minutes. Constant voltage was set for A, B, C, and D to 10 V, 15 V, 20 V, and 10 V respectively. The specimen codes for A, B, C, and D were T2SS-1, T2SS-3, T5SS-1, and T5SS-2.

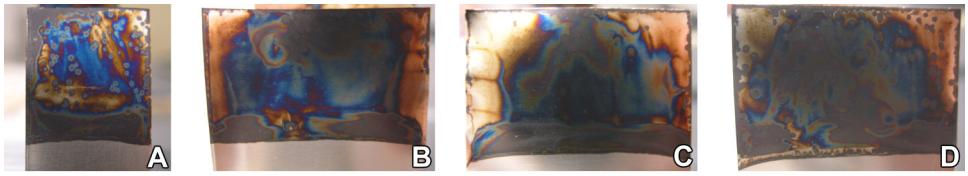

Figure 29 - Photos of the best coatings from the 25% concentration (diluted by high purity water) EPD experiments. All coatings were deposited for 3 minutes. All coatings were deposited for 3 minutes. Constant voltage was set for A, B, C, and D to 35 V, 30 V, 40 V, and 60 V respectively. The specimen codes for A, B, C, and D were T1SS-7, T3SS-5, T3SS-6, and T3SS-7.

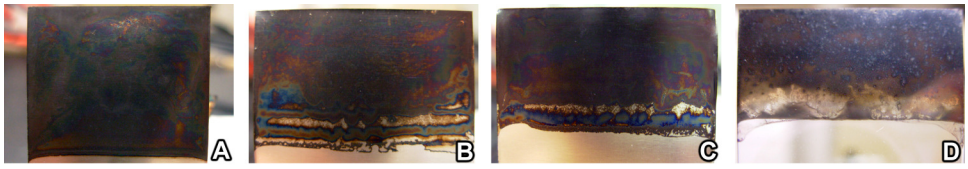

Figure 30 - Photos of the best coatings from the ethanol dilution trial EPD experiments. Coating A was deposited at 35 V for 5 minutes using a solution consisting of 17% concentration of the original solution, 50% water, and 33% ethanol. Coatings B, C, and D were all deposited for 4 minutes using a solution consisting of 67% concentration of the original solution and 33% ethanol. The applied voltages for B, C, and D were 15 V, 20 V, and 20 V respectively. All substrates were stainless steel except specimen D which was deposited on ITO. The specimen codes for A, B, C and D were T4SS-3, T6SS-1, T6SS-2, and T6SS-3.

The preliminary EPD experiments with the cationic polymer functionalized carbon nanotube aqueous solution all yielded poor quality coatings but the observations helped to shape the next set of experiments. It was observed that there is a window for applied voltage where the coating quality is best. If the voltage is set too low then little or no deposition occurs and this is likely caused by a poor driving force for electrophoresis. If

the voltage is set too high then the coating quality suffers due to excessive gas generation at the electrode surfaces from the hydrolysis of water, and also the higher deposition rate could lead to a sub-optimal coating morphology with properties such as high porosity and high roughness. The optimal voltage range changes with the different EPD test variable, for example dilute solutions appear to require a higher applied voltage. Since the high voltage increase H_2 gas formation at the cathode, there were more bubble marks on the coatings from diluted solutions compared to those deposited from the full concentration.

4.1.3 Deposition mechanism

It is speculated that the deposition mechanism is based on the coagulation of material that is concentrated at the cathode surface over time by the electrophoresis of the charged polyelectrolyte. The electrophoresis of the material is driven by the strength of the electric field and this force must also be significant enough to overcome the opposing diffusional force from the resulting induced concentration gradient. Assuming that the local concentration of material required for effective coagulation is independent of the solution concentration, a dilute solution would therefore have a larger concentration gradient than a solution with a higher bulk concentration. Due to the opposition of a larger concentration gradient, the electrophoretic force of the material in a dilute solution would need to be stronger by comparison. Since the electric field is controlled by the applied voltage, this explanation is consistent with the observation that a higher applied voltage was required to deposit material using a dilute solution compared to the fully concentrated solution. As shown in Figure 28 and Figure 29, the best coatings using the fully concentrated solution were obtained in the range of 10 V to 20 V, while the best coatings using the 25% concentration solution were obtained in the range of 30 V to 60 V.

For the high concentration coagulation mechanism to work effectively, the material should not carry a charge that causes electrostatic repulsion. However, the polymer used in these preliminary experiments is a strong polyelectrolyte cation, which means it dissociates completely and the positive charge is insensitive to most reasonable pH values. There is a high pH region at the cathode due to the production of OH^- anions from the electrolysis of water and other similar half-cell reactions described in the literature review. Despite the fact that the quaternary ammonium cation groups at the end of the polymer side chains maintain their positive charge, perhaps the OH^- anions in the high pH region can participate in charge screening of the functional groups in the vicinity of the substrate. With this type of charge screening, the polymer chains would no longer feel electrostatic repulsion and thus high concentration coagulation could be the dominant deposition mechanism in these experiments.

4.1.4 Coatings from ethanol-diluted solutions

The preliminary trials using ethanol to dilute the solution yielded some notable results. The amount of gas generated at the electrodes was much less than when pure water was the solvent and this resulted in less bubble marks on the coating surface as well as it being generally smoother and more homogenously colored. The drying behaviour of the coating after being removed from the solution post-deposition was also considerably better with increasing alcohol concentrations.

The reduction in gas production by adding ethanol is simply due to a lower water concentration and therefore there is proportionally less electrolysis to produce H_2 gas at the cathode and O_2 gas at the anode. Ethanol also has a lower ionic content than water and thus the current density through the solution is also reduced. Additionally, the dielectric constant of the solvent, which is a measure its polarity, is another important difference

between water and ethanol with the values being 80.4 and 24.3 respectively.[107] EPD studies of ceramic suspension have shown that there is an optimal range for the dielectric constant of the solvent where no deposition occurs outside the range.[73] When the dielectric constant is too low there is no deposition because the solvent does not have sufficient dissociative power, and when it is too high the ionic concentration of the solvent causes a reduction in the size of the double layer surrounding the ceramic particles and the resulting electrophoretic mobility is too low.[73] The effect of the dielectric constant on deposition may not be as important as with ceramic materials because the charging mechanism of the polymer is not the surface adsorption of ions, but the amount of ions in solution is still certainly an important factor. Perhaps with fewer ions in solution then there is less charge screening surrounding the strong polyelectrolyte functional groups, which likely affects the electrophoretic mobility.

While there are fewer ions in ethanol compared to water, there are still some dissociated species because a small amount of the alcohol ionizes into an alkoxide and an acid as described in the following reactions of either two alcohol molecules or one alcohol and one water[108]:

$$2RCH_2OH \longleftrightarrow RCH_2O^- + RCH_2OH_2^+ \quad \text{(EQ15)}$$

$$RCH_2OH + H_2O \longleftrightarrow RCH_2O^- + H_3O^+ \quad \text{(EQ16)}$$

In the case of ethanol, the ethoxide anion $C_2H_5O^-$ is fairly stable due to the high electronegativity of oxygen where the charge is localized, and due to this stability ethanol is weakly acidic. In an aqueous solution the ethoxide anion isn't as stable and won't persist because it deprotonates water to once again become ethanol as shown by the following reaction:

$$C_2H_5O^- + H_2O \longleftrightarrow C_2H_5OH + OH^- \quad \text{(EQ17)}$$

If hydroxide ions participate in charge screening to reduce electrostatic repulsions near the cathode and facilitate polymer coagulation, it can be speculated that this process would still function if the alcohol concentration was far greater than the water concentration due to the presence of alkoxide anions. Ethoxide could potentially interact with the quaternary ammonium cation of the polymer side chain in the same way that hydroxide might help to screen the positive charges. In low water concentrations, perhaps ethoxide could be electrogenerated from ethanol at the cathode in the same way as that hydroxide is electrogenerated from water, although certainly to a lesser extent. The following is the proposed half-cell reaction for the generation of ethoxide at the cathode during EPD:

$$2C_2H_5OH + 2e^- \rightarrow H_2(g) + 2C_2H_5O^- \quad \text{(EQ18)}$$

If this half-cell reaction does occur, it happens much less than the electrolysis of water because experimental observation determined that adding ethanol significantly reduced the amount of gas bubbles being visibly generated at the electrodes. However, the electrogenerated gas was not collected or measured so it is plausible that the reaction occurs but the rate is slow enough that large visible bubbles do not form.

4.1.5 Coating drying behaviour: ethanol vs. water

The drying behavior of ethanol compared to water is also an important factor in the improvement of coating quality and there are a few properties that govern this behaviour. It was observed that as the ethanol to water ratio increased, the amount of solvent that remained on the surface after pulling the substrate out of the solution decreased and the drying time also decreased. The drying time depends on the vapor pressure and since

ethanol has a higher vapor pressure than water, it thus has a higher evaporation rate. Surface tension is also important and ethanol has a considerably lower surface tension than water at 0.022 $N \cdot m^{-1}$ and 0.073 $N \cdot m^{-1}$ respectively.[109] Since ethanol has a lower surface tension, the contact angle will be lower and the result is a lower volume of liquid remaining on the surface after the substrate is removed from the solution. Viscosity also plays a role in the volume but the viscosity of water and ethanol are almost equal. Both the lower volume and higher evaporation rate translate to a faster drying time, which reduces the amount of time that the polymer has to re-dissolve back into solution, which is possible with a strong polyelectrolyte.

Another observation when the substrate was removed from the solution containing ethanol was that the residual liquid and deposited polymeric material was less runny. The results of this effect are evident by comparing the dry coatings shown in Figure 29 and Figure 30. The coating from the water-diluted solution appeared to run during drying and more solid material settled in the lower portion of the substrate due to gravity than the upper portion. However, the ethanol-diluted coatings retained the original distribution of material and there did not appear to be any noticeable dripping effects. It seemed that the adhesion of the deposited material may have been stronger and the amount contained in the residual liquid was lesser compared to the water-diluted experiments. Perhaps this is also related to the dielectric properties of the solution and with ethanol having a lower ionic content it may be less able to redissolve the deposited material.

4.1.6 Solution depletion and degradation

After a coating has been deposited, there is less material remaining in the solution than before the deposit. If the volume and concentration of the solution were low enough, then the change in concentration is important to consider. The problem that arises is that

no two deposition experiments with the same solution can be considered to be equal conditions because the concentration decreases after each coating is produced. This problem could have been addressed by using a large beaker and a large excess of solution so that the changes in concentration are insignificant, but unfortunately only very limited quantities of this polymer were available. It was necessary to use small beakers and small amounts of material, so it was important to be mindful of the amount of deposition that can occur before the concentration has changed too much to be comparable.

It was observed in these preliminary EPD experiments that the solution became increasingly more transparent as material was being consumed with each coating. After approximately 4 to 8 coatings, depending on the voltage and time variables, most of the material had been depleted and the solution was no longer producing coatings of comparable quality to the first few coatings of the batch. While most of this result can be attributed to the depletion of the material, there were also distinct observations of solution degradation.

In some cases after an EPD experiment, the remaining solution looked like material agglomeration and precipitation had occurred. As shown in Figure 31, there were many black fiber-like particles and the typically dark colored and homogenous solution became much more transparent aside from the black particles. The fiber shaped particles could be very large bundles of functionalized carbon nanotubes

Nanotube bundling could be caused by induced dipoles or polarization of the nanotubes structures as a result of the electric field. The dipoles would then allow nanotubes to attract and bond via dipole-dipole interactions. This agglomeration effect tended to occur at high applied voltage and with the fully concentrated solution. It was discovered that this effect was partially reversible by placing the solution in an ultrasonic

bath for a few minutes following a deposition experiment. The ultrasonic waves agitate the agglomerate material and destroy the weak dipole bonding, allowing the macromolecules to separate once again. This step was applied after every coating when the remaining solution had any traces of agglomeration. While this process was helpful, it was found to not be perfectly reversible because after a few deposit-sonication cycles the solution was no longer recoverable from it's degraded state.

Figure 31 – [Left] A photo of a functionalized nanotube solution poured into a wide flask after much of the material had precipitated into visible fiber-like particles. [Right] A photo of the original functionalized nanotube solution as received.

4.1.7 Section summary

A solution of cationic polymer functionalized carbon nanotubes was received and attempts to fabricate coatings of the material were performed using electrophoretic deposition under constant voltage conditions. The results of a full concentration, water-diluted 25% concentration, and ethanol-diluted 67% concentration were discussed.

It was found that there is a range of applied voltages that creates the best quality coatings and this range is correlated to the concentration of the solution such that lower concentrations require a higher voltage to produce a coating.

The deposition mechanism is speculated to be the coagulation of material at the cathode as it is highly concentrated due to electrophoresis. It was suggested that OH^- ions

generated by electrolysis reactions might participate in charge screening of the positively charged functional groups on the polymer side chains, which would mitigate the effects of electrostatic repulsion between the macromolecules.

Dilution with ethanol has the effect of smoothing the coating surface by reducing the amount of gas generated at the electrodes and reducing the current density due to it's lower dielectric constant. Ethanol also improves the coating drying behavior due to its lower surface tension and higher vapor pressure compared to water.

It was found that the concentration of the solution depletes after a few coatings have been deposited, and in some cases the quality of the solution also degrades, possibly due to agglomeration via dipole-dipole interactions caused by electro-induced polarization of the material. The solution degradation was partially reversible by ultrasonication, but after enough EPD experiments the solution could no longer recover sufficiently.

4.2 Anionic Polymer Functionalized Carbon Nanotubes

4.2.1 Introduction

Since the coating quality of the cationic strong polyelectrolyte functionalized carbon nanotube solution was poor, the Adronov group prepared a negatively charged version of the same material to test the quality of anodic EPD coatings. The functional group on the side chains of the conjugated polymer, $R-N(Et)_3$ was instead synthesized to be sodium sulfonate, $R-SO_3Na$. In this structure two of the oxygen atoms are double bonded to sulfur and the third oxygen has a single covalent bond to the sulfur and an ionic bond to the sodium atom. In solution the sodium atom dissociates and the side chain functional group becomes $R-SO_3^-$, which is a negatively charged strong polyelectrolyte because of

the stability of the sulfonate anion. In anodic EPD, electrophoresis causes the negatively charged ions to move toward the anode substrate.

4.2.2 Description of experiments

Anionic EPD was attempted using the fully concentrated solution, and ethanol-diluted solutions with 40% and 67% concentration of the original solution as received. Similarly to the cationic experiments, a variety of voltages between the electrodes were tested ranging from 5 V to 30 V and set to deposit for a fixed time of 2, 3, or 4 minutes. Selections of the coatings that resulted from these preliminary experiments are displayed using photographs in Figure 32 and Figure 33.

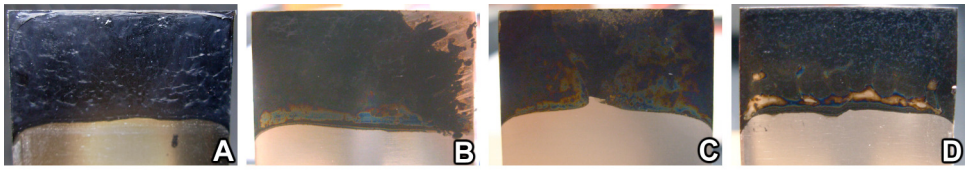

Figure 32 - Photos of the best EPD coatings from the full concentration (as received) of the anodic solution. Specimen A and B were deposited for 4 minutes each while C and D were deposited for 1 and 2 minutes respectively. Constant voltage was set for A, B, C, and D to 15 V, 5 V, 10 V, and 5 V respectively. The specimen codes for A, B, C, and D were T7SS-1, T T7SS-2, T7SS-3, T7SS-4.

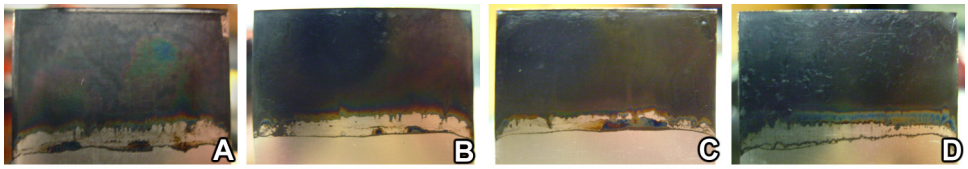

Figure 33- Photos of the best EPD coatings from the ethanol-diluted 67% concentration anodic solution. Specimen A and B were deposited for 2 minutes each while C and D were deposited for 4 minutes each. Constant voltage was set at 15 V for A, while B, C, and D were all set to 20 V. The specimen codes for A, B, C, and D were T8SS-3, T T8SS-5, T86SS-6, T8SS-8.

Notable differences were observed from these preliminary experiments using the anionic version of the strong polyelectrolyte functionalized nanotube solution compared to the original cationic solution. The voltage range required to obtain the best deposits was between 5 V and 15 V for the fully concentrated solution and 15 V to 20V for the

ethanol-diluted 67% of full concentration solution. Both of these ranges are slightly lower than those of the cationic solution under equivalent conditions. It was also evident that the deposition rate of the anionic solution is considerably higher than the cationic solution, even at lower voltages, and in some cases the deposition rate was too fast.

Comparing the coating quality to that of the cationic EPD, the anionic EPD coatings appear to be slightly better quality. In the best anionic specimens the visible uniformity is an improvement with the coating appearing mostly matte black, but there are still notable colorful interference effects which indicate inconsistent film thickness across the coating area. Part of the improvement in quality might come from the noticeable reduced gas production at the anodic substrate.

The ethanol-diluted coatings continued to follow the apparent trend that a lower concentration solution requires a higher voltage to be deposited. Compared to the fully concentration solution, the deposition rate was slower and the coatings were thinner but also more homogenous. Experiments with a higher ethanol concentration and even lower material concentration at 40% of the original solution yielded even smoother coatings but they were very thin and translucent. As observed with ethanol in the cationic solutions, the drying behaviour of ethanol-diluted anodic solutions shared the same benefits.

4.2.3 Deposition mechanism

It is suspected that the deposition mechanism for the anionic functionalized nanotubes is the same as the cathodic version but oppositely charged. Electrophoresis drives the negatively charged macromolecules towards the anode where they concentrate and coagulate. In this situation the same question arises about electrostatic repulsion between all the negative charges of the polymer side chain end groups. At the anode the

water electrolysis half cell reaction produces oxygen gas but also hydrogen ions: $2H_2O \rightarrow O_2(g) + 4H^+ + 4e^-$

Perhaps the H^+ ions, or more likely H_3O^+, are electrostatically attracted to the sulfonate anion and thus screen the negative charges from repelling each other, allowing the coagulation of the macromolecules to occur at high concentration.

4.2.4 Coating quality

Part of the reason for the improved coating quality is likely due the fact that half as much oxygen gas is generated at the anode as the amount of hydrogen gas that is generated at the cathode. The consequence is that there are fewer or smaller gas bubbles so they have a lesser overall effect on the surface quality. Any additional factors that would explain the slightly different results of the anionic solution compared to the cationic are much less obvious and would likely require thorough investigation.

4.2.5 Bundle alignment

With the deposition rate being unexpectedly high and the optimal voltage range being lower than the cationic solution, the first EPD attempt with the anionic solution was deposited at a relatively high voltage. The resulting behavior of the material as it was being deposited was unexpected. It was observed that the material was forming tendrils on the substrate that pointed parallel to the electric field and reached out from the anode towards the cathode. The longest of these tendrils were at the bottom edge of the substrate and they spanned the majority of the distance, almost reaching the opposite electrode. When the applied voltage was removed, the nanotubes sagged downward due to gravity, suggesting that the electric field was responsible for keeping them pointed parallel. Most of the tendrils were broken off when the substrate was removed from the solution, likely

due to surface tension and because they were only weakly bonded together. Any remaining tendrils were nearly flattened as the substrate was removed except for a dense protrusion of material along the substrate edge, and a few bumps remained on the rest of the surface. The post-deposit solution was visibly degraded with the fallen tendril material remaining as a solid even after attempts to re-dissolve the material using an ultrasonic bath. Three stages of this observation have been captured and displayed in Figure 34 showing the tendrils mid-deposition, the removed wet substrate, and the resulting dry coating.

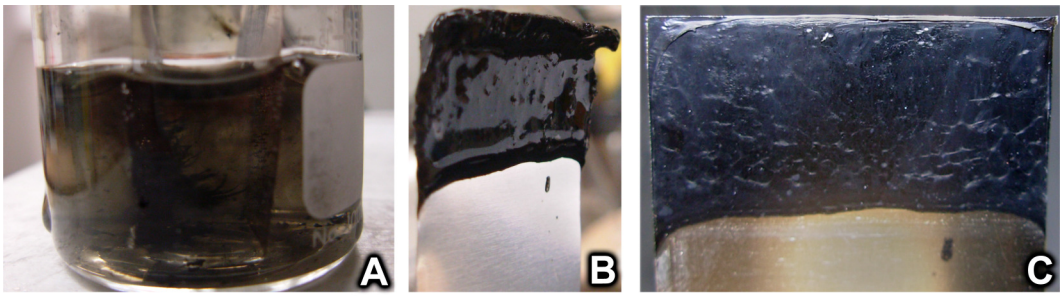

Figure 34 - Alignment of functionalized nanotube material during anodic EPD at 15V for 4 minutes. (specimen T7SS-1) A) Beaker of solution during the deposition showing the anode substrate on the left with tendrils of material pointing towards the cathode on the right, oriented parallel to the electric field during deposition. The deposited material is the dark part in the center of the image and on the substrate surface. B) The resulting wet coating, and C) the resulting coating after drying. Coated substrates are oriented upside-down from their position during the EPD process.

The mechanics behind this observation might involve the electronic polarization of the nanotubes, resulting in their subsequent orienting parallel to the electric field, and the electrostatic attraction of aligned nanotubes due to the induced polarization as suggested in 2004 by P. Kamat et. al.[90] In the Kamat EPD study using carbon nanotubes mixed in a THF solution with tetraoctylammonium bromide, the investigators observed the formation of nanotube tendrils aligned to the electric field at high applied voltage with a description and images that closely match the observations presented here. They suggested that the electric field aligns and polarizes the SWNTs such that the end pointing towards the

cathode is more positive and the end pointing towards the anode is more negative. It was also noted that the tendrils would grow towards the opposite electrode until the field was turned off and then they would relax their orientation and sag downward. In addition, they also performed a cyclic voltammogram that suggested nanotubes have the ability to undergo charging when subjected to an externally applied electric field, and theoretical calculations predict increased charge density at the ends of charged nanotubes.

This observed field induced tendril growth and alignment does not produce a structure that is ideal for the purposes of creating smooth coatings, but being aware of the phenomenon is useful for the overall understanding of the deposition mechanics. It is possible that there may be potential niche applications where this phenomenon could be exploited to provide unique structural and electronic properties and it is known that the alignment of carbon nanotubes is being actively researched in the scientific community for this reason.

4.2.6 Solution depletion and coating repeatability

Using the ethanol-based solution composed from 67% of the original functionalized nanotube solution concentration, the applied voltage of the 5th deposition experiment in this set was 20 V. These conditions were then repeated 5 additional times to become familiar with the amount of coatings that can be created before the quality noticeably declines. It was observed that the coatings became increasingly thinner (decrease of opacity), visibly rougher, and the deposited material was increasingly runnier as the substrate was removed from the solution and set to dry.

The decrease in thickness can be attributed to the decrease in concentration as material is removed from solution and deposited on each substrate. The increase in roughness suggests that the homogeneity of the solution declines after prolonged

exposure to the electric field. Perhaps the functionalized nanotubes in solution agglomerate due to the polarizing effects of the electric field that was likely responsible for the noted alignment phenomenon. Polarized nanotubes would then be attracted to each other due to the difference in charge along each end as well as the fact that the polymer side chains are also charged. If nanotube bundles and agglomerates are forming then when these particles are deposited they may retain their shape which could certainly create a coating with a higher roughness compared to one created from a well dispersed solution of smaller particles.

The increasingly runny deposited material upon substrate removal from solution might be a symptom of a decline in coating quality. Perhaps there is a decrease in the adhesion of the material to the substrate, and also the cohesion of the deposited material. If the previously speculated agglomeration of material from solution is occurring before deposition, this may also explain a decrease in adhesion and cohesion. If larger particles are forming then each particle would have a higher ratio of volume to the surface area that is in contact with the substrate, and this could explain a decrease in substrate adhesion. Additionally, the larger the particles are the less interaction and entanglement surface area there is within the material of the coating and this could explain the decrease in cohesion of the deposited material.

4.2.7 Reduction of the ITO substrate surface to a metal

Sometimes in science an unusual observation arises from an accident. In an experiment that was intended to be anionic deposition on an ITO substrate with a platinum cathode, the wiring was accidentally reversed such that the ITO was the cathode and the platinum electrode became the anodic substrate. In cathodic deposition, the anode is typically an inert material such as platinum to prevent it from oxidizing, but in anodic

deposition the substrate is the anode so problems may arise if it is a metal that oxidizes easily. ITO is not at all problematic as the anode because it is already an oxide.

In this accidental setup, the deposition of negatively charged functionalized nanotubes occurred on the platinum electrode which was in the anode position, while the cathode was the ITO. Realizing what error had occurred after observing that the material had deposited on the platinum electrode, it was expected that the ITO surface would remain bare. However, the ITO surface had become opaque and shiny grey colored, almost silvery. The experiment was repeated and the same result was observed. After ruling out the possibility of metal ion contaminants or metal oxide particle contaminants in solution or on the electrodes, the most probable culprit was the ITO substrate surface itself.

It is likely that the In_2O_3 participated in reduction half-cell reactions in addition to the expected reduction of water to hydrogen gas and hydroxide that typically occurs at the cathode, $2H_2O + 2e^- \rightarrow H_2(g) + 2OH^-$, which has a standard reduction potential of -0.83 V.[110] The reduction of indium oxide can occur in a variety of ways so the exact reaction mechanism is not clear. The indium in ITO exists in the +3 oxidation state which is the most common state, but indium is also known to exist in +2 and +1 in some situations as well as the neutral metal. Common aqueous electrochemical reduction reactions for a metal oxide involve the consumption of H^+ or the production of OH^-, and in an alcohol solution there are likely other species involved such as ethoxide:

$$In_2O_3(s) + 6e^- + 6H^+ \rightarrow 2In(s) + 3H_2O \quad \text{(EQ19)}$$

$$In_2O_3(s) + 6e^- + 3H_2O \rightarrow 2In(s) + 6OH^- \quad \text{(EQ20)}$$

$$In_2O_3(s) + 6e^- + 6C_2H_5OH \rightarrow 2In(s) + 6C_2H_5O^- + 3H_2O \quad \text{(EQ21)}$$

Each of these reactions can be expanded into intermediate reactions involving 2InO and In_2O if the oxidation state of indium steps downward incrementally rather than from +3 directly to 0. The reaction of ITO with H^+ is not likely to occur because hydroxide and probably some ethoxide are produced at the cathode by electrolysis half-cell reactions and they would likely combine with the H^+ that is generated at the opposite electrode before it can reach the ITO substrate. The most likely ITO reduction reactions involve the consumption of water or ethanol to produce hydroxide or ethoxide respectively as well as metallic indium. The water-consuming reaction has a standard reduction potential of -1.03 V which is below that of the electrolysis reaction and therefore should not occur preferentially.[110] Despite this, a silvery looking film developed on the ITO cathode during anodic deposition so perhaps there are more energetically favorable mechanisms for the reduction of ITO that have occurred.

The real reduction mechanism of In_2O_3 is probably much more gradual than the sudden change in oxidation states from +3 to 0 with the likely presence of intermediate indium oxidation states. The lower order indium reduction reactions could have more energetically favorable reduction potentials compared to the half-cell reaction for the hydrolysis of water. However, it is overly simplistic to treat the reduction mechanism as if In_2O_3 is a distinct molecule because it is a crystalline solid and reactions would be additionally complicated by surface effects and diffusion. The mechanisms describing the liberation of oxygen from the ITO layer as well as electron transfer to indium atoms probably occur in steps of small surface reactions. The process might be similar to the bond breaking sequence in the etching of ITO by HCl as described by Monk and Man [111], except instead of the indium atoms bonding with chloride ions as in the case of HCl etching, there is electron transfer from the cathode to the indium atoms.

This ITO cathodic reduction phenomenon may have negative consequences for the cathodic deposition of material on ITO surfaces where the transparency and electrical properties of ITO are essential. The existence of a metal surface layer certainly reduces the transparency to a varying degree depending on the extent of reduction. Perhaps more important are the consequences to the electronic properties such as a change in the work function and resistivity of the former ITO layer. It is known that the partial reduction of ITO causes a decrease in electronic conductivity and the effect is said to be the result of the change in ratio of dopant tin atoms to the indium (III) host, which is why partially reduced ITO has been described as "deactivated ITO".[111]

While no specific investigation occurred, there was no visible evidence suggesting that the indium metal layer forms when ITO is used as a substrate for coatings rather than just an exposed counter electrode. Perhaps there may be some minor reduction effects on the surface in the initial stages of deposition, but it is quite possible that the deposited material prevents the reduction reaction from continuing by shielding the oxide from the ions in the solution. This ITO reduction phenomenon may be important to study much more rigorously in performance or optimization studies of devices fabricated by cathodic EPD on ITO substrates. If it is found that there is a decrease in device performance due to the existence of metallic indium at the surface, it may be preferable to utilize anodic deposition techniques instead when using ITO substrates.

4.2.8 Section summary

A solution containing an anionic version of polymer functionalized carbon nanotubes was obtained and anionic electrophoretic deposition was tested. The voltage range required to obtain the best deposits was slightly lower than that of the cationic solution under equivalent conditions and the deposition rate of the anionic solution was

considerably higher. The anionic EPD coatings appear to be slightly better quality than the cationic coating and this may be a result of the lower amount of oxygen gas being generated at the anode compared to the amount of hydrogen that is generated at the cathode via electrolysis reactions.

It was observed that the coating quality declines after repeated deposits showing an increase in the macro scale roughness and an increase in the runniness of the wet deposited material. The suggested explanations for these observations involved both the gradual depletion and agglomeration of the material in solution.

Additionally, two unusual phenomena were observed during the anodic deposition experiments; aligned tendril growth and ITO reduction. During high voltage EPD it was found that tendril growth and alignment of nanotube-containing deposit material was induced during deposition and this was likely caused by electronic polarization of the nanotubes. It was also observed in an anodic EPD experiment that reduction reactions likely occurred in an ITO cathode when it was accidentally used as a counter electrode, which suggests that cathodic deposition on ITO may need to be approached with caution if the reduction effect occurs and is significant enough to affect the essential ITO properties.

4.3 Strong Polyelectrolyte Deposition

4.3.1 Introduction

The coatings that were obtained from the strong polyelectrolyte solutions of functionalized carbon nanotubes were of insufficient quality for practical applications. Further deposition with this polymer was performed without adding carbon nanotubes in order to simplify the experiment by removing a variable. The pure polymer was expected

to be easier to deposit due to a higher charge density and the smaller particle size might translate to improvements in coating cohesion from a larger ratio of surface area to volume. The electrophoretic deposition of strong polyelectrolyte conjugated polymer was continued with both the cathodic and anodic varieties which were synthesized and supplied by the Adronov group.

4.3.2 Description of anionic polymer experiments

Anodic deposition of the negatively charged polymer was performed using the as-received concentration which was 0.5 $g \cdot L^{-1}$ and also a 0.15 $g \cdot L^{-1}$ concentration diluted to contain 70% ethanol. The deposition of the fully concentrated anionic polymer coating produced a large number of oxygen gas bubbles at the stainless steel anode substrate. The coating was an orange-brown base color covered with multicolored patches and it was heavily marked by hundreds of small circles. It was important to make sure the appearance of the coating was due to the deposition and not oxidation of the substrate, so the experiment was repeated with a different substrate.

The ITO substrate can not suffer from oxidation at the anode because it is already an oxide. The resulting coating on ITO was faint due to the substrate's transparency, but close inspection revealed the same high density of small circle marks and multicolored patches similar to the stainless steel. This suggests the stainless steel remained intact and the appearance of the coated substrate is solely due to the coating rather than oxidation. Figure 35 shows the stainless steel coating and the ITO coating with a digitally enhanced image insert that emphasizes the colors and small circle marks of a section of the ITO coating.

The rate of gas produced at the electrodes was very high, even at relatively low voltages such as 10 V, and this is probably the cause of hundreds of circular marks on the

coating. While this result as well as the many colors of the coatings appear to be different from the results of the deposition of nanotubes that are functionalized with this polymer, it is important to realize that nanotube coatings are very dark. Since carbon nanotubes are black and opaque, their removal from the experiment allowed much more visual details to be revealed in the coating because the polymer is translucent and a lighter shade of brown. Various colorful interference effects were slightly observable in the nanotube coatings, but the darkness of the coating mitigates the appearance of the visual effects that are more easily noticeable in a pure polymer coating.

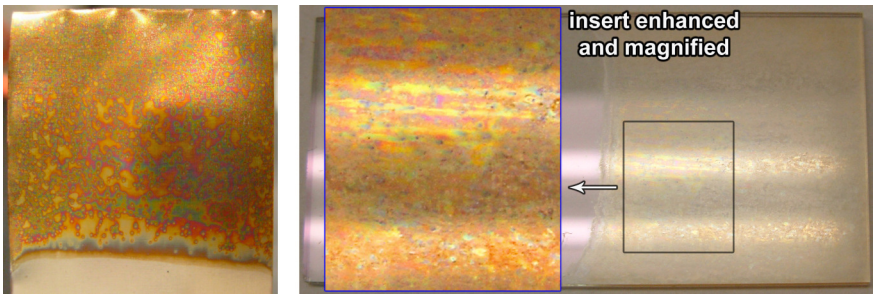

Figure 35 - Photos of full concentration anionic polymer EPD coatings deposited at 20 V for 3 minutes each. [left] On stainless steel, and [right] on ITO, with the boxed portion magnified and digitally enhanced in the inserted image to reveal the colors and small circle marks. The reflection of the fluorescent tube ceiling lights was utilized in the photography of the ITO coating to improve the visibility of the surface features. The specimen codes are P1-1 and P1-2 respectively.

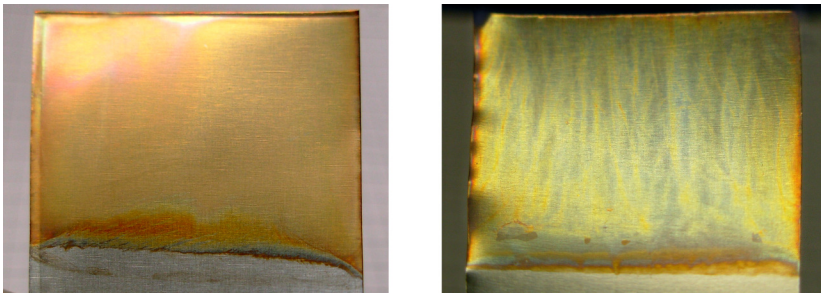

Figure 36 – EPD Coatings of anionic polymer diluted with 70% ethanol to 0.15 g·L^{-1}. [left] A smooth coating deposited at 15 V for 30 min. [right] A vertically streaked coating deposited at 35 V for 10 min. The specimen codes are P3-3 and P3-4 respectively.

The gas generation rate needed to be dramatically reduced so a series of experiments with 70% ethanol dilution were conducted. The polymer concentration was reduced to 30% of the original concentration, which became 0.15 $g \cdot L^{-1}$. The deposition of this dilute solution did not produce visible gas bubbles at the electrodes and the circular marks were absent from the resulting coatings. At voltages higher than 20 V there was some bubble formation at the electrodes but the bubbles tended to remain small and rise up rather than settling on the substrate. The bubbles floated to the surface rapidly in columns and this caused vertical streaking to occur in the coatings. At voltages set below 20 V the gas production was low enough that there was not visible bubble formation and the resulting coatings were smooth. All of the ethanol-diluted anionic polyelectrolyte coatings appeared to be very thin, and deposition times that were longer than usual such as 10 minutes or more were necessary to obtain a visible coating. This is not unexpected because the concentration of polymer was quite low at 0.15 $g \cdot L^{-1}$ and the deposition rate scales with concentration. Figure 36 shows a coating deposited below 20 V another deposited above 20 V, clearly demonstrating the different in color consistency.

4.3.3 Description of cationic polymer experiments

The cationic polyelectrolyte solution without nanotubes, synthesized by the Adronov group, was received having the concentration of 0.5 $g \cdot L^{-1}$ and with the warning that this cationic solution is not as stable in ethanol as the anionic solution. The solution was diluted to 50% ethanol containing 0.25 $g \cdot L^{-1}$ polymer and deposition was attempted since the solution remained stable. A series of cathodic deposition experiments lasting 10 minutes each were attempted at applied voltages ranging from 20 V to 40 V. In all of these attempts there was no noticeable deposit on the stainless steel substrate. The deposition time and applied voltage were certainly large enough to produce a deposit if

the solution was capable of forming a coating, so the lack of a deposit was unexpected. Another solution diluted with less ethanol (30%) was subjected to the same EPD experiment and again there was no deposit, with the only noticeable difference being more gas generated at the electrodes due to the increased water content.

In further attempts to deposit this polymer, small amounts of the additive, Zirconyl Chloride, were used because it had been proven in the past to facilitate the deposition of the cationic strong polyelectrolyte, poly(diallyldimethylammonium chloride), PDDA.[112] The result on the cathode substrate was a very thin and patchy white deposit, which is most likely caused by reactions at the electrode with the additive itself to form zirconium oxides and hydroxides, rather then a polymer coating, which would be pale brown in color. Increasing the additive concentration also had a direct correlation to the current density during deposition, suggesting that the additive is the dominant charge carrier. The polymer did react to the additive during deposition with the formation of cloudy precipitates or possibly mild gelling effects in the beaker between the electrodes. However, there appeared to be no noticeable driving force to move the material towards the cathode or to form a deposit on the cathode substrate.

Previously when the cationic polymer was used to functionalize carbon nanotubes, the resulting macromolecules formed coatings on the cathode during EPD, although they were poor quality coatings. The lack of a deposit with the new solution of the cationic polymer is strange because the nanotubes should not be the difference between producing a coating and lacking a deposit since they are not naturally charged and they do not consume, screen, or otherwise interact with the charge of the functional groups at the ends of the side chains. The results with this polymer solution put into question the extent of supposed positive charge of the polymer material in solution and perhaps there was a

mistake in the synthesis procedure where the polymer was not sufficiently charged with the quaternary ammonium cations that should be at the ends of the side chains.

4.3.4 Strong polyelectrolyte discussion

Both charge varieties of polymer solutions were expected to have a higher deposition rate than the polymer functionalized nanotubes because the polymer would have a higher charge density than the macromolecules formed by the combination with neutrally charged nanotubes. However, an increased deposition rate was not observed and instead the rate was lower. There may be a simple explanation for this, and it has to do with differences in concentration.

The concentrations of the received anionic and cationic polymer were known to be 0.5 $g \cdot L^{-1}$ before they were diluted with ethanol. On the other hand, the concentration of polymer material in the functionalized nanotube solution for the preliminary EPD tests was unknown. This is a symptom of the preparation method used by the Adronov group which was to saturate the solution with functionalized nanotubes and simply take the maximum concentrated soluble portion of the mixture and to leave behind the excess from the centrifuge. The use of this method meant that the concentrations were not pre-determined and were thus unknown. Despite this unknown, experience with the transparency of these solutions at various concentrations can provide a rough method of comparing their concentrations.

The preliminary functionalized nanotube solutions were very dark and could be estimated to be well over 0.5 $g \cdot L^{-1}$ and more likely in the range of 2 $g \cdot L^{-1}$. This is much more concentrated than the anionic and cationic polymer solutions in this latest set of experiments, which is known to be 0.5 $g \cdot L^{-1}$. The difference in deposition rates between the functionalized nanotube solutions and the polymer solutions is likely to be the result

of the difference in concentrations, since the concentration of material is positively correlated to the deposition rate.

While the coatings from the anionic polymer solution diluted with 70% ethanol were the best quality coatings described so far, they were still not as uniform in appearance as a polymer film should be. While further experimentation with the strong polyelectrolyte solutions could likely have resulted in improvements in the coating quality, the fact remains that strong polyelectrolytes are not ideal for electrophoretic deposition. The substitution of a different functional group at the end of the side chains could convert the polymer into a weak polyelectrolyte, which is much better suited for EPD because the charge can be neutralized by controlling the pH of the solution. There is potential for a better quality coating using a weak polyelectrolyte because if the polymer can be neutralized at the substrate electrode it could become insoluble or at least much less soluble. In addition, there would no longer be inter-chain repulsive forces because the side chain functional groups would no longer carry a charge, facilitating better cohesion between the macromolecules and therefore a better quality coating.

4.3.5 Section summary

EPD experimentation continued using polymer solutions without carbon nanotubes. Initial solutions of anionic polymer produced coatings that were heavily marked from the result of gas generation. The addition of a large proportion of ethanol significantly reduced the gas generation rate and smooth coatings were obtained using a low deposition rate when the applied voltage was below 20 V. EPD attempts with a new solution of cationic polymer were unsuccessful and it was likely that the polymer may have been insufficiently charged during the synthesis procedure.

While further experimentation with the strong polyelectrolyte solutions may have resulted in small improvements in their coating quality, it was decided that the deposition of weak polyelectrolyte polymers should be pursued preferentially because they are more ideal for electrophoretic deposition and have the potential for superior results.

4.4 HCl-protonated Weak Polyelectrolyte Deposition

4.4.1 Introduction

A new polymer solution was received which had been synthesized by the Adronov group to contain a different functional group to become a weak polyelectrolyte. The received solution contained 2 $g \cdot L^{-1}$ of polymer in 70% ethanol and 30% water which contained 0.1M HCl.

The original cationic polymer, P1, was modified to contain one less ethyl group bonded to the nitrogen atom at the end of each side chain. This changed the quaternary ammonium cations into neutrally charged tertiary amines. The resulting polymer, shown structurally in Figure 37 is called poly(9,9-bis(diethylaminopropyl)-2,7-fluoreneco-1,4-phenylene) and was assigned the shorthand name PDAFP. The nitrogen of each end group becomes positively charged when protonated by acid, which enables the electrophoresis of the polymer towards the cathode during EPD. The positively charged PDAFP can be easily reverted back to the neutral PDAFP in high pH environments. If a high pH environment is formed locally in a globally acidic solution, the polymer can be neutralized within the local alkaline region even while the remaining polymer in the net acidic bulk holds its positive charge.

Another important aspect of the neutral versus charged PDAFP is the change in solubility. The neutral polymer is not at all soluble in water but once it has been

protonated with acid it becomes highly soluble. The interaction with ethanol is not as binary as it is with water since the neutral PDAFP is moderately soluble in ethanol, but the protonated PDAFP is still much more ethanol-soluble.

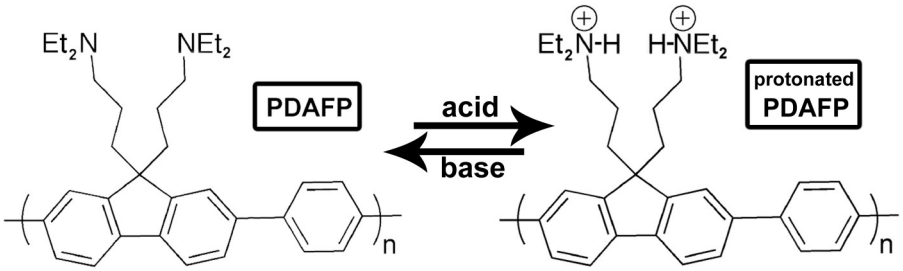

Figure 37 - The structure of the weak polyelectrolyte synthesized by the Adronov group, poly(9,9-bis(diethylaminopropyl)-2,7-fluoreneco-1,4-phenylene), or PDAFP. This polymer becomes protonated in acidic solutions to become positively charged.

4.4.2 Experimentation with a polymer solution

Initial EPD experimentation with the weak polyelectrolyte solution focused on depositing films without carbon nanotubes being added to the solution. The polymer was deposited from concentrations of 0.5 $g \cdot L^{-1}$ and 1.0 $g \cdot L^{-1}$, and with ethanol concentrations of 70%, 85%, and 92.5%. The applied voltage was varied between 5 V and 20 V and the experiments were set for times ranging from 2 min to 10 min.

The deposition mechanism for the weak polyelectrolyte utilizes the pH dependent charge properties of the tertiary amine functional groups. Since the solubility is strongly controlled by the presence of charge, it changes dramatically when the cationic polymer is deprotonated. The charged polymer is deprotonated by the OH^- ions to form water molecules and the neutral polymer in the vicinity of the cathode where there is a local high pH region, caused by electrolysis reduction reactions. The neutral polymer is insoluble in water and only weakly soluble in ethanol, but since the concentration of the polymer at the cathode is very high due to electrophoresis; it is likely that the minor solubility in ethanol is insignificant and the polymer at the cathode surface is effectively

insoluble. The absence of charge in the polymer enables it to coagulate without any electrostatic repulsion and thus solidify into a coating on the substrate.

The resulting coatings were homogenous in color but they were marked by some vertical streaking and spots, both likely caused by the production and rise of gas bubbles. Since there was rapid gas bubble formation at the electrodes, especially the cathode substrate, the rate of gas production looked to be considerably higher than during the deposition experiments of the strong polyelectrolyte. In all cases with the HCl-protonated weak polyelectrolyte solution, the measured current density was much higher than in the deposition experiments with the strong polyelectrolyte by a factor of approximately 10. The high current density suggests that the ionic content of the solution is too high and considering the rapid formation of bubbles it is likely that the acid concentration was excessive. In order to test this hypothesis, an experiment was developed to observe the results of varying the acid concentration.

Since the polymer was known to have mild solubility in ethanol in its neutral state, an 18 mL ethanol solution of PDAFP was prepared by the Adronov group without any acid and the polymer was dissolved to saturation. The concentration was thus unknown but based on the color and transparency it was estimated to be less then 0.5 $g \cdot L^{-1}$. Three solutions of 90% ethanol were prepared from the neutral polymer solution containing HCl concentrations of 0.01M, 0.001M and 0.0001M. Each solution contained 6 mL from the original and since they were planned to be 24 mL, the polymer concentration of each test solution was one quarter of the originally received solution, which according to the estimate would be 0.125 $g \cdot L^{-1}$ or less.

The result was that none of the tests produced a significant coating including the highest acid concentration test which was designed to contain more acid than the previous

experiments with the protonated weak polyelectrolyte. Gas bubbles were generated in the highest acid concentration test but gas production was not visible in the other two tests. The concentration of polymer was likely far too low to obtain a coating, even at high voltages, tested up to 60 V.

A few more tests were performed with new solutions that were prepared to be slightly acidic in order to be able to vary the acid concentration, but once again the saturated polymer concentration was low. While some slight coatings were obtained on the substrates, the quality was low with the coatings being very thin and possessing distinct vertical streaks. Based on all these experiments with various concentrations of polymer, acid, and ethanol, a specific mixture was requested to the Adronov group to prepare. The mixture contained 90% ethanol and within the 10% water was an acid concentration of 0.1M HCl, to protonate a high concentration of the weak polyelectrolyte, hopefully without having too much excess acid. The resulting solution was prepared with 2.0 $g \cdot L^{-1}$ of polymer and it was very stable.

Two sets of EPD experiments were performed with this polymer using the solution as received, and a diluted version containing 1.0 $g \cdot L^{-1}$ of polymer and 95% ethanol. The EPD coatings produced from this solution were very uniform in color and moderately smooth in texture aside from mild vertical streaks caused by some gas bubble formation, but to a significantly lesser extent than in previous weak polyelectrolyte experiments.

As had been previously observed with the strong polyelectrolyte, the voltage range required to achieve the best quality deposit is higher when the concentration of the depositing material in solution is lower. The current density of this new solution during deposition was only approximately three times the current density of the strong polyelectrolyte solutions, which is a much smaller increase compared to the previously

observed 10 fold increase in the case of the earlier experiments which contained excessive acid concentrations.

The effects of additional acid was also tested and it increased the current density, the production rate of gas bubbles, and caused more distinct vertical streaks in the coating with no perceived benefit to the deposition experiment.

4.4.3 Experimentation with a polymer solution containing functionalized SWNTs

It is likely that slightly better results could be obtained by additional fine tuning of the deposition variables such as the polymer concentration, acid concentration, ethanol:water ratio, applied voltage, and time. However, since the ultimate purpose is to produce polymer coatings containing functionalized carbon nanotubes, fine adjustments are better suited to experimentation with a solution containing nanotubes since the optimized variables are likely not identical to those for the pure polymer solution.

Deposition experiments were conducted using a new solution of weak polyelectrolyte functionalized SWNTs and excess free polymer, which was received as 2.0 $g \cdot L^{-1}$ of total polymer and 0.1 $g \cdot L^{-1}$ of SWNT, or 5% of the polymer weight. The solvent was 90% Ethanol and the 10% amount of water contained 0.1M HCl. All experiments preserved the same 20:1 ratio of polymer to SWNT and the following polymer concentrations were utilized in the different sets of experiments: 1.3 $g \cdot L^{-1}$, 1.0 $g \cdot L^{-1}$, 0.6 $g \cdot L^{-1}$, and 0.5 $g \cdot L^{-1}$. The applied voltage and the time of deposition were varied to find ideal conditions at each voltage and they ranged from 5 V to 40 V and from 1 min to 6 min respectively. Ethanol concentrations of the experiment sets varied only slightly from as low as 93% to as high as 97.5%.

4.4.4 Nanotube coating results

The resulting coatings were near homogenous in their yellowish grey color which was similar to the coatings without nanotubes but their presence adds a grey shade to the yellowish brown of the polymer coatings. These nanotube-containing coatings also exhibited the same subtle vertical streaking texture as the polymer coatings.

There was an observable difference between the qualities of two coatings deposited under similar conditions where the coating that was produced after a number of coatings had already been deposited was visibly smoother. Typically if the applied voltage is set above the range to obtain an ideal coating, the quality suffers from the effects of excessive gas bubble formation. However it was observed in these test series that after enough coatings had been produced with the same solution, the range of ideal voltage shifted upward.

One example of the phenomenon occurred in an experiment series which tested the effect of increasing the applied voltage starting from 8 V and increasing by 4 volts for each coating. The coating deposited at 24 V contained bubble marks from electrode gas production and this effect continued for the 28 V and 32 V coatings. The next two coatings were deposited at 36 V and 40 V and they were observed to be considerably smoother than the three previous coatings and free of bubble markings. Next was a 44 V coating which again contained bubble marks that suggests there is still an upper limit on the upward shift in ideal voltage. Finally another 32 V coating was deposited and it was significantly smoother than the previous 32 V coating, although also appearing to be thinner. Meanwhile the solution was increasingly becoming more transparent and the color was fading after each deposit.

The experiments with using lower material concentrations also exhibited improved coating quality compared to those deposited from high concentration solutions. In this case the water concentration was also lower and the increased smoothness can be partially attributed to the resulting lower rate of gas generation at the electrodes. However in the experiments where the variables are fixed except for the reduction in the amount of material remaining in solution, the decrease in material concentration is likely responsible for the observed improvement in coating smoothness. According to Hamaker's Law, the deposition yield is proportional to the concentration of depositing material.[113] So perhaps when the deposition rate is high due to high concentration, there is not enough time for the deposited material to assemble in a densely packed and smooth film.[73] There might also be some liquid and gas molecules that get trapped by the rapidly depositing material.

A second possible factor in the observed improvement of coatings deposited towards the end of the experiment series is that the amount of water in the beaker may decreases over time at a faster rate than the ethanol. Since the electrolysis of water to hydrogen and oxygen gas occurs more readily than electrode reactions with ethanol, it is possible that after a given amount of deposition time much of the water has been consumed to produce gas molecules which escaped the beaker, increasing the ethanol to water ratio.

Lastly, the lower concentration of material in solution also has an effect on the amount of dipole-dipole interactions between the macromolecules. Since the polymeric material in solution is positively charged and the applied electric field induces dipoles in the electron structure, electrostatic interactions between macromolecules in solution will occur. This activity likely leads to some agglomeration of the material due to electrostatic attraction before it has traveled to the substrate. When the concentration is lower the probability of macromolecular interactions is lower and thus the degree of agglomeration

would also be lower. The reduction in electro-induced agglomeration could likely be responsible for the smoother coatings because with a smaller particle size the material would be able to pack more efficiently compared to the arrangement of large bulky particles.

Another coating quality observation was the difference between two coatings deposited with the same applied voltage but coated for different durations. It was observed that the coating surface quality appears to decrease as the coating is deposited longer. In one of the experiment series an applied voltage of 6 V was utilized to deposit a coating for 2 minutes, then another coating for 6 minutes, and then an additional 2 minute coating. The coatings deposited for 2 minutes looked identical and appeared to be smooth and monochromatic, while the coating deposited for 6 minutes was streaky.

Perhaps the macro scale roughness of the coating increases as it gets thicker. This phenomenon could be explained by the possible amplification of the peaks in the coating thickness. It is known that electrostatic charges on a conductor tend to gather at locations with a small radius of curvature such as at a peak in a coating. Since the increased charge density at the peaks increases the local electric field this would also increase the deposition rate and thus amplify the roughness.

This proposed peak amplification effect has limitations because of conductivity differences between the substrate and the coating. The polymer, although conjugated and containing some carbon nanotubes, is still much less conductive than the substrate. The resistance from the substrate to the top of the peaks in the coating thickness causes a voltage drop which decreases the local electric field at the coating surface. The parts of the coating with the least resistance are the thin areas so the local electric field strength would be increased. Therefore the effect of coating resistance somewhat counteracts the

amplification of peaks. If these proposed mechanics actually take place, the roughness would strongly depend on the resistance of the coating material, with high resistance materials producing smoother coatings due to the decreased deposition rate at the thick points.

4.4.5 Microstructure of deposited material

The coatings of weak polyelectrolyte functionalized carbon nanotubes and free polymer deposited from a low concentration and high ethanol solution generally appeared to be good quality, at least in the macro scale. There did not appear to be much more room for improvement in the better quality coatings that were produced, but the microstructure was unknown and could be a source of important information.

Scanning electron microscopy (SEM) and atomic force microscopy (AFM) were utilized to observe these coatings at the micro and sub micron scale. The observed structure of the material in the coating is an entanglement of somewhat fibrous polymer agglomeration containing many small pores that appear to be the result of empty space in the entanglement of polymeric material. The pores range from 15 nm to 65 nm in diameter and the average pore is approximately 30 nm. These small pores do not appear to penetrate deeply and it is unlikely that they provide an open channel to the substrate except for the case of a very thin film that approaches the thickness of only a few layers of the polymer fibers. One of the coatings was prepared as a cross section specimen which enabled the measurement of the coating thickness to be approximately 1.8 μm. The cross section and high magnification surface images are displayed as Figure 38.

The most surprising observation from SEM imaging occurred in the mid-magnification range where an unexpected structural phenomenon was found. A high density of crater-like, open-ended, circular voids was found throughout the whole coating

surface. The average size and coverage of these voids varied with each specimen, but the diameters typically ranged between 3 μm and 19 μm across all of the observed coatings.

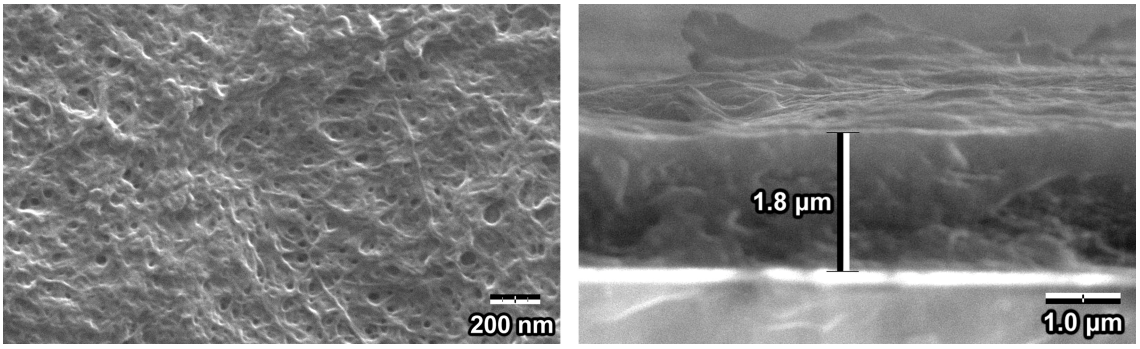

Figure 38 - SEM micrographs. [left] Typical coating surface at high magnification showing sub-micron structure acquired at 15 kV, 50000x, and 9.0 mm working distance. [right] Cross section of coating deposited on a platinized silicon wafer, acquired at 15 kV, 10000x, and 9.7 mm working distance.

Atomic force microscopy (AFM) was also performed on a similar EPD coating to obtain another perspective from a different characterization technique to ensure that the observed features were not artifacts of the SEM process such as beam damage. The AFM specimen was a coating deposited at 15 V for 2 min on a silicon wafer from a 48 mL solution of 0.5 $g \cdot L^{-1}$ conjugated polymer with 5% weight SWNT and 97.5% ethanol solvent. AFM images were acquired in contact mode using the "J-scanner" which has a maximum scan area of a 150 μm × 150 μm square. The AFM results displayed in Figure 39 show scans of a typical coating region and a void at high magnification. The data shows the average void diameter in this coating is 6.8 μm and the depth is typically is in the range of 1000 nm with gradually sloped walls and a small, flat base. The coating morphology from the AFM data is consistent with the results from SEM, therefore it is likely that both methods are free of significant imaging artifacts, altering effects of sample preparation techniques, or observational damaging effects such as electron beam damage that sometimes affect the integrity of the characterization method.

The SEM examination of the various coatings produced under different conditions to obtain different thickness has led to the identification of some apparent trends in the shape, size, and frequency of the voids that are found throughout these coatings. The void properties appear to change depending on the thickness of the coating as well as the applied voltage that was utilized in the electrophoretic deposition process.

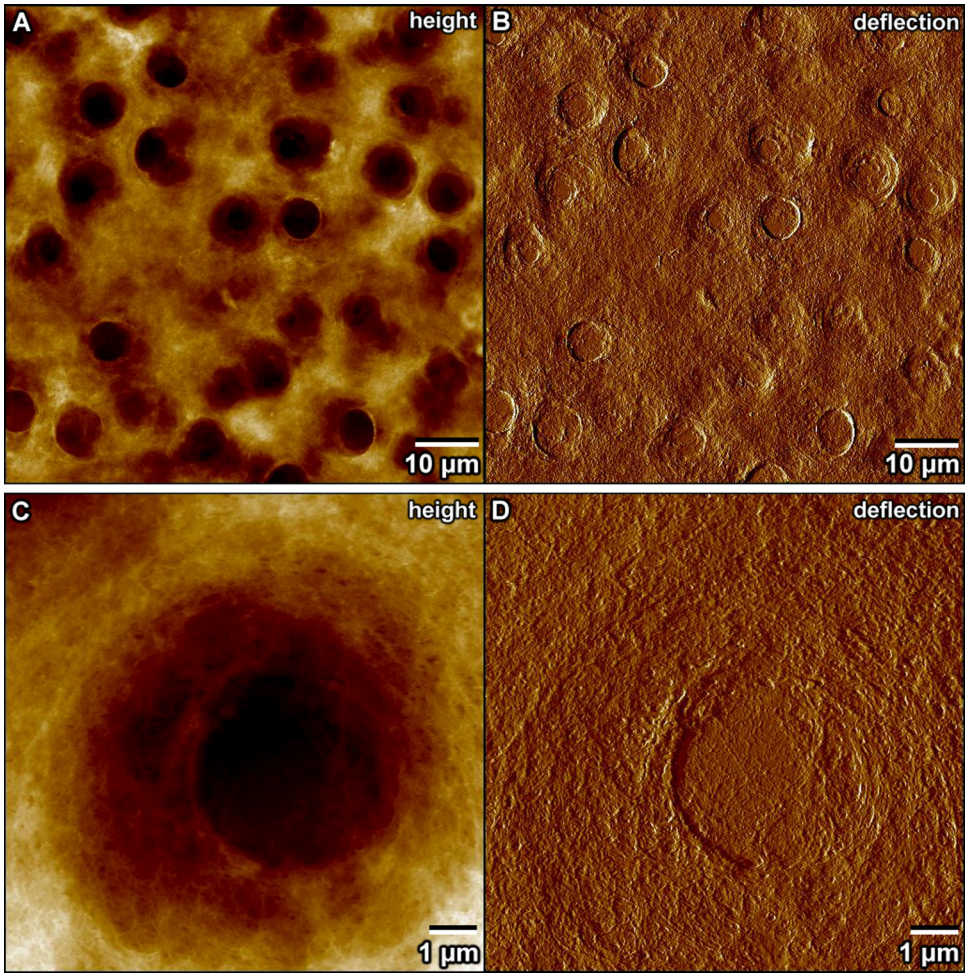

Figure 39 - Two AFM scans of a coating showing height and deflection data using the black-brown-white color scheme and left to right scan direction. The top scan is 75 µm × 75 µm where the black-to-white height scale of image A is 1500 nm. The bottom scan is 10 µm × 10 µm where the black-to-white height scale of image C is 1000 nm. Images B and D are the corresponding deflection data, which gives the rate of height change and it serves the purpose of amplifying small features height variations, and the shadow effect provides a more natural appearance.

Very thin coatings, such as in Figure 40, contain a high density of small voids that are likely to be at their early stage in formation. They are only somewhat circular at that point, and it appears that they tend to merge into larger voids as the coating continues to be deposited. These larger voids become more circular as they grow while the coating thickness increases. Their shape resembles a crater or bowl with a flattened bottom and the walls are sloped as if a sphere was nested inside. As the coating thickness increases further such as in Figure 41, the voids appear to reach a maximum diameter and then the surface opening shrinks inward from the circumference but without filling the void as if the deposited material is encasing a sphere.

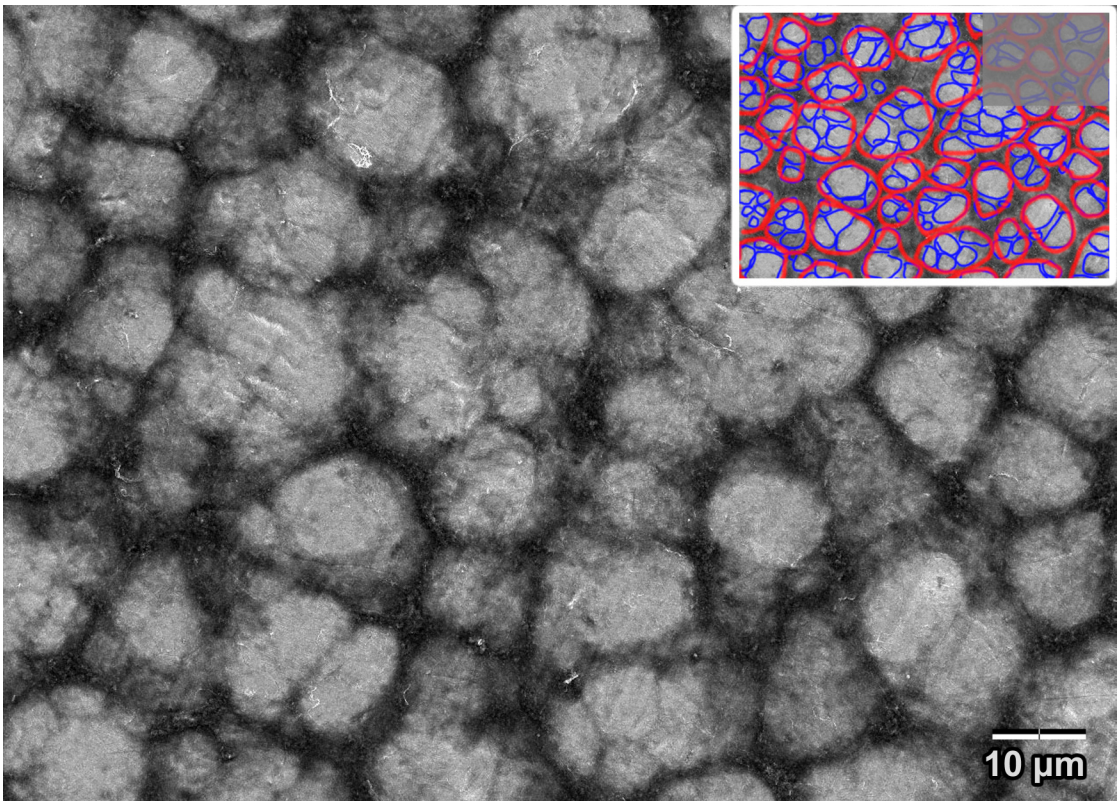

Figure 40 - SEM micrograph of a very thin coating showing a high density of small bare spots that appear to have started merging into larger voids. The insert is a small version of the image where the small voids and post-merge voids are highlighted with blue and red respectively. This coating was deposited at 6 V for 2 min from a 0.5 g·L^{-1} solution with 97.5% ethanol. The image was acquired at 1000x magnification using a 5 keV beam and a 5.5 mm working distance.

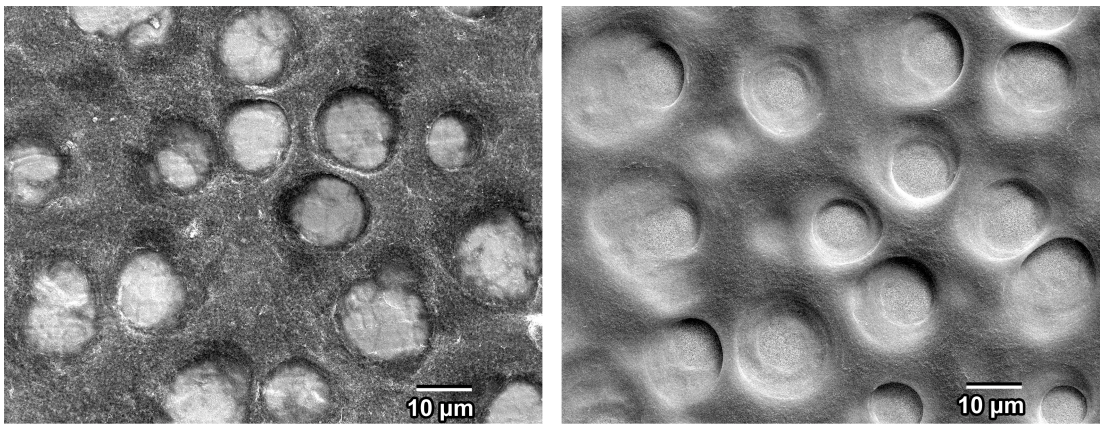

Figure 41 - SEM micrographs showing crater-like voids in the coating. The left image shows voids that still have visible traces of smaller voids in their interior that merged togeather. The right image shows a thicker coating where the voids have become more circular and have reached a large diameter at the top of the coating, likely near the maximum diameter before the coating begins to close over the voids. Both coatings were deposited with a similarly concentrated solution of approximately 0.5 g·L^{-1} and 97.5% ethanol using 6 V for 6 min [left] and 10 V for 10 min [right]. The images were both acquired at 1000x magnification, with a 5 keV beam and 5.5 mm working distance for the left, and with a 15 keV beam and 9 mm working distance for the right.

In very thick coatings such as in Figure 42, there was a range of void sizes with the largest ones resembling wide open craters while others that appeared to originate deeper into the coating had a smaller circular opening at the surface. There were also two features in the SEM micrographs that suggested the possibility of completely enclosed voids, with the first being the decrease in the density of open craters on the surface, which could suggest that many of the original voids have been covered over.

The second feature that suggested there may be enclosed voids under the surface was the bright circles on the coating surface with a smaller diameter than the open craters, shown in Figure 42. These circles posses only a slight shadowing effect from what would be expected with a bowl shaped indentation as depicted in the drawing in Figure 43. Even if the spots might be slightly concaved, the weak shadowing indicates that the curvature and depth is low and likely not significant enough to account for the full brightness of the spots. Perhaps the contributions of type 2 and type 3 secondary electrons account for the observed bright spots. While type 1 secondary electrons are only detected when they

originate from within the first few nanometers of the surface under the electron beam, the presence of backscattered electrons causes additional contributions to the secondary electron image from type 2 and 3 secondary electrons.

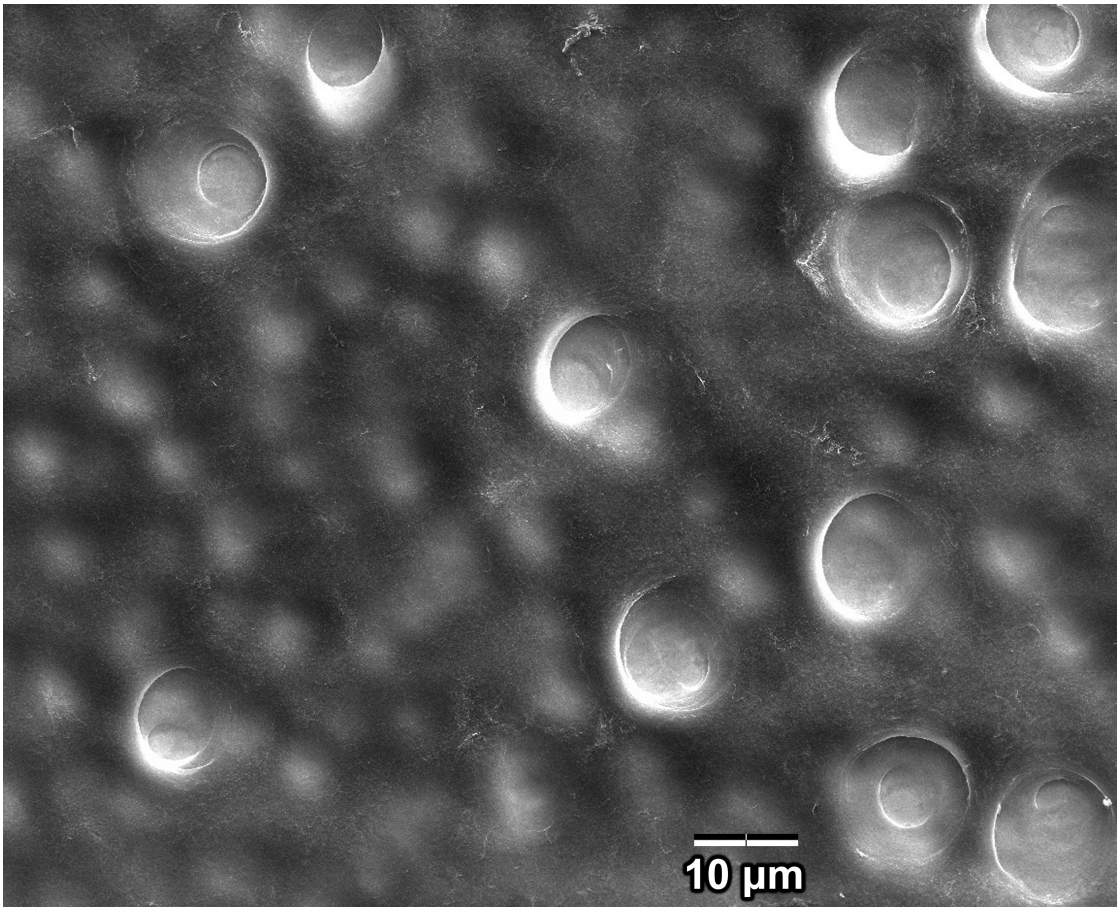

Figure 42 - SEM micrograph of a thick coating showing some voids that appear to be partially closed over at their opening. The image also contains features that suggest there are completely enclosed voids under the surface. These features are the bright circular spots on the surface that are not likely to be simply concave indentations, and the fact that the void density is much smaller than it is with thinner coatings. This coating was deposited at 10 V for 10 min from a solution with 95% ethanol and approximately 1 g·L^{-1} concentration. The image was acquired at 1000x magnification with a 15 keV beam and 8.6 mm working distance.

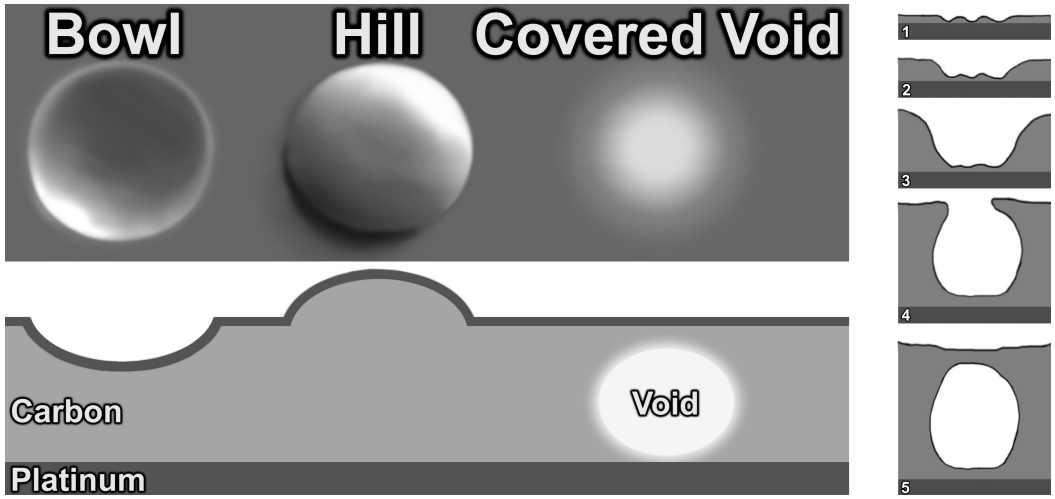

Figure 43 - Schematic diagram showing an illustration of how the secondary electron image (with the detector positioned in the top right) would display a bowl-shaped indentation and a hill-shaped particle to compare to the appearance of the suspected enclosed voids. The top diagram illustrates the surface while the bottom represents the cross section, showing the materials that were used in the Monte Carlo simulation for the coating and the substrate. The right diagram illustrates a cross section of a void at 5 proposed stages in formation as coating thickness increases. 1 is the beginning stage with small shallow voids, 2 is the merging of small voids into a large one, 3 is the maximum diameter of the void, 4 is the partial covering of the void, and 5 is the complete enclosure of the void.

In SEM, the primary electrons from the beam penetrate deeply into the specimen and their interaction volume depends on the acceleration voltage, the density of the specimen, and the atomic number of the elements in the specimen. Backscattered electrons are primary beam electrons that were ejected back out through the surface due to one or more elastic collisions which changed the direction of travel. While these electrons are not collected by the secondary electron detector, when they exit the specimen through the top surface they can cause additional secondary electrons (type 2) to be released and these can contribute towards the secondary electron image. Type 3 secondary electrons can also be produced and collected when the backscattered electrons collide with the various surfaces in the SEM chamber. Through these mechanisms, partial contrast from well below the specimen surface is often observable in the secondary electron image.

The amount of type 2 and 3 secondary electrons that are collected depends on the amount of backscattered electrons, which is a function of the backscattering coefficient. This coefficient is the fraction of primary electrons that escape as backscattered electrons and it increases with atomic number due to a higher amount of elastic scattering events. It can also be modified by factors that change the interaction volume size and shape such as the density or distribution of materials and the acceleration voltage.

The backscattering coefficient of a specific scenario can be approximated by Monte Carlo simulation of the primary electron trajectories of the electron beam as it interacts with the specimen. Two scenarios can be created to determine whether there is an increase in the backscattering coefficient when a large void is present under the surface compared to a solid coating without voids. Using carbon to approximate the deposited composite of polymer and carbon nanotube material, the first scenario is a 200 nm carbon layer covering a 1000 nm empty void layer followed by a 50 nm carbon layer sitting on a platinum substrate. The substrate in the simulation was chosen to be platinum because the coating in Figure 42 was deposited on a 150 nm platinum-coated silicon wafer substrate. The second scenario is a 1250 nm uninterrupted layer of carbon on the platinum substrate.

Monte Carlo simulations were performed using CASINO v2.42 with a 10 nm wide electron beam accelerated to 15 keV. The simulation used 20000 electrons to calculate the backscattering coefficient but only 150 electrons trajectories are displayed in the diagram to maintain visual clarity. The blue paths represent primary electrons that terminated within the specimen and the red paths represent the backscattered primary electrons.

The output of the simulation is displayed in Figure 44 and the calculated backscattering coefficients are 0.051 for the pure carbon layer and 0.49 for the coating with an enclosed 1000 nm void, which is an increase of nearly a factor of 10. This large

increase can be attributed the fact that the primary electrons in the simulation penetrate the specimen deep enough to interact with the high atomic number platinum substrate. Backscattered electrons were generated within the top 100 nm of the platinum substrate and successfully escaped back up through the coating surface because there is very little material to interfere with the electron path.

These results suggest that there is likely to be approximately 10 times as many type 2 and 3 secondary electrons collected when the SEM beam is scanning over an encapsulated void space compared to a solid coating. This would certainly result in an increase in the brightness of the image at the corresponding location due to more electrons contributing to the signal. Therefore, the simulation validates the hypothesis that the bright spots observed in the SEM micrograph of Figure 42 are likely to indicate the presence of voids below the coating surface, as depicted by the illustration in Figure 43.

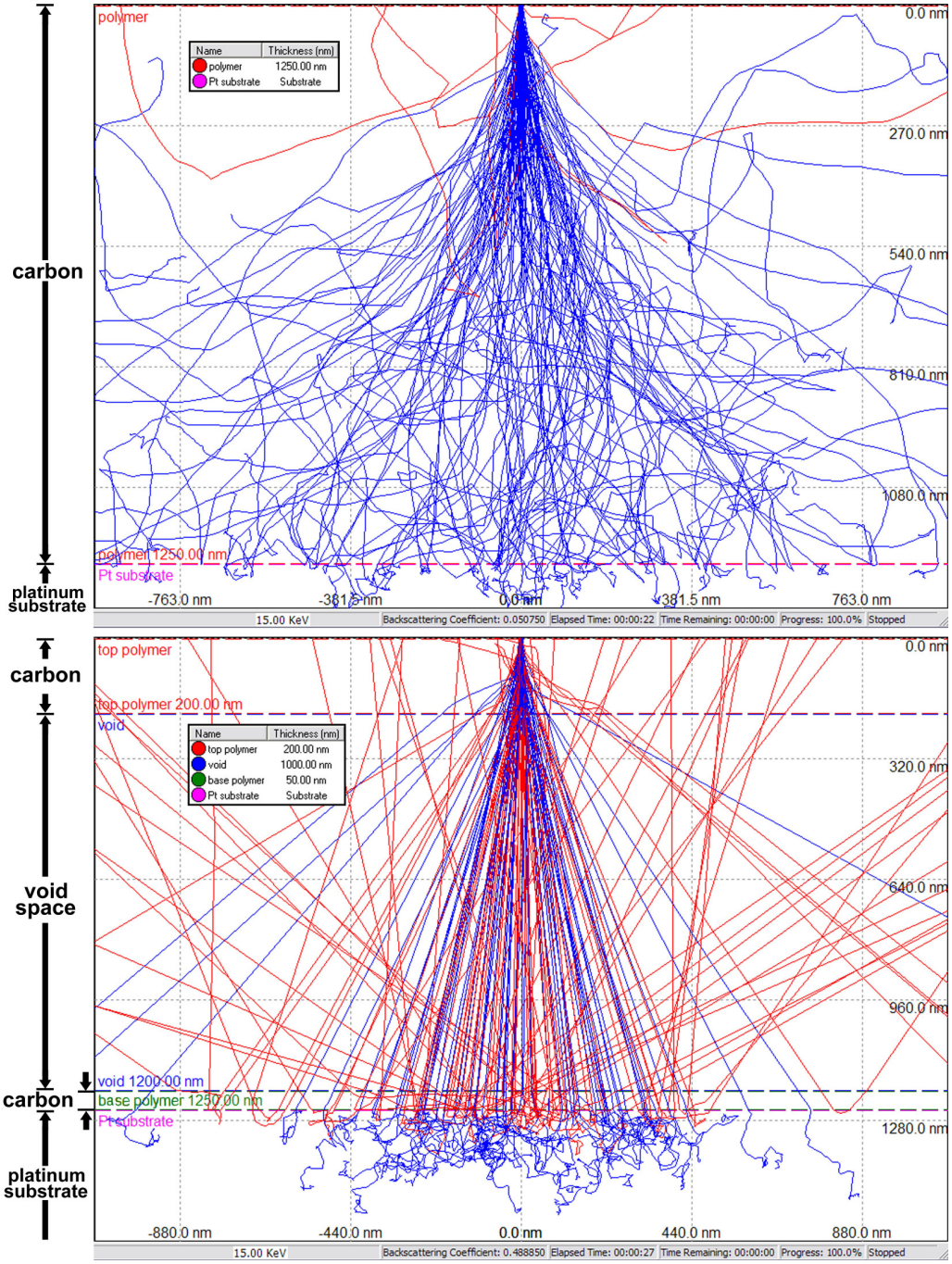

Figure 44 - Monte Carlo simulations using CASINO v2.42 with a 10 nm electron beam at 15 keV. The blue paths represent primary electrons that terminated within the specimen. The red paths represent backscattered electrons. Both diagrams depict a 1250 nm thick carbon coating on a Pt substrate. The top is a solid carbon coating and the bottom contains a 1000 nm void, with 200 nm of carbon above it and 50 nm below. The backscattering coefficients are 0.051 and 0.49 respectively, which suggests that ~10 times more type 2 and 3 secondary electrons are collected when the void is present in the coating.

The applied voltage during deposition was found to have an effect on the size of the voids where higher voltages result in smaller voids in the coating, as shown in the SEM micrographs of Figure 45. This effect appears to be compensated by the increased number of voids at higher voltages so the change in density of voids at the surface is not dramatically different. In one of the experiments, coatings were produced using two different voltages (6 V and 12 V) and two different times for each. In these coatings the shortest duration coatings appeared to be in stage 2 of void development as described in Figure 43 and the average diameter of their voids was smaller than those in the coatings that were deposited for a longer duration which appeared to be in stage 3 of void development. Due to the effect of voltage the thinnest coating contained voids with a larger average diameter than the thickest coating, as shown in Table 1 when comparing specimens WPCNT5-7 and WPCNT5-9. The thicknesses of these coatings were not explicitly measured but they have been ranked from thickest to thinnest. While thicker coatings contained voids with a larger diameter, the applied voltage had a strong effect on the void diameter that dominated over the effect of thickness.

Table 1 - Coatings deposited at two voltages for different times showing the effect of voltage on average void diameter. Coating thickness has been ranked from thickest to thinnest.

specimen	V [V]	t [min]	d_{avg} [μm]	rank
WPCNT5-6	6	6	13	(2) thick
WPCNT5-7	6	2	10	(4) thinnest
WPCNT5-8	12	1	4	(3) thin
WPCNT5-9	12	3	6	(1) thickest

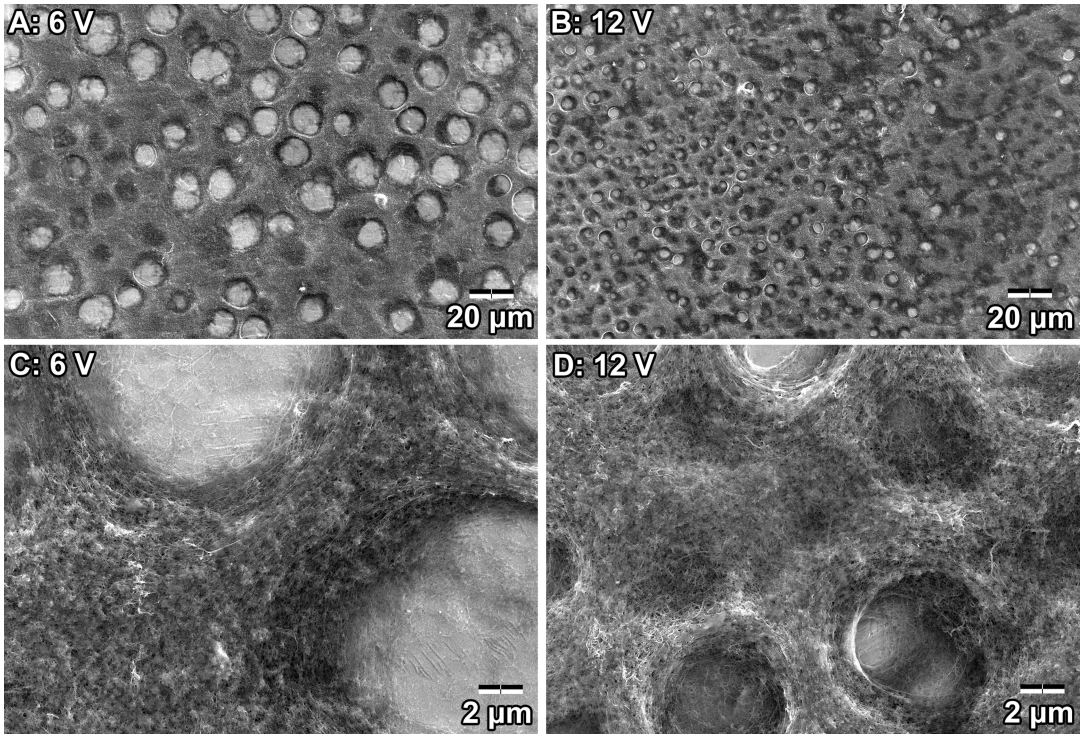

Figure 45 - SEM micrographs of two coatings at two different magnifications, showing the difference in void size and amount due to applied voltage. Images A and C are specimen WPCNT5-6 which was deposited at 6 V for 6 minutes. Images B and D are specimen WPCNT5-9 which was deposited at 12 V for 3 minutes. The image magnifications are 500x for A and B, and 5000x for C and D. All four images were captured using a 5 keV beam and 5.5 mm working distance. The average void diameter for these 6 V and 12 V coatings was 13 µm and 6 µm respectively.

Based on the coating morphology observed by SEM and the fact that gas is generated at the electrodes during deposition, it is extremely likely that the voids in these coatings originated from the formation of gas bubbles. This hypothesis fits well with the suggested description of void growth that was presented in Figure 43, and the following process is proposed to explain the void growth behaviour corresponding to the five steps in the figure:

1) At the beginning of deposition, gas is generated across the whole submerged substrate area and small bubbles begin to form. Due to surface tension these small bubbles remain attached to the substrate. Meanwhile, material is being electrophoretically deposited around the small bubbles but not under them.

2) As the bubbles grow larger many of them make contact with other bubbles and due to the minimization of surface energy they eventually merge to form larger bubbles. More material continues to deposit and thicken the coating on the substrate surrounding the merged bubbles.

3) Both the bubbles and the coating continue to grow as time passes during deposition. The coating builds up on the surface around the bubbles and since at this stage the diameter of a void is likely not much larger than the diameter of a bubble, the voids are also growing and will reach a maximum diameter at the equator of the bubble.

4) Beyond the equator of the bubble, the continually growing coating may begin to enclose it as material builds around the bubble. If the coating is allowed to grow beyond this point the diameter of the void opening will likely shrink with increasing coating thickness.

5) The coating eventually fully encloses some voids and likely traps gas bubbles inside them. The trapped gas probably escapes slowly through the small pores in the deposited material as the coating dries when it is removed from the solution.

It is not necessary that the bubbles remain in their original position for the void space to continue to develop. Eventually the bubbles are released into the solution and rise to the surface. This may occur when a bubble becomes large enough that the buoyancy force begins to dominate over the forces that were holding it in place and this would be very likely to occur when it has grown too large for the deposited material enclosure that surrounds it, and at any time throughout the deposition the bubbles may break away from the surface due to agitation by convection and vibrations. New bubbles may form to again fill the void space with gas preventing the depositing material from filling the interior of the void but allowing the material to slowly enclose it.

This evidence for this process is observable in the SEM images of Figure 40, Figure 41, and Figure 42. It should be noted that there is no reason the bubbles must contact the substrate and they likely also develop on the polymeric coating surface, especially after some voids have become fully enclosed. This would explain the observation that thicker coatings tend to contain surface dimples that do not penetrate deeply into the coating but are still shaped as if a bubble was seated in that place while the coating grew around it.

The suggested gas bubble behaviour can also be applied to propose an explanation for the effects of voltage on the void size. According to Hamaker's Law, the deposition yield is proportional to the charge that has passed through the electrodes so in temporal terms that means the deposition rate is proportional to the current, which is proportional to the applied voltage through Ohm's Law. At higher applied voltages the deposition rate is higher, therefore it likely takes less time for the material to build up a coating that surrounds a bubble and restricts its growth. It is also possible that the increased particulate motion in the solution due to a larger electrophoresis driving force causes additional agitation to the bubbles in the form of convection and enables them to release from the surface at a smaller size. These proposed mechanisms would explain the resulting smaller void size when the applied voltage is higher.

4.4.6 Baking experiments

Coatings are occasionally heated in an oven to optimize the properties and this process, typically called annealing or baking, has been known to reduce the surface roughness in some cases. Baking was tested as a method to possibly reduce the size of the voids and the sub-micron scale porosity of the coatings. A batch of similar coatings was prepared using EPD with the applied voltage set to 10 V for 2 min using a 48 mL solution of 0.5 $g \cdot L^{-1}$ polymer containing 5% weight of SWNTs and diluted to contain 97.5%

ethanol. Each coating was subjected to the same deposition conditions aside from the slight decrease in material concentration after each deposit removed some material from solution. One coating was used as a reference while all the others were subjected to a one hour heat treatment in a pre-heated oven. The temperature for each specimen was different, starting from 50ºC for the first and increasing in intervals of 50ºC for each specimen up to 400ºC for the last coating.

The coatings baked up to 200ºC do not appear to be visually different but the coatings baked in the range of 250ºC to 350ºC were a deeper golden brown color. The 400ºC baked coating was not as vibrant and was more gray-brown in color and looked as if it had become much thinner and more transparent than the other baked coatings. Figure 46 is a series of photographs of the reference coating and all the baked coatings.

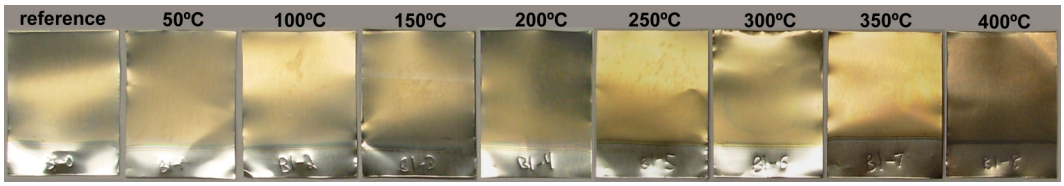

Figure 46 - Photos of the reference coating and the 8 coatings that were baked in a pre-heated oven for one hour with their baking temperatures displayed above their image.

The SEM results of the baked coatings, compiled in Figure 47, show that baking has no effect on the size of the voids but it does affect the coating morphology and thickness. Higher baking temperatures appear to cause degradation in the deposited material and the coating gets increasingly thinner as baking temperature increases because some of the material has burned off. As the coating gets thinner the microstructure of the stainless steel substrate becomes increasingly visible and in the higher temperature baked specimens the grain boundaries and other textures such as scratches aligned in the steel's rolling direction are easily noticeable since there is less material covering the substrate. In the 400ºC specimen and to a lesser extent in the 350ºC specimen, there is very little

remaining material in the voids. The visible remnants are small bundles of carbon nanotubes and many small circular particles with size ranging from 20 nm to 100 nm.

Aside from the voids, in the bulk of the coating there is a gradual decrease in porosity of the baked coatings over the reference coating. The effect is very minor below 350ºC but the deposited material in the 350ºC and 400ºC baked coatings is clearly much less porous than the reference coating because of the elimination or reduction in size of the sub-micron pores. This increase in density likely comes at a cost because it appears that there is also less material remaining on the substrate which implies that some of the material was burned off during the baking process. The polymer appears to heavily decompose starting at 350ºC. Based on these results, a high temperature heat treatment appears to be quite harmful to the coating morphology.

The lower temperature baked coatings, 200ºC and below, were not dramatically different than the reference coating but there appears to be a slight decrease in porosity and coating thickness. It remains unknown whether these minor changes have a noticeable effect on the coating properties but there is one clear benefit of light baking. Due to the high porosity of the coatings there is likely to be traces of solvent remaining and holding the coatings near or above the boiling temperature of water will help to ensure the coatings are completely dry. This is one of the main reasons that coatings for electronic applications typically go through a light baking process.

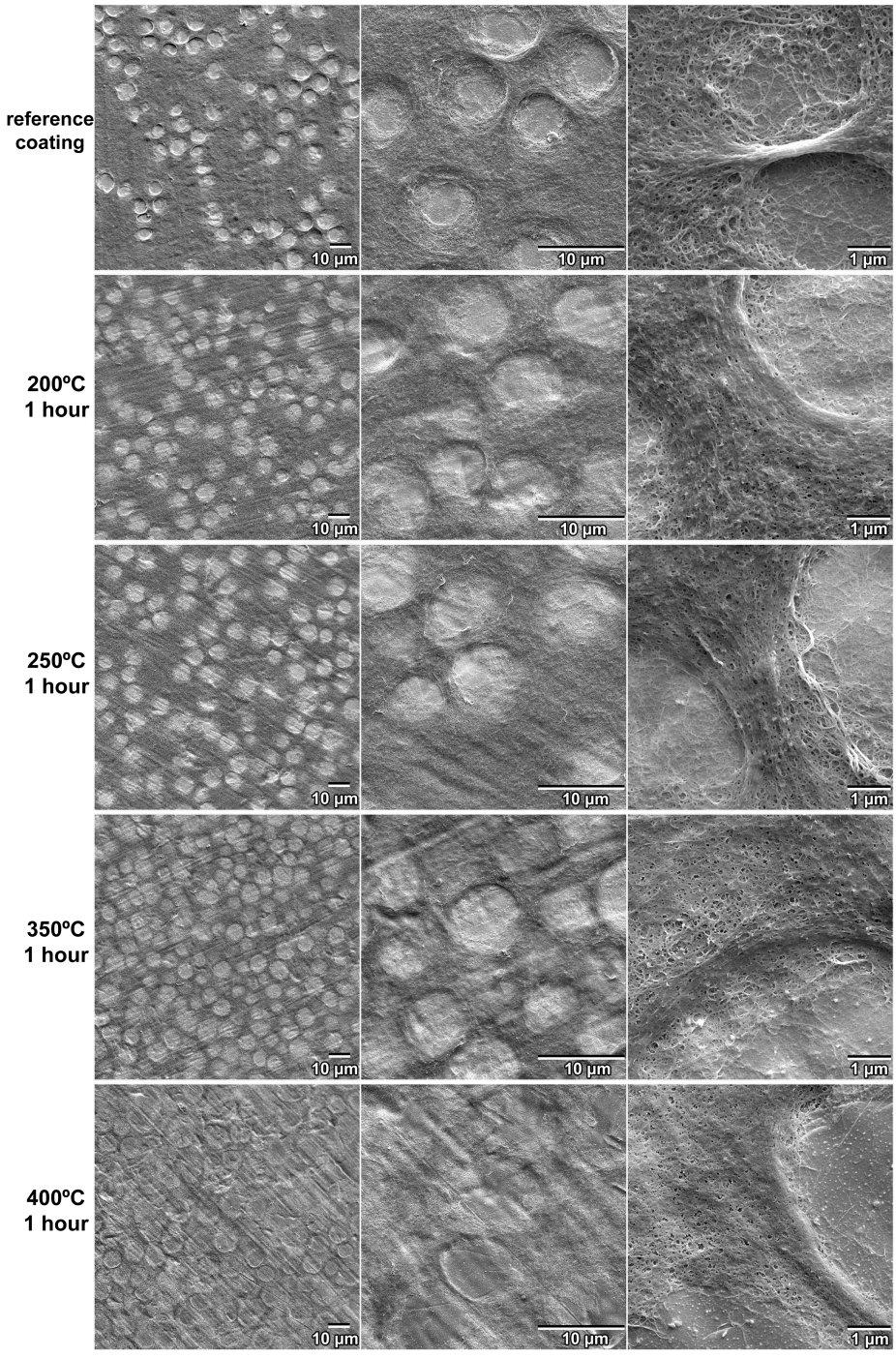

Figure 47 - SEM micrographs of coatings from the bake experiment at three different magnifications; 500x, 2000x, and 10000x for the left, center, and right columns respectively. The images depict typical regions in the coatings of the reference and the coatings that were baked at 200ºC, 250ºC, 350ºC, and 400ºC.

4.4.7 Section summary

A solution of weak polyelectrolyte cationic polymer that was protonated by HCl was received and utilized in electrophoretic deposition. This enabled the polymer with the ability to change from soluble positive charge to insoluble neutral charge as a function of pH. This mechanism facilitates cathodic deposition since the high pH at the cathode due to electrolysis reactions causes the polymer to become neutrally charged and insoluble.

Initial concentrations of acid were found to be too high, causing excessive bubble formation. Efforts were made to reduce the acid concentration and better polymer coatings were achieved. Experimentation moved on to depositing a new solution of cationic weak polyelectrolyte functionalized SWNTs with excess free polymer.

Explanations were proposed for the observations that smoother coatings were produced with lower concentration solutions, shorter deposition durations, and higher ethanol:water ratios. SEM and AFM observation revealed that the coating structure contained a high density of crater-like voids. It was proposed that the SEM results suggested there are also voids beneath the surface in thick coatings and this theory was validated using Monte Carlo simulation.

A step-by-step process was also proposed to explain the void growth behaviour in the coatings as a result of the presence of bubbles attached to the coating surface during deposition and the suggested process fits well with the SEM observations. The process was also used to suggest the reasons why higher voltages were generally observed to produce coatings with smaller voids.

A series of deposited coatings were baked in an oven with the intention that elevated temperatures might allow the deposited polymeric material to relax and partially fill the crater-like voids resulting in a reduction in surface roughness. SEM results found that

baking had no effect on the size of the voids but the higher temperatures reduced the coating thickness and affected smaller scale morphology through material decomposition. It was concluded that high temperature baking does more harm than good to the coating morphology. Low temperature baking may still be beneficial due to the likely evaporation of any remaining trapped solvent.

4.5 Acetic Acid Protonated Polymer

4.5.1 Introduction

The crater-like voids that covered the surface of the coatings that was deposited using HCl protonated material were very likely the result of gas bubble formation at the substrate electrode. The formation of gas is significantly increased when there is a high ionic content in the solution and using HCl to protonate the polymer certainly increases the amount of ions because of the nature of strong acids. Any small amount of HCl in excess of what is necessary to protonate most of the polymer's functional end groups will fully dissociate into H^+ and Cl^- ions which will undergo reduction and oxidation reactions at the cathode and anode respectively to form H_2 and Cl_2 gas. This excess gas generation could be minimized if the amount of excess ions can be minimized. Perhaps a more appropriate approach to polymer protonation is to use a weak acid.

Weak acids such as acetic acid have a much lower dissociation constant compared to strong acids so excess amounts will not produce as many extra ions. Another benefit is due to Le Châtelier's principle because the protonation of the neutral polymer consumes H^+. According to Le Châtelier's principle, the decrease in H^+ concentration causes the dissociation equilibrium reaction to compensate by shifting towards the production of

more H^+. Using acetic acid as an example, the following equilibrium reaction would shift to the right:

$$CH_3COOH \longleftrightarrow CH_3COO^- + H^+ \qquad \text{(EQ22)}$$

This shift in equilibrium means that the amount of acetic acid actually needed for polymer protonation is low because more H^+ is produced as it is consumed by the polymer protonation. This effect also decreases the excess H^+ because the acetate ion is not being consumed and therefore exerts chemical potential to push the reaction to the left. The result is that only small amounts of a weak acid are necessary to protonate the polymer and due to equilibrium mechanics there is not a large excess of H^+ ions beyond what was consumed in polymer protonation. This should translate to a much smaller amount of gas bubbles being generated at the electrodes compared to protonation with strong acid.

4.5.2 Solution preparation

A new batch of PDAFP was received from the Adronov group in powder form to enable a higher level of control over the solution. The powder was completely insoluble in water and drops of acetic acid were added until the powder was fully dissolved due to protonation of the side chain functional groups to enable solubility. This occurred after 0.2% by volume of acetic acid was added to the water and polymer mixture. The resulting 6 $g \cdot L^{-1}$ aqueous polymer solution became the stock solution for experimentation and was diluted with ethanol to give various polymer concentrations. The stock solution was also used to functionalize individual single-walled carbon nanotube by thoroughly mixing with ultrasonicated nanotubes and centrifuging to remove any remaining insoluble material.

4.5.3 EPD coatings at various concentrations

Similar to the previous coatings that were protonated with HCl, the acetic acid protonated polymer material and functionalized carbon nanotubes produce better quality coatings at lower solution concentrations. Spanning multiple batches of experiments, three different concentrations of protonated polymer and functionalized carbon nanotube solutions were utilized. The coatings produced from 0.25 $g \cdot L^{-1}$ solutions were observed to be smoother and nearly monochromatic compared to the coatings produced from 1.0 $g \cdot L^{-1}$ and 0.5 $g \cdot L^{-1}$ solutions which had some texture and an assortment of interference-like color bands indicating that the thickness is not consistent across the coating. Figure 48 shows photographs of typical polymer functionalized carbon nanotube coatings that were deposited from solutions at the three different concentrations. Concentrations below 0.25 $g \cdot L^{-1}$ did not show additional improvements in quality and were only used occasionally because the percentage of material remaining in solution was depleted too quickly at very low concentrations. Pure polymer coatings deposited from 0.25 $g \cdot L^{-1}$ were similar in appearance and quality to those with functionalized nanotubes.

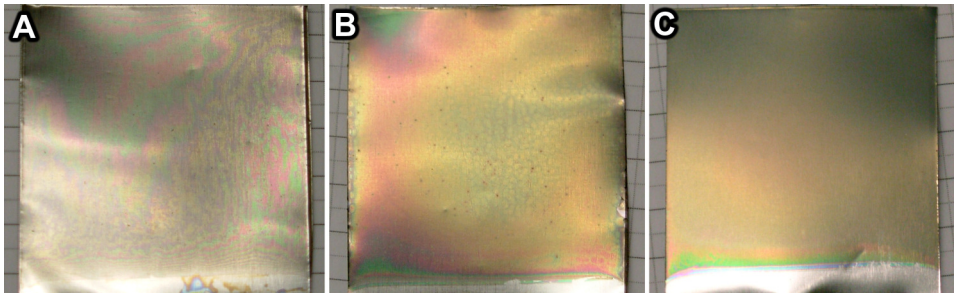

Figure 48 - Photos of polymer functionalized carbon nanotube coatings deposited from three different concentrations. A) 1.0 $g \cdot L^{-1}$ solution at 60 V for 2 min. B) 0.5 $g \cdot L^{-1}$ solution at 70 V for 1 min. C) 0.25 $g \cdot L^{-1}$ solution at 70 V for 1 min. The ethanol concentrations for these experiments were 83%, 92%, and 96% respectively.

The causes for the improvement in quality with lower material concentrations of acetic acid protonated material are likely the same as those hypothesized for previous polymer solutions. Lower concentrations require additional dilution which enables the use

of more ethanol in favor of less water. Secondly, since the deposition rate scales with concentration lowering the concentration of material results in a slower deposition rate. This may have the advantage of allowing more time for trapped gas molecules to escape and also for the depositing material to assemble more efficiently into a densely packed film.[73] Lastly, lower concentration reduces the probability of dipole-dipole interactions between macromolecules. This enables less agglomeration of material prior to deposition which may result in coatings that are smoother and denser due to the more efficient packing of less entangled particles.

4.5.4 Effect of acetic acid protonation compared to HCl

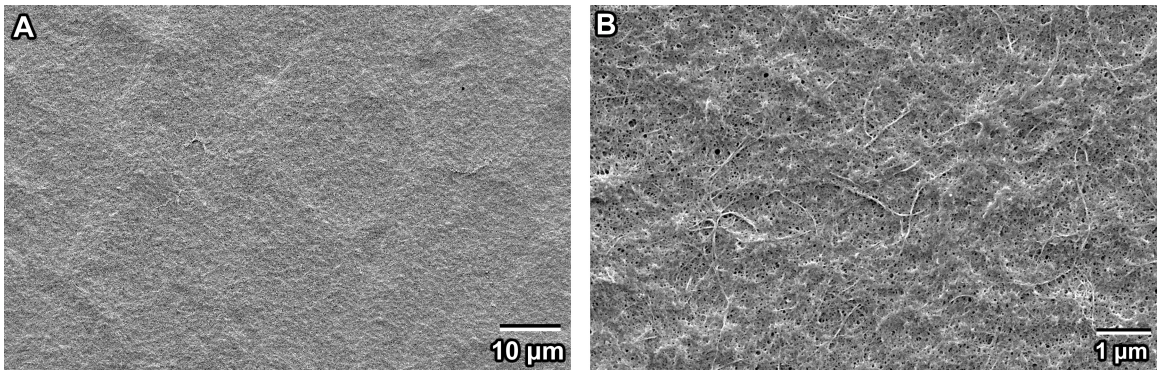

Figure 49 - SEM micrographs of a polymer functionalized carbon nanotube coating captured at 1000x (A) and 10000x (B) magnification, deposited at 50 V for 1 min from a 0.25 $g \cdot L^{-1}$ solution. The images show that acetic acid protonation eliminated the presence of bowl-shaped voids.

The main purpose of switching from HCl protonation of the end groups to protonation by a weak acid such as acetic acid was to minimize the ionic content of the solution for the purpose of preventing the formation of bowl-shaped voids. Using SEM, it was observed that the coatings produced from solutions of polymer and polymer functionalized carbon nanotubes that have been protonated by a minimized amount of acetic acid no longer posses any trace of the bowl-shaped void defects in the microstructure. Figure 49 shows two SEM micrographs of a polymer coating containing

functionalized nanotubes captured at 1000x and 10000x magnifications, and deposited at 50 V for 1 minute from a 0.25 $g \cdot L^{-1}$ concentration solution. These surface images are typical of the coatings produced from solutions that were protonated with acetic acid. They demonstrate the elimination of the bowl-shaped voids that were consistently observed in the coatings that were produced using HCl protonated polymer solutions such as in Figure 41, which is the same magnification as Figure 49A for comparison.

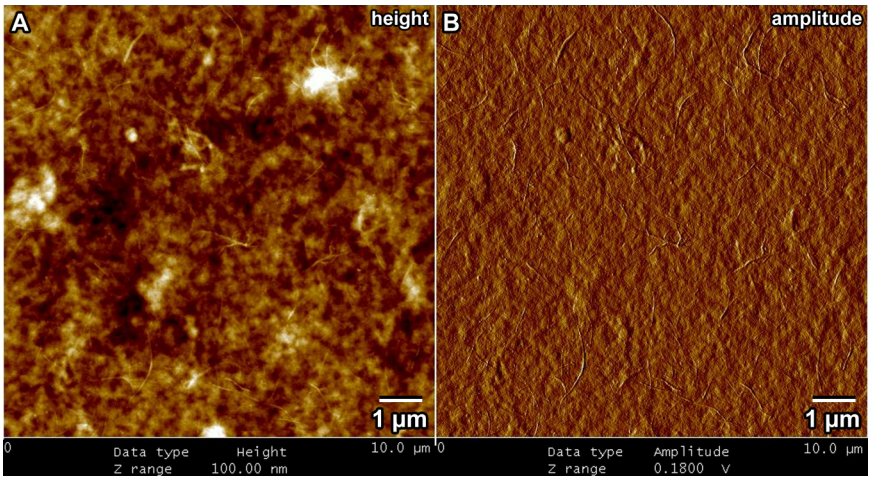

Figure 50 – AFM images from a functionalized nanotube coating surface showing height and amplitude data in a 10 µm x 10 µm tapping mode scan using the "E-scanner". The black-to-white height scale in the data in "A" is 100 nm. The data in "B" is the tip amplitude, which is used to amplify the appearance of height changes and also provides a more natural looking image. The coating was deposited at 70 V for 1 min from a 1.0 $g \cdot L^{-1}$ concentration solution.

Atomic Force Microscopy was also utilized to observe the coatings that were deposited from acetic acid protonated solutions. Since AFM specimens do not require cleaning or special coatings and can be operated in non-contacting modes, the data can be used to verify that the lack of voids observed in SEM is not a result of specimen preparation or beam damage. The data displayed in Figure 50 was typical of the observed functionalized nanotube coating showing no sign of the large voids that existed in coatings that were deposited from HCl-protonated solutions. This AFM data can be compared to the that from the HCl-protonation experiments in Figure 39C which is the

same dimensions as in Figure 50 except due to the depth of the bowl-shaped crater the black-to-white scale was 10 times larger.

As suspected upon the switch to a weak acid protonation technique, the reduction in the ionic content of the solution due to the minimization of excess acid resulted in a major improvement in coating quality. The acid reduction was significant enough to eliminate the formation of bowl-shaped voids that were suspected to be the product of excessive H_2 gas generation at the cathode when HCl was used to protonate the functional groups of the polymer side chains. The visible bubble formation during deposition was nearly eliminated and even at high voltages no large voids were observed in the coating microstructure.

4.5.5 Effect of the functionalization technique on nanotube agglomeration

In early experiments with the polymer that had been protonated with acetic acid, SEM observation of the coating morphology of deposited polymer functionalized carbon nanotubes revealed an unusual finding. There was an abundance of agglomerated carbon nanotube bundles scattered in patches throughout the coating. Various SEM micrographs of this phenomenon have been compiled in Figure 51.

The agglomerations were suspected to be the result of the specific functionalization technique that was used to prepare the carbon nanotube solution. The technique involved the dilution of aqueous 6.0 $g \cdot L^{-1}$ concentration polymer solution by ethanol to get the polymer concentration down to 2.0 $g \cdot L^{-1}$. The next step was the addition of 5% dry SWNTs by polymer weight to the solution and then the mixture was placed in an ultrasonic bath and finally the centrifuge.

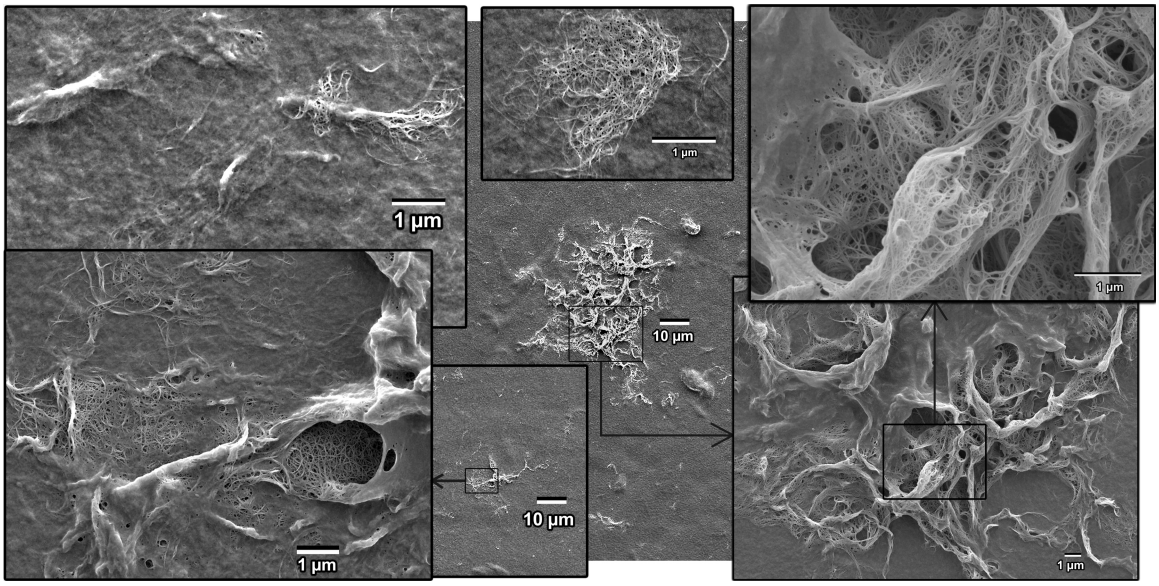

Figure 51 - An assortment of SEM micrographs at various magnifications showing agglomerations of functionalized carbon nanotubes within the coating surfaces.

The hypothesized problem with this technique is entirely about the way the carbon nanotubes were introduced to the mixture. Unmodified carbon nanotubes exist in a state of entangled bundles held together by π-π stacking and while contact with the polymer in solution causes the polymer to functionalize the nanotube surface, the polymer still requires access to the surface for functionalization to take place. Ultrasonication is effective at dispersing the nanotubes but in this case perhaps there was not enough time for the dry nanotubes to fully untangle and de-bundle. The polymer may have been able to envelope the bundles which would render them soluble, but may not have had access to all the single nanotube surfaces within the bundle.

I proposed a modified functionalization technique to change the order of mixing and also to increase the ultrasonication duration. Before introducing the SWNTs to the aqueous polymer solution they were dispersed in ethanol by extensive ultrasonication. Then the well dispersed nanotube suspension was mixed with the polymer solution and again the mixture was subjected to the ultrasonic bath and centrifuge. There appeared to

be less insoluble solid material after centrifuging which suggests that the nanotubes were more thoroughly dispersed.

The resulting EPD coatings of functionalized SWNTs from the new batch were found to contain significantly less agglomerations of SWNTs. Visible SWNT bundles were still present, such as those in Figure 49B, but there were very few large clusters such as those depicted in Figure 51. The near elimination of agglomerated bundles was suspected to be the result of the improved order of mixing and longer ultrasonication durations during the polymer functionalization process.

4.5.6 Control over coating thickness

It is necessary to have control over the coating thickness because it is a very important parameter for some coating applications. For example, tuning the thickness of the active layer in an organic solar cell is one of the major tools for optimizing the device performance.

A wide range of coating thicknesses were achieved throughout the various experiments, with some experiments specifically focused on producing very thin or very thick coatings of both pure polymer and composites of functionalized SWNTs with free polymer. The thinnest EPD coatings of both types that were observed by SEM were found to be slightly less than 100 nm in thickness. The cross sectional SEM micrographs of these thin coatings are given in Figure 52.

Thin EPD coatings are achievable using solutions of low to moderate concentrations such as 0.05 $g \cdot L^{-1}$ to 0.25 $g \cdot L^{-1}$, the time should be limited to the approximate range of 30 sec to 1 min, and the applied voltage should be 30 V to 40 V. The ranges of these variables are likely close to their minimum values. If the concentration is too low there

might not be sufficient agglomeration at the electrode to produce a uniform coating. If the voltage is too low there might not be enough driving force for electrophoresis or for the high pH region to be sufficiently established. If the duration is too short there might not be enough time for the build up of OH^- ions to create the high pH region or enough time for the electrophoresis to establish sufficient agglomeration.

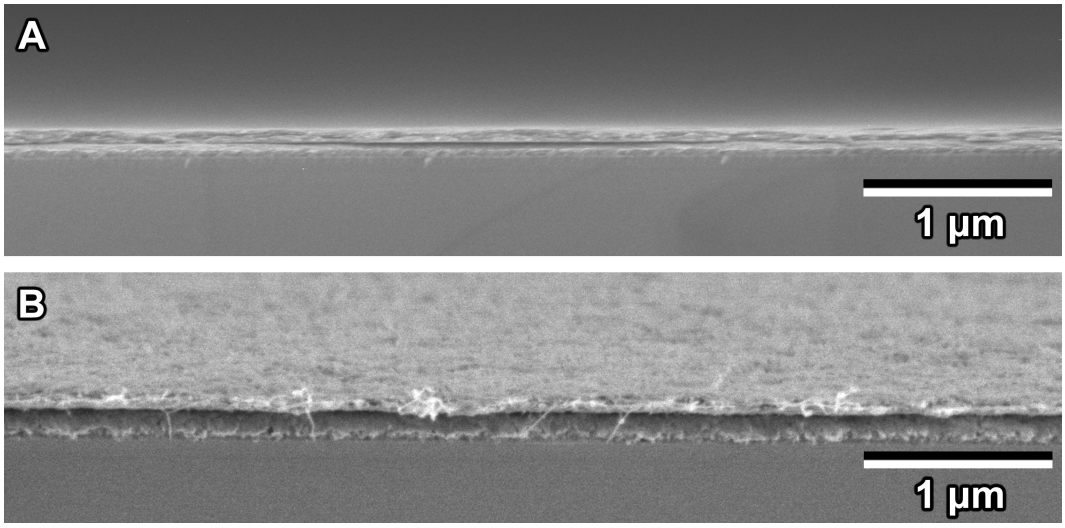

Figure 52 - SEM cross section images of thin EPD coatings captured at 20000x using a 1.5 keV electron beam. A)~86 nm thick polymer coating deposited at 40 V for 30 sec from a 0.25 g·L^{-1} concentration solution. B)~76 nm thick functionalized nanotube coating deposited at 30 V for 1 min from a 0.25 g·L^{-1} concentration solution.

Thinner coatings than those in Figure 52 are possible but difficulties arise as the minimum viable values of the deposition variables are approached. Experimentation using conditions below the ranges described above typically resulted in low quality, non-homogenous looking deposits, or no deposit. Additionally, measurement of very thin coatings may require a different technique because SEM observation becomes difficult with very thin coatings since there is not enough coating material to accurately adjust the focus and correct the astigmatism at the high resolutions that are required to capture images of coatings that are less than 100 nm in thickness.

At the other end of the spectrum, relatively thick coatings near 10 μm in thickness have been produced such as those imaged by SEM and shown in Figure 53. The thickest coating across all experiments that was measured is a functionalized SWNT deposit at 10.8 μm, which is thicker than those in Figure 53. However, no SEM image is available since the coating was measured using optical profilometry for the transparency experiment that will be discussed shortly.

Thick coatings of approximately 10 μm can be produced using relatively high voltages such as in the range of 50 V to 70 V, from above normal solution concentrations such as 0.5 $g \cdot L^{-1}$, and deposited for an extended duration in the range of 10 min to 15 min.

The voltage and concentration have practical upper limits while the duration has no limit other than the gradual decline of the deposition rate to zero. Previously described experimentation has revealed that above an ideal voltage range the quality of the resulting coating declines due to excessive gas generation at the electrodes. High voltage also likely causes agglomeration of the material prior to deposition which would increase the roughness and porosity. The deposition from high concentration solutions was found to produce visibly lower quality coatings, as demonstrated in Figure 48 and previously explained, but 0.5 $g \cdot L^{-1}$ yields an acceptable compromise between good quality and maximum thickness.

Coatings with thicknesses well beyond 10 μm are likely possible. If there are any applications where a large coating thickness is much more important than the roughness, density, thickness variation, and material cohesion, then it may be advantageous to exceed the typical upper voltage range in order to maximize thickness. It would also be beneficial to use a large beaker and increased solution volume so that the concentration does not significantly decrease as material is deposited. The only limit to coating thickness would

then become the increasing electrical resistance of the coating as thickness increases. Since the applied voltage is constant, the increase in series resistance causes a larger voltage drop over the coating which reduces the electric field through the solution resulting in the decline of the deposition rate.[73]

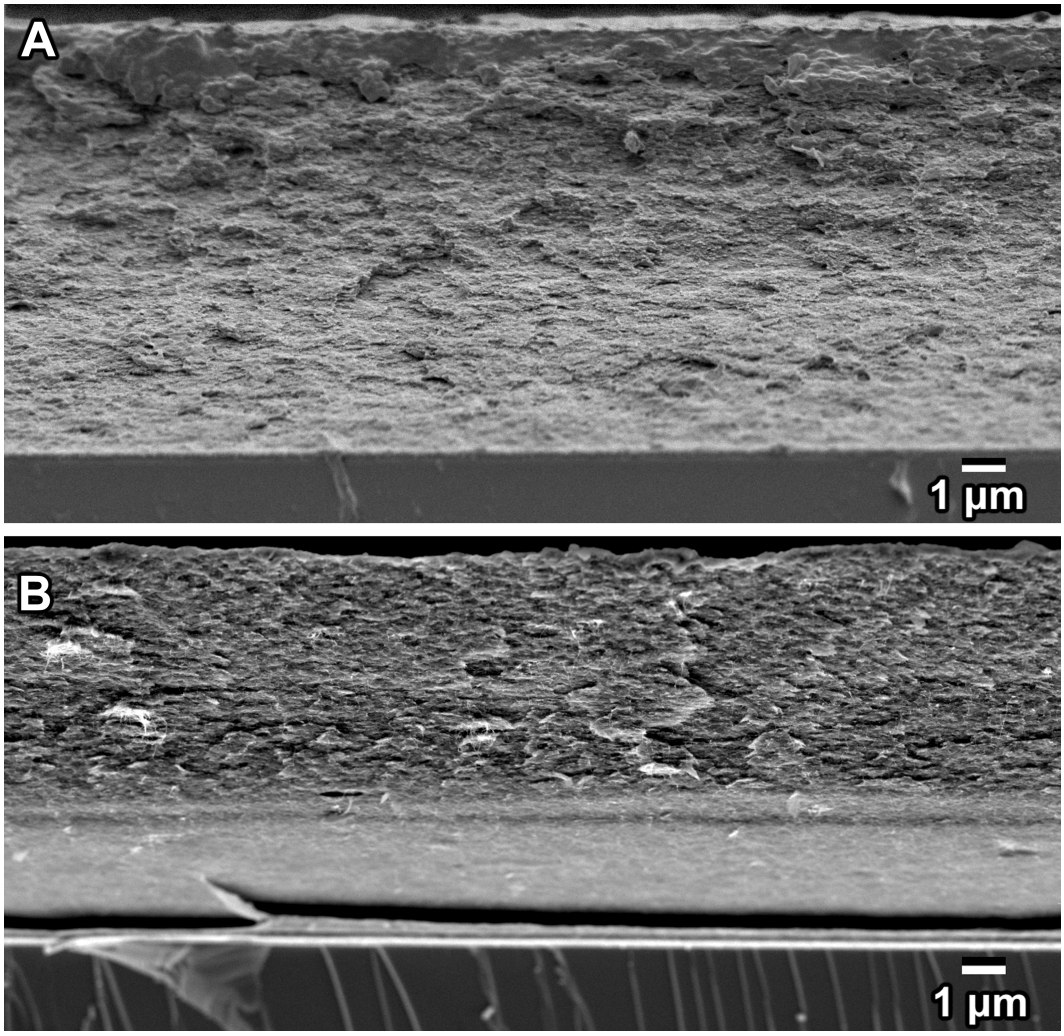

Figure 53 - SEM cross section images of thick EPD coatings captured at 5000x using a 1.5 keV and 3 keV beam for A and B respectively. A)~9.6 µm thick polymer coating deposited at 60 V for 15 min from a 0.5 g·L^{-1} solution. B)~6 µm thick functionalized nanotube coating deposited at 50 V for 4 min from a 1.0 g·L^{-1} solution. In image B the coating appears to be protruding from the substrate and curled upwards due to an imperfect cleave during SEM specimen preparation, therefore the thickness was estimated from measuring only the part that appears to be the true cross section and is in focus.

Comparing the thinnest and thickest coatings that were measured in cross section using SEM, the demonstrated thickness range is from less than 100 nm to approximately 10 μm. The difference between the extremes is two full orders of magnitude which indicates that EPD is a versatile technique for producing coatings spanning a wide range of thicknesses and therefore potentially useful to a variety of applications. Achieving thicknesses anywhere between the two extremes is simply a matter of adjusting the applied voltage, solution concentration, and tuning the duration of deposition.

Control over coating thickness was further demonstrated in an experiment to produce a series of polymer functionalized SWNT coatings spanning the known thickness range. The deposition conditions for each of the 9 specimens are displayed in Table 2. The thickness was tuned by first setting the solution concentration and then adjusting the voltage and time at each concentration step to achieve increasingly thicker coatings starting from a very thin coating.

Table 2 – Deposition conditions for the series of functionalized SWNT coatings that span the known thickness range, and the corresponding coating thicknesses measured using optical profilometry.

	Concentration	Voltage	Time	Thickness
1	-	-	-	(uncoated)
2	0.05 $g \cdot L^{-1}$	40 V	1 min	80 nm
3	0.05 $g \cdot L^{-1}$	50 V	2 min	170 nm
4	0.10 $g \cdot L^{-1}$	50 V	2 min	370 nm
5	0.10 $g \cdot L^{-1}$	50 V	6 min	790 nm
6	0.40 $g \cdot L^{-1}$	50 V	2 min	1220 nm
7	0.40 $g \cdot L^{-1}$	50 V	4 min	1840 nm
8	0.40 $g \cdot L^{-1}$	55 V	7 min	3260 nm
9	0.75 $g \cdot L^{-1}$	50 V	5 min	5060 nm
10	0.75 $g \cdot L^{-1}$	60 V	12 min	10800 nm

ITO coated glass was used as the substrate because of its transparency which enabled the measurement of light absorbance across the visible spectrum for each specimen.

Figure 54 is a photograph of uncoated ITO followed by the 9 EPD coatings of increasing thickness and decreasing transparency. The coatings are arranged from thinnest to thickest and placed over printed numbers to aid in the visualization of the optical transparency. The numbers under each specimen in Figure 54 are consistent with those in Table 2. The corners of each specimen surface are uncoated because they were used as electrical contact points to provide current to the ITO top layer in the EPD setup and were thus shielded from deposition.

Figure 54 - A photograph of a series of polymer functionalized SWNT coatings deposited on ITO. They are arranged in order of increasing coating thickness and placed over printed numbers to help visualize the transparency of each coating. The first specimen is uncoated for comparison.

The absorbance of each specimen was measured using a UV-Visible Spectrophotometer and the data was converted to the percent of light transmitted through the specimen for improved graphical visualization. Figure 55 is a graph of the percent transmittance vs. the wavelength of incident light for each specimen. The uncoated ITO was used as a baseline to eliminate the contribution of the substrate to the coating data. To the right of each curve is the thickness of each coating measured in nanometers using optical profilometry. The strong absorption in the 300 nm to 400 nm range corresponds to the absorption of the polymer, while the carbon nanotubes absorb broadly across the measured spectrum.

Clearly there is a tradeoff between coating thickness and transparency with thin coatings being highly transparent across most of the visible spectrum while the thickest coatings have approximately zero transparency across the measured optical range. For applications such as an organic solar cell there would be an optimum thickness to obtain

maximum power conversion efficiency. The high absorption of thick coatings is useful to prevent the transmission of photons but increasing the thickness has a significant negative impact on the coating's charge carrier transport properties due to the low carrier mobility in the coating material. Based on the data of Figure 55, the thickness of a solar cell device using this composite material should probably not exceed approximately 400 nm. At this thickness the absorption within the polymer's absorption peak range has reached approximately 100%. Assuming that only photons absorbed by the polymer can be converted, there is likely no benefit to increasing the thickness any further and doing so would only negatively impact the charge carrier transport through the device. The optimal thickness for maximum efficiency could potentially be much lower than 400 nm if the transport issues tend to dominate the device performance characteristics over maximizing absorption, but it is not likely to exceed 400 nm.

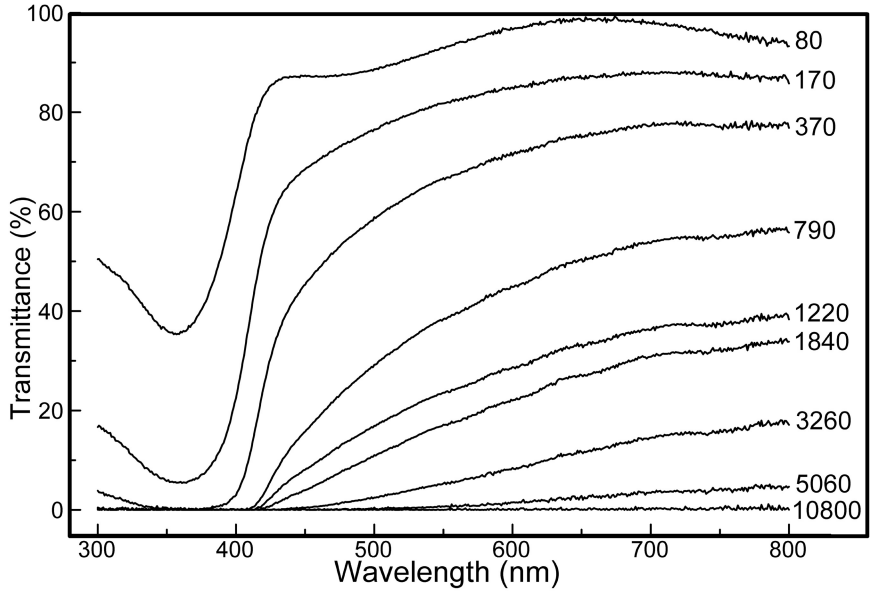

Figure 55 - A plot of light transmittance as a function of incident wavelength for each of the 9 coated ITO specimens of different thickness. The top curve and the bottom curve correspond to the thinnest and thickest coatings respectively. The average thickness for each specimen, measured in nanometers using optical profilometry, is given to the right of each curve.

4.5.7 Quartz crystal microbalance analysis of the deposition rate

The deposition yield as a function of time was observed in real-time using a quartz crystal microbalance (QCM). In addition to demonstrating the effects of applying different voltage or concentration conditions, this also revealed how the general deposition behavior changes at different stages of the process.

EPD experiments utilizing the QCM were conducted with the quartz crystal as the cathode substrate. Lower than usual voltages (3 V and 5 V) had to be used to reduce the problems associated with high resonant resistance when the current is high, since it causes a polymer concentration buildup near the cathode, resulting in a locally increased viscosity. The electrode separation distance was therefore reduced to offset the drop in electric field strength caused by the decreased voltage. A platinum sheet was used for the anode spaced 3 mm away from the substrate surface. The solution was also diluted down to the polymer concentrations 0.05 $g \cdot L^{-1}$ and 0.1 $g \cdot L^{-1}$ in order to help keep the viscosity low. Solutions containing functionalized nanotubes were not tested due to the higher viscosity of the solution. However, since it is the charge of the polymer that facilitates the deposition, the trends observed by QCM experimentation of solutions containing functionalized nanotubes would likely look the same as the results from a solution containing purely polymer.

The QCM results are displayed graphically in Figure 56 as the Sauerbrey mass vs. time starting from the beginning of the deposition. The graph shows the progression of film formation in terms of the mass gained by the quartz crystal electrode substrate.

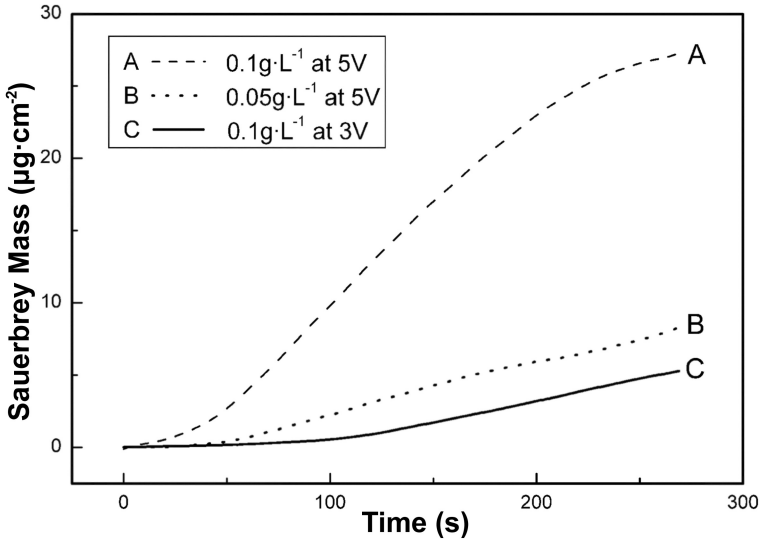

Figure 56 - In-situ quartz crystal microbalance measurement of the Sauerbrey mass vs. time during electrophoretic deposition from a polymer solution.

The comparison between curve "B" and curve "A" shows a large increase in the deposition rate when the polymer concentration is increased. The scaling is found to be greater than linear since the concentration increase by a factor of two resulted in a much larger increase in the amount deposited within the same time. Also the deposition rate, determined by the slope of the linear midsection of the curves, differs by a factor of 3.7.

The comparison between curve "C" and curve "A" similarly shows a large increase in the deposition rate when the applied voltage is increased from 3 V to 5 V. As with the concentration, the voltage scaling is also greater than linear. The difference in voltage was a factor of 1.67 while the resulting increase in the deposition rate was a factor of 4.8.

In addition to the affects of changing concentration and voltage, the shape of the QCM data plots reveal what can be described as three stages in the deposition process. The deposition rate in the starting stage is initially very low but gradually increases with time. After a period of time the deposition rate has reached a steady state where the mass gain vs. time is linear. After a few minutes the deposition rate begins to decline dramatically in the ending stage.

In the starting stage, the deposition rate begins at zero and gradually increases. This behavior is in contrast to what is typically observed in the deposition of ceramic particles where the deposition rate is linear and at a maximum almost immediately.[114] The initial deposition rate behavior of this polymer system is likely due to the kinetics involved in establishing the conditions that facilitate the deposition. Rather than simply a matter of electrophoresis, the successful deposition requires the accumulation of OH^- ions in the vicinity of the cathode to increase the pH to the point where it is high enough to deprotonate the functional groups of the polymer side chains. The sufficient accumulation of OH^- ions requires a period of time that depends on the applied voltage, but not the concentration of the polymer solution since the OH^- comes from the solvent. This is demonstrated by the fact that the deposition of trial "C" in Figure 56 took considerably longer to reach a steady state than trials "A" and "B" which were deposited at a higher voltage and reached their steady state deposition rates after approximately the same duration despite having different concentrations.

The middle stage is the linear portion of the mass vs. time curve where the deposition rate is constant. In this stage the conditions that enable deposition have already been fully established and the deposition rate is at a maximum. The volume of solution can affect the width of this stage because it determines the impact of the decreasing solution concentration as polymer is being deposited on the substrate and removed from the solution. A low concentrated solution could be depleted of polymer fast enough that the deposition rate will decline as the concentration significantly decreases. If the linear region is wide then it is probably safe to approximate the concentration as constant over each individual deposition run. The depletion of polymer is thus not likely to be the primary cause of the eventual decline in the deposition rate.

The third stage is the prominent decline of the deposition rate and it is the result of the quantity of material already deposited. Due to the high resistance across the coating thickness compared to the solution, under constant voltage conditions the voltage drop over the insulating coating causes a drop in the electric field that influences the electrophoresis of material between the coating surface and the counter electrode.[73] This decreases the driving force and causes a decrease in the particle velocity, resulting in the decline of the deposition rate.

4.5.8 Layered deposition

An additional form of coating control available with EPD is the ability to deposit multiple layers of different materials. The ease of producing coatings composed of various layers expands the use of the EPD technique towards additional niche application. In an organic solar cell for example, it might be advantageous in some systems to deposit a small barrier layer to prevent a short circuit or to improve the energy levels for charge carrier collection. Another example is to deposit different layers of photoactive material that are tuned for different wavelength ranges in order to enable the efficient capture of light energy from a broader spectrum.

The deposition of more than one layer is demonstrated in Figure 57, where a layer of polymer containing functionalized carbon nanotubes was first deposited, and then a second layer of pure polymer was subsequently deposited on top. This can be achieved by simply placing the electrode substrate which has been coated with the first layer into another beaker to undergo a second EPD run with a different solution. This process can be repeated for additional layers. Due to the decline in the deposition rate when the coating is thick, subsequent layers may require additional time or higher applied voltage to achieve the desired thickness.

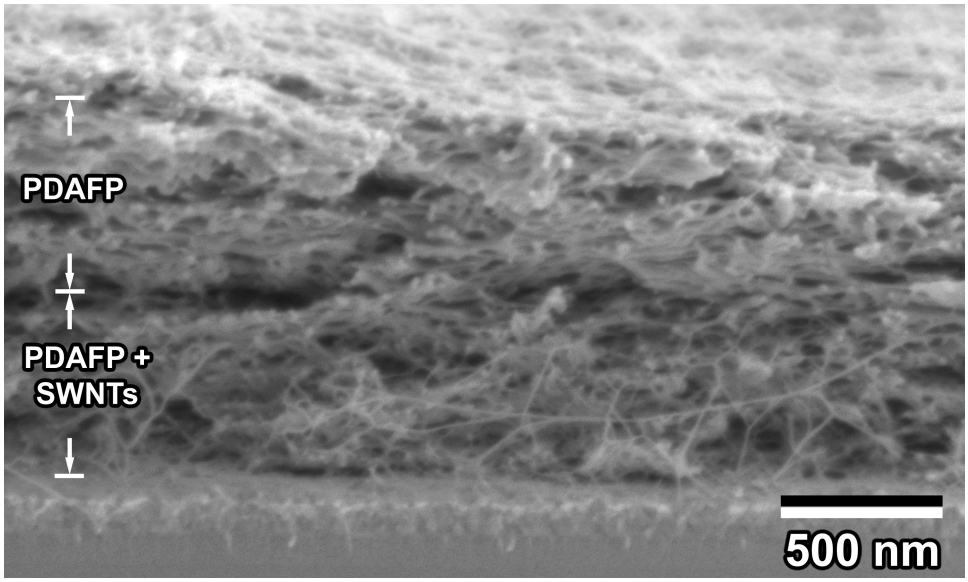

Figure 57 - SEM micrograph of a cross section of an 1140 nm thick bilayer EPD coating with polymer functionalized carbon nanotubes on the bottom and a pure polymer layer on the top. The image was captured at 40000x using a 1.5 keV electron beam.

4.5.9 Discussion of nanotube alignment

The alignment of carbon nanotubes within a coating can be potentially useful or potentially harmful, depending on the coating application. It is therefore appropriate to report observations of perceived alignment and to also consider the false positive observation of alignment.

Many of the SEM cross sectional images of EPD polymer films containing functionalized carbon nanotubes show a disproportionate amount of the nanotubes to be oriented in the vertical direction. This direction is orthogonal to the substrate and parallel to the direction of the electric field during EPD. However, it can not be hastily concluded that the nanotubes must be depositing in an aligned orientation without careful examination of the SEM micrographs and consideration of the specimen preparation techniques.

Deposition for cross sectional observation was conducted with platinum-coated silicon wafer substrates which enabled a sufficiently clean fracture of the substrate and coating by pressing a scriber at the substrate edge to initiate a fracture along a cleavage plane. The fracture would apply tension within the coating orthogonal to the direction of crack propagation as the substrate cleaves into two pieces and forces the coating to fracture with it. It is important to consider how the polymer and nanotubes likely react to the forces applied to them during this fracture.

The mechanical properties of the custom-made polymer, PDAFP, have not been studied so information is unavailable, but based on similarly structured polymers it is likely to have a glass transition temperature significantly above room temperature. The cracks and fracture surfaces of the polymer that were observed using SEM also suggest that the polymer fractures in a brittle manner and it usually fractures neatly along the same plane as the cleaved silicon substrate.

Different behavior can be expected from the carbon nanotubes within the polymer matrix because they are very flexible and have an extremely high tensile strength. A curved nanotube put under tension will fully straighten and even stretch slightly before fracturing; much like a rope would behave. Carbon nanotubes within the film under the tension of a fracturing polymer matrix would likely get pulled out of the matrix as they straighten and stretch under the tensile load as the polymer crazes and then cracks. There is clear evidence for this phenomenon in Figure 58 showing straightened carbon nanotubes that have been pulled out of the polymer matrix due to tension.

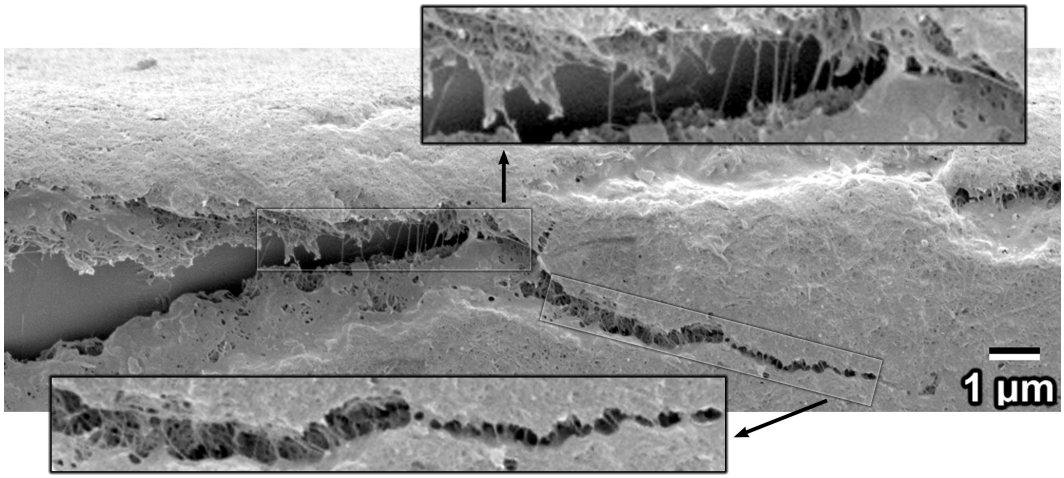

Figure 58 - SEM micrograph from a cross section specimen of an EPD polymer coating containing functionalized carbon nanotubes. At a location where the coating did not fracture along the same plane as the substrate, a section of the coating remained hanging over the substrate fracture edge (a rare case) and contains a crack-craze. Straightened carbon nanotubes that have been pulled out of the polymer matrix are clearly visible spanning the crack gap and they are also found within the fibrillar bridges between the microvoids of the craze. This image was captured at 4500x magnification with a 1.5 keV beam using a 3.7 mm working distance.

Once the coating is fully cleaved into two pieces and the nanotubes have either broken or were completely pulled out at one end, the straightened and pulled nanotubes would then be left dangling. If most of them fall downward due to gravity or an electrostatic attraction then they might give the appearance of nanotube alignment during observation of the cross section. It is important to separate this false positive alignment from true nanotube alignment that may occur during electrophoresis and subsequent deposit formation.

Occasionally some portions of the coating cross section did not fracture cleanly and coating material remains overhanging the substrate fracture edge. In some of these cases the pulled-out nanotube phenomenon was clearly observable and various examples of this situation are provided in Figure 59. The images labeled “A” and “B” are examples where the polymer matrix slightly overhangs the edge and free dangling nanotubes are visible. The images labeled with “C” and “D” show thin and thick coating cross sections that

fractured in approximately the same plane as the substrate but contain nanotubes that have been pulled outward and are freely dangling below the base of the coating. It is quite obvious that the exposed nanotubes in these examples are positioned with vertical alignment as a result of the fracturing mechanism, but these are only special cases and not the typical appearance of a cross section. Normally the coating is cleanly split along the same plane as the cleaved substrate and it is usually much more difficult to attribute the nanotube orientation entirely to the fracturing mechanism.

The alignment of carbon nanotube tendrils in the electric field during the deposition from an anionic polymer functionalized nanotube solution was previously discussed. It was suggested with literature precedent that the tendril orientation parallel to the electric field is the result of the electronic polarization of the nanotubes and subsequent electrostatic attraction of the polarized structures.

Nanotube polarization leading to a dipole-induced chaining mechanism has also been suggested by Quale and Talbot with the addition of assistance from a pre-coat layer to facilitate the stability of the substrate-normal nanotube orientation.[115] It has been suggested that special techniques are required to preserve substrate-normal nanotube orientations when the electric field is removed and also to survive through the drying process.[115, 116] Additionally, carbon nanotube alignment induced by the electric field has been reported with assistance from a polymer base coating[117] and due to the anisotropy of the electrophoresis velocity of nanotubes having different spatial orientations with respect to the electric field.[118] The electrophoretic mobility of an infinitely long cylinder oriented parallel to the electric field has been theoretically determined to be twice as large as when the cylinder is oriented orthogonally to the electric field.[119] This implies that the deposition rate of field-oriented cylinders, and thus carbon nanotubes, is higher than other

orientations and it also suggests that a cylindrical particle may rotate within the suspension to travel in this higher mobility orientation.

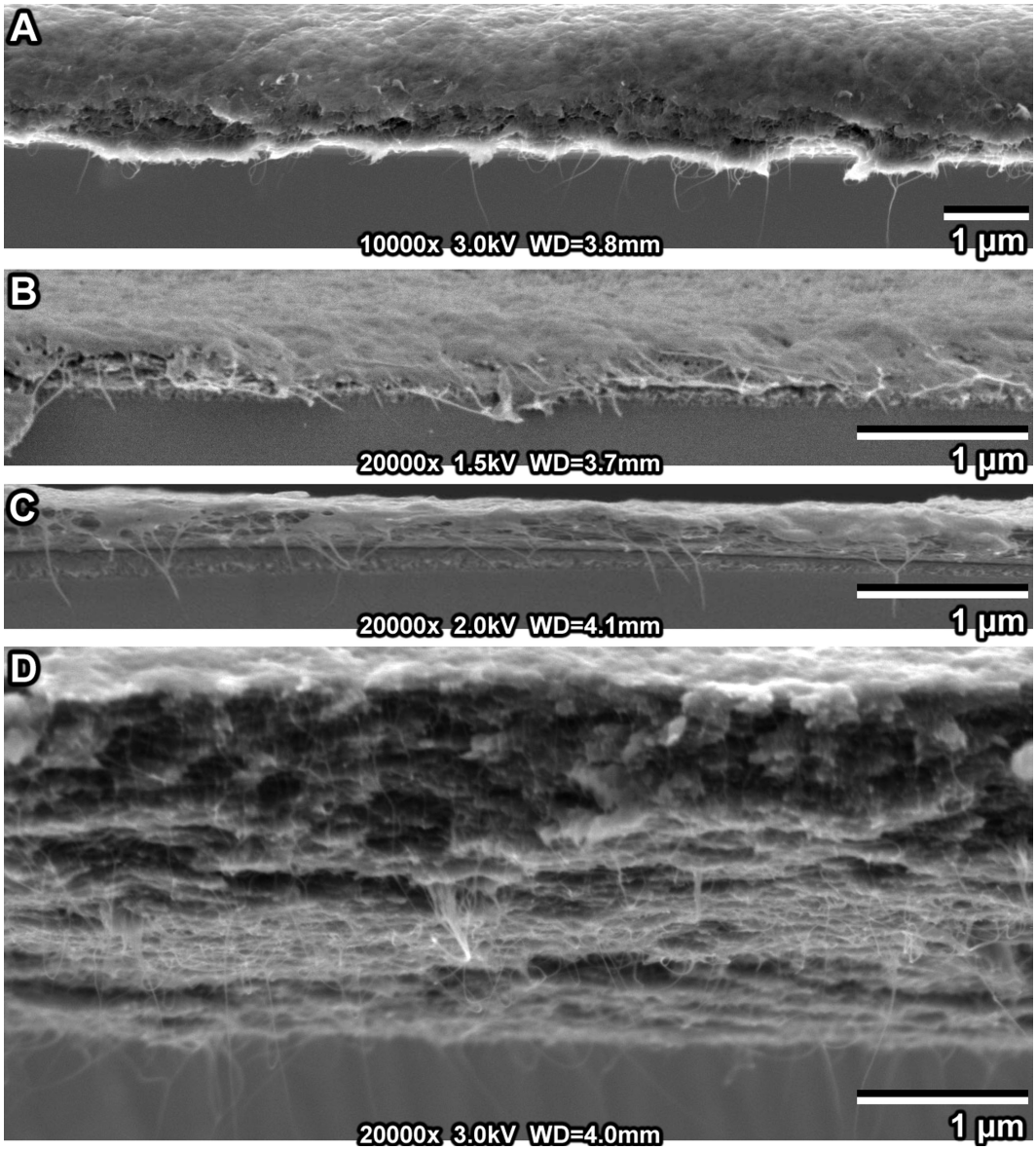

Figure 59 – Various SEM cross sectional images of EPD polymer coatings containing functionalized carbon nanotubes showing examples of pulled and hanging nanotubes. The specific magnification, acceleration voltage, and working distance are provided under each image.

It is important to realize that the mechanisms behind alignment in the solution during the deposition process do not directly translate to alignment on the dried substrate. The

induced alignment and electronic polarization effects of the electric field do not persist when the electric field is removed. Furthermore, a substrate-normal orientation is not likely to persist after drying because of the high surface energy of a standing nanotube or bundle of nanotubes compared to orientations that lie flat on the substrate. Substrate-normal orientation can be preserved if the base of the nanotube is anchored in a matrix material that is rigid enough to provide support. It is also possible that the nanotubes that are deep within a coating may hold their alignment if that orientation happens to be preserved while the matrix material co-deposits around it.

If true nanotube alignment occurred then identifying it in cross section could be difficult because of the presence of the pulled and hanging nanotube effect since both effects result in vertically oriented nanotubes. Even when there are clear signs of pulled nanotubes, that observation does not rule out the possibility that there is also nanotube alignment in the coating at the same location. Since the two effects look similar it is useful to list key visual characteristics that are likely to be exclusive to either pulled nanotubes or true substrate-normal nanotube alignment.

The following are easily identifiable visual characteristics of nanotubes that have been pulled out of the coating during fracture:

- One end of the nanotube appears to be free and not embedded into the coating.
- A large portion of the nanotube is void of attached polymer and is clearly located externally from the bulk material.
- The free ends of loose nanotubes sometimes appear to be angled slightly outwards from the image plane towards the direction of the suggested tensile force.
- Some loose nanotube ends hang below the base of the coating.
- Hanging nanotubes appear to be very straight as if they have been under tension.

The following are visual characteristics that would be common to true substrate-normal nanotube alignment:

- There is a disproportionately higher than random amount of nanotubes that appear in a vertical orientation within the coating cross section.
- Nanotube alignment is generally vertical but there are variations in the exact angles.
- The vertically oriented nanotubes appear to be embedded into the coating at both ends, which significantly decreases the likelihood that they are oriented by tensile force since one end was not pulled out of the matrix material.
- The vertically oriented nanotubes that exist slightly deeper into the coating than the cross sectional surface are highly unlikely to have been oriented due to pulling.
- There are bends and kinks in the nanotubes, indicating that the structures are naturally oriented and less likely to have been under tensile stress.

There were many instances in SEM cross sectional observation where EPD polymer coatings containing functionalized carbon nanotubes appeared to show substrate-normal alignment and four example images are provided in Figure 60. The appearance of these SEM cross sectional specimens is clearly distinct from the images of Figure 59 where the signs of pulled nanotubes are obvious; however, the images in Figure 60 still contain some of the visual characteristics of pulled nanotubes. Some of the vertical nanotubes have a free end that appears to be dangling, which is a sign that it has been pulled outward from the matrix material. Many of the vertical nanotubes are located externally from the bulk, some of them appear to be straightened, but only a few appear to be angled outward or hang below the base of the coating.

In contrast, the images may also display some of the characteristics of true alignment. The vast majority of visible nanotubes are vertically oriented in the substrate-normal direction yet there is enough variation in the angles to suggest that many of them may not

have been pulled in tension. Additionally, many of the vertically oriented nanotubes appear to be attached to the bulk material at both ends, many contain bends and kinks, and there are even some that are visibly embedded deeper into the coating than the front surface of the cross section where the tensile stress would be the highest.

These SEM cross sections appear to display the visual characteristics of pulled nanotubes and the results also indicate the plausibility of true alignment. It is highly likely that nanotube pulling during the substrate cleaving process is a major contributor to the appearance of vertically oriented nanotubes. However, to claim with certainty that true alignment has or has not also occurred would be a hasty conclusion without a deeper investigation into the study and characterization of electric field-induced substrate-normal nanotube alignment. The results are inconclusive, yet still useful because even the plausibility of oriented nanotubes provides a need for further investigation because it has an impact on potential applications of coatings containing carbon nanotubes produced by EPD.

The alignment of nanotubes could enable some applications such as high density field emission displays. It could also be a cause for concern in other applications where semiconducting properties are more desirable than metallic conduction behaviour such as in an organic solar cell. This could be even more problematic when the length of the nanotubes approaches the thickness of the coating, likely leading to a shunt between the two contacts. A device with those issues may only be able to function properly if the metallic and semiconducting carbon nanotubes can be separated and only the semiconducting variety should be used in such an application.

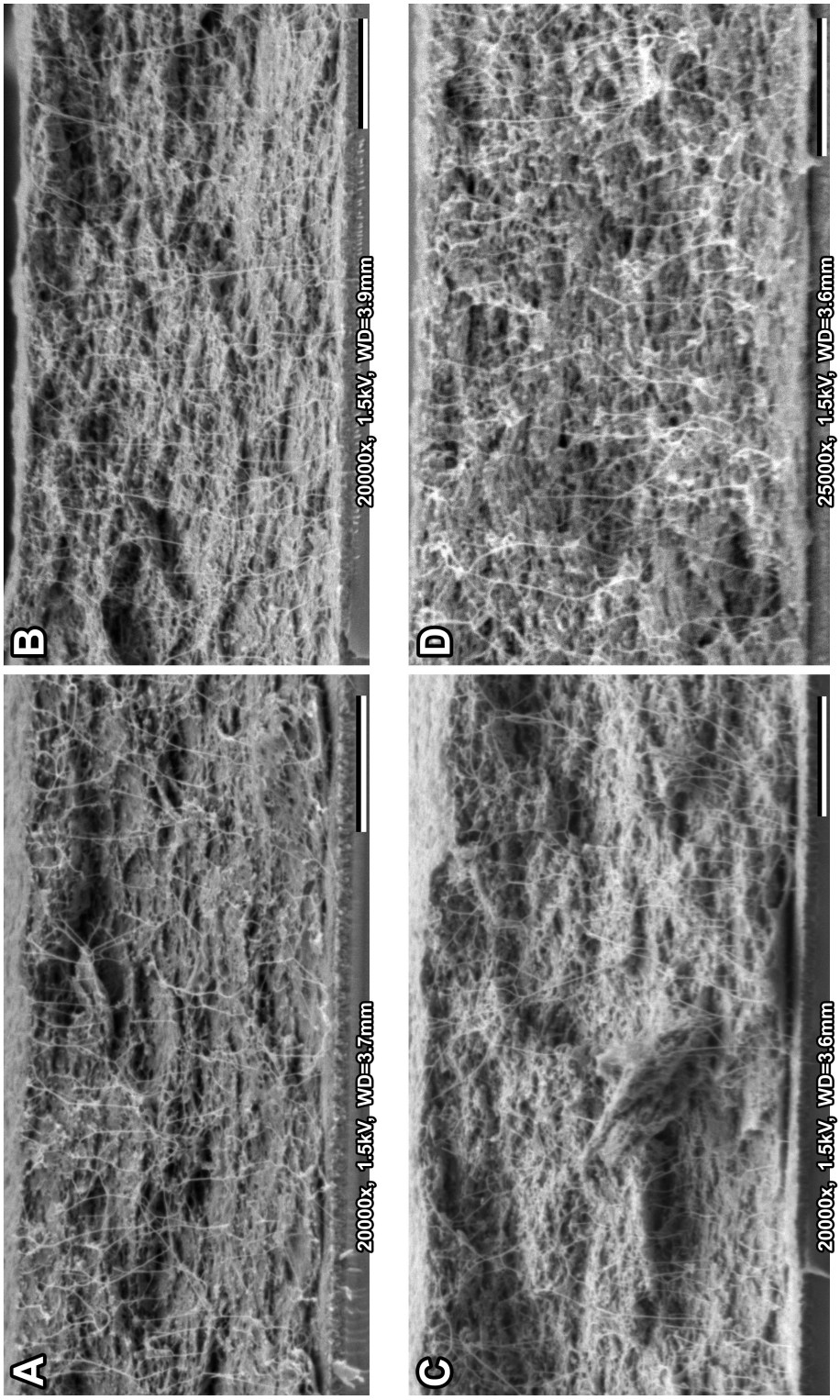

Figure 60 – (Rotated) Various SEM cross section images with 1 μm scale bars of EPD polymer coatings containing functionalized SWNT showing possible nanotube alignment. Magnification, acceleration voltage, and working distance are given under each image.

4.5.10 Section summary

It was proposed that protonating the polymer with a weak acid might eliminate the large voids in the coatings that were suspected to be caused by excess gas production at the electrode. A minimized amount of acetic acid was utilized and successfully yielded smooth coatings that were free of large voids, with the better quality coatings being produced from low concentration solutions. Coatings containing functionalized carbon nanotubes displayed much less agglomerated structures after the functionalization technique was slightly improved by a more efficient order of mixing and longer ultrasonication durations.

Control over coating thickness was demonstrated by producing thin and thick coatings of both pure polymer and nanotube-containing polymer. Practical upper and lower limits on coating thickness were discussed. The thinnest coatings demonstrated were below 100 nm in thickness while the thickest were approximately 10 μm, which is a difference of two full orders of magnitude. Producing a coating between the two extremes is simply a matter of adjusting the applied voltage, solution concentration, and tuning the duration of deposition.

Further control over thickness was demonstrated by producing a series of coatings to span the thickness range and the use of ITO substrates enabled the measurement of coating transparency as a function of incident wavelength. It was suggested that the maximum ideal coating thickness of this material for a solar cell device is approximately 400 nm due to no additional light absorption from the polymer in thicker coatings.

The deposition yield as a function of time was observed in real-time using a quartz crystal microbalance. Both the concentration and voltage was found to have a greater than linear affect on the deposition rate and the yield over the same time period. The shape of

the mass vs. time curves revealed 3 distinct stages of deposition. The starting stage is influenced by the applied voltage and represents the time needed to establish the conditions near the substrate that enable deposition. The middle stage is the linear portion of the mass vs. time curve where the deposition rate is constant. The end stage is the decline of the deposition rate due to the voltage drop across the accumulated coating resulting in the reduction of the electric field strength across the solution.

The ability to deposit multiple layers of different coatings was demonstrated. This technique could be used to improve coating performance or even enable additional niche applications of EPD.

The substrate-normal alignment of carbon nanotubes versus the false appearance of alignment due to the cross section specimen preparation technique was discussed. Some images clearly show that nanotubes are often pulled out of the matrix material as a result of the tension applied to the coating during the cleaving of the substrate into two pieces. Visual characteristics of both nanotube pulling and true nanotube alignment were identified. It was concluded that nanotube pulling is a major contributor to the appearance of alignment but it is plausible that some true alignment also occurs during electrophoresis and the subsequent deposition of polymer functionalized carbon nanotubes.

4.6 Photovoltaic Device Fabrication

4.6.1 Introduction

Polymer coatings containing polymer functionalized carbon nanotubes have been successfully deposited by electrophoretic deposition. The originally received material and initial EPD attempts barely yielded a visible deposit on the substrate but after many refinements the resulting coatings became relatively uniform, controllable, and reliable. This was achieved through developing an understand of the deposition mechanism, improvements in the choice of functional groups on the polymer side chains to become a weak polyelectrolyte, the switch to weak acid protonation, changes in the nanotube functionalization technique, the use of high ethanol to water ratios, and finding the ideal ranges for solute concentration, applied voltage, and deposition duration.

With the EPD coatings beyond the initial stages of development it was possible to spend some time considering one of the potential applications of the material and technique. Solar cells were the primary application intended for this material so the preliminary development of organic photovoltaic device fabrication was undertaken. The Xerox Research Center of Canada (XRCC) assisted with this application because of their interest and expertise in organic photovoltaic devices as well as their dedicated laboratory facilities to this field of research.

Some McMaster University graduate students spend a majority of their time at the XRCC facilities and they were willing to explain and demonstrate their device fabrication techniques and testing procedures. The knowledge of these techniques was then applied towards establishing customized procedures for device preparation at the main laboratory of the Adronov research group within the department of Chemistry & Chemical Biology

at McMaster University. Most of the device fabrication subsequently took place at McMaster University with the exception of the thermal evaporation deposition and the device testing which both utilized the XRCC laboratory facilities.

The organic photovoltaic device fabrication involves the following steps: Thorough cleaning of the ITO substrate, photolithography process to pattern the ITO substrate, spin coating of the PEDOT:PSS bottom buffer layer, deposition of the active layer, and the deposition of the top buffer layer (LiF or BCP) and aluminum electrode layer, both by thermal evaporation. These procedures were promptly followed by device testing using a solar simulator.

4.6.2 Device fabrication training

In order to learn the organic photovoltaic device fabrication process at XRCC a common bulk heterojunction device was made using P3HT:PCBM as the active layer. The ITO was prepared for the photolithography process, depicted in Figure 61, by applying the rigorous cleaning procedure described in the previous chapter. The first step of photolithography was to spin coat the square inch ITO tile with photoresist and soft bake it. The photoresist was then exposed to UV light through a mask in order to create a pattern and render the exposed area soluble in a developer solution. The coated ITO tile was then placed into a developer solution that removed the exposed photoresist while the part that was protected by the mask remained intact. The ITO tile was then hard baked to strengthen the remaining photoresist. Finally, it was etched in a strong acid solution to remove the uncovered ITO while the remaining photoresist protected underlying ITO. Following etching, the photoresist was removed using acetone and the ITO tile was cleaned. The resulting pattern, shown in the last drawing of Figure 61, consisted of four

separated ITO pads which can each be tested independently as a device and one strip of ITO at the top which is the location of the top electrode contact point in device testing.

The fabrication of the photovoltaic device on the patterned ITO tile consists of sequentially depositing the different layers on the substrate and using masking to control the deposit area. This process is depicted in Figure 62 and began with spin coating a layer of PEDOT:PSS within a specific area masked by scotch tape. Following a baking step, another mask was applied and the active layer was spin coated in a dry box from a warmed 20 $g \cdot L^{-1}$ solution of P3HT:PCBM (1:1) in chlorobenzene. After drying on a hot plate, another mask was applied and the tile was placed in the thermal evaporator which was pumped down to vacuum level. An ultra thin (5Å) buffer layer of LiF was then deposited over the active layer and followed by a 50 nm layer of aluminum for the top electrode, masked to resemble the last tile of Figure 62. After ten minutes of annealing at 140ºC in a vacuum oven the device was ready to be tested.

The mask positioning of the various layering steps was designed to prevent short circuits by ensuring that no layer can directly contact any device layer other than adjacent layers. The electrical current is therefore forced through every layer sequentially as depicted in Figure 63B.

The masking left the outer sides of the ITO islands exposed on each device for electrical contact to the base layer. Only one contact for the aluminum layer was necessary and it was located at the top, over the ITO strip that was electrically separated from the four devices by an etched trench. With the electrical testing setup depicted in Figure 63, the four devices could be tested independently since the solar lamp targets one device at a time and the contact to each device at the ITO electrode is also isolated exclusively to the specific device being tested.

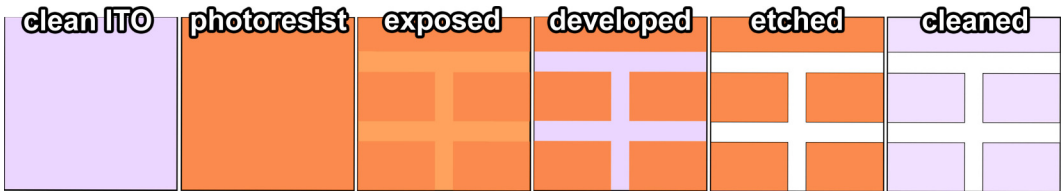

Figure 61 – The main stages of the photolithography process to pattern the ITO surface.

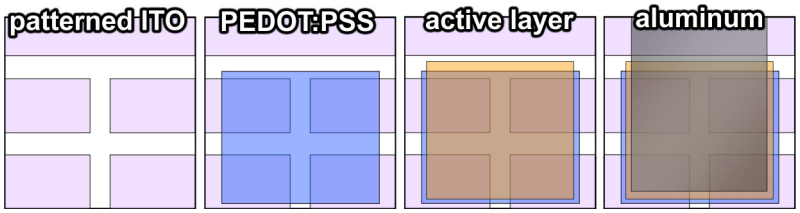

Figure 62 – The deposition of the various layers in an organic photovoltaic device.

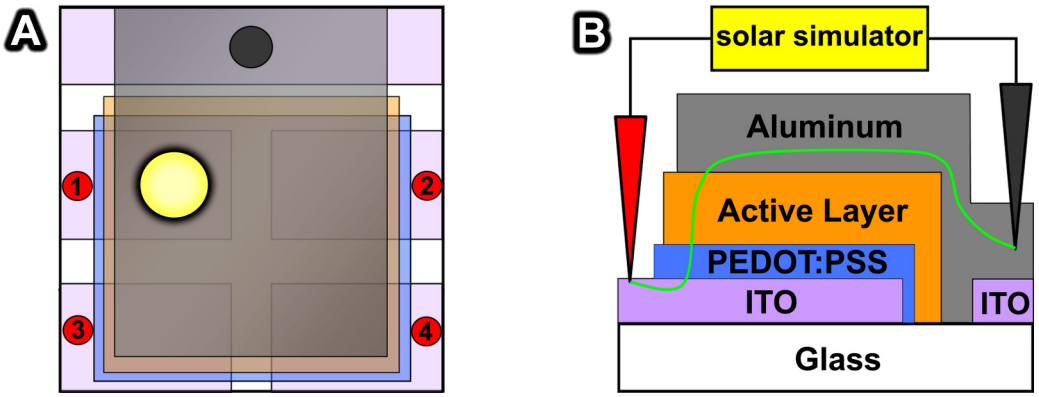

Figure 63 – A) Top view diagram showing ITO electrode contact points (red) for each of the four devices and the top metal electrode contact (black) on the aluminum at the top of the image. A controlled area of simulated sunlight is shown illuminating one device. B) Cross section diagram showing the electrical current pathway (green) through all the device layers of one device.

Each P3HT:PCBM device on the patterned ITO substrate was tested with the solar simulator to generate the current vs. voltage behaviour under simulated sunlight and in the dark. Figure 64 is a typical plot of the data from one of the devices, shown in the form of current density vs. voltage. The resulting average open circuit voltage (V_{OC}) across all devices was 0.54 V with an average fill factor of 0.56, and the average power conversion efficiency was calculated to be 1.45%. The difference between each device was small

with all the efficiencies within 10% of the average efficiency. Half the devices had the LiF buffer layer over the active layer while the other half did not. The performance between the two types was approximately the same considering the sample size was not large enough for small differences to be statistically significant. One of the roles of LiF is to extend the lifespan of the device, but this aspect was not tested.

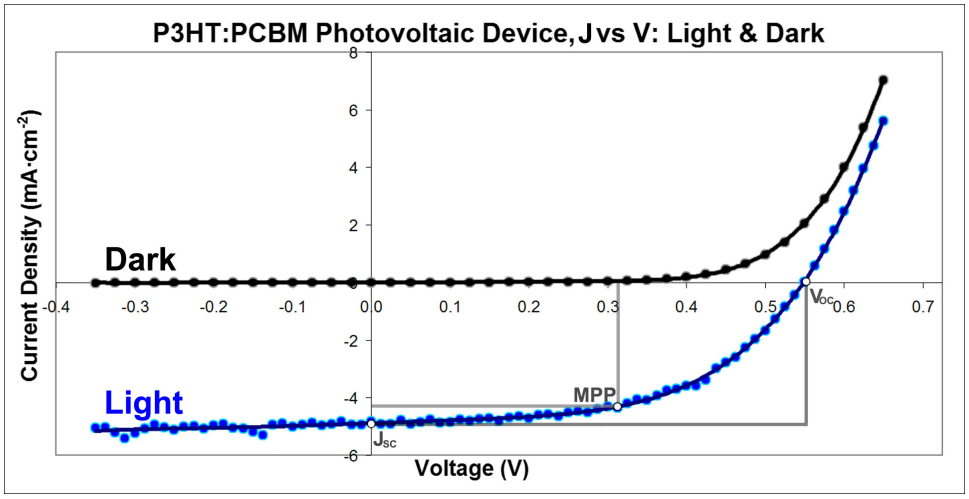

Figure 64 - Current Density vs. Voltage plot for the P3HT:PCBM photovoltaic device.

These P3HT:PCBM device results suggest that the fabrication procedure was performed well enough to produce a properly functioning device. This was noteworthy because the quality and even functionality of organic photovoltaic devices tends to be very sensitive to the procedure and to minor human error. The same techniques could then be applied to fabricate devices with the EPD polymer coatings containing polymer functionalized carbon nanotubes with some confidence in fabrication procedure competency.

4.6.3 Device layout adaptations

The first step towards adapting the photovoltaic device fabrication procedure to the EPD coatings was to attempt EPD of the active layer on the patterned substrate. A few

patterned ITO tiles were masked and spin coated with PEDOT:PSS to look like the second tile in Figure 62 and the tile was further masked with the intention of depositing the active layer with similar dimensions to the third tile in Figure 62. It was known that the EPD coating would not deposit on bare glass but it was not known whether the PEDOT:PSS layer was conductive enough to facilitate EPD. Copper tape was placed down the sides of the tile to establish electrical conductivity to the four ITO islands and the deposition conditions were 50 V for 2 min using a 0.25 $g \cdot L^{-1}$ solution, which typically produced high quality coatings.

The resulting coating was found to only deposit on the areas of PEDOT:PSS over top ITO, and repeated experiments produced the same result. To confirm the result, a plain glass slide was spin coated with PEDOT:PSS and attempts to deposit on it using EPD yielded no coating. The PEDOT:PSS layer was not conductive enough to enable EPD except when there was ITO directly underneath. Furthermore, the EPD coatings did not fully cover the entire ITO area because the pattern was too intricate and edge effects reduced coating quality. An illustration of the resulting EPD coating is shown in Figure 65A.

Even if the EPD coating quality over the four ITO islands could be perfected, the lack of an active layer in the gaps between the ITO islands was a major problem. In the locations without ITO underneath and without an active layer, the aluminum layer would directly contact the PEDOT:PSS and the device would be short circuited as illustrated in Figure 65B&C. It was clear that the four device configuration was not likely to be compatible with EPD.

To eliminate the short circuit that would occur between the PEDOT:PSS and aluminum in the gaps between the four ITO islands, the ITO patterning was simplified to

a one device per tile configuration as illustrated by the modified photolithography process shown in Figure 66. This larger device area and more simplified pattern also reduced the impact of EPD edge effect and resulted in a smooth coating, depicted in Figure 67A. However, it is still not possible to deposit the active layer beyond the edge of the ITO at the top trench and it is important to realize that the EPD coating does not form perfectly sharp edges. A short circuit is likely to leak through at this edge from the ITO or PEDOT:PSS to the aluminum as illustrated in Figure 67B&C by the red pathway.

The edge short can be completely eliminated by the addition of an electrically insulating barrier layer. This barrier, depicted in Figure 68 by the yellow strip along the trench edge, prevents the aluminum electrode from contacting anything other than the active layer. While it is possible to conceive of a barrier layer for the four-device configuration, this complicates the procedure and requires that the EPD coatings properly cover all four device areas without significant edge effects. For preliminary device purposes the single barrier layer was simply created by using a thin strip of scotch tape that was sliced with a razor blade on glass, but ideally it should be built into the fabrication process as a deposited thin film of an inert and insulating material. The major downside to adding a barrier layer is its large thickness because the aluminum layer above it needs to be continuous. A thick barrier strip creates a wall that the submicron aluminum layer must climb in order to maintain the electrical pathway and this can be problematic since thermal evaporation deposition tends to follow a linear path and tall objects can cast shadows that block deposition in some places.

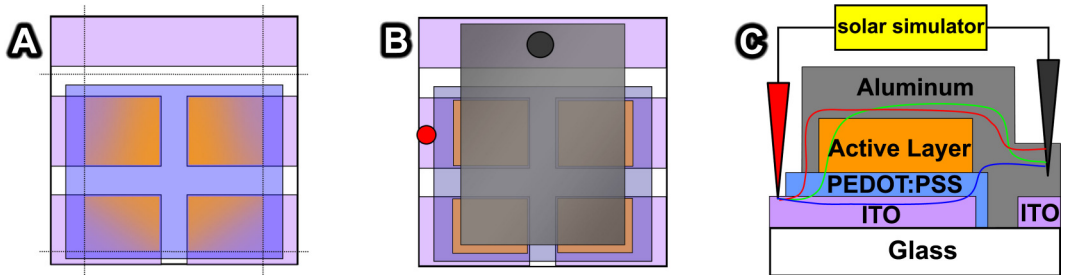

Figure 65 – Illustration of the EPD coating masked within the box bound by the dotted lines but only depositing on the PEDOT:PSS locations with ITO underneath (A). If the aluminum top electrode were to be deposited as in "B" there would be short circuits circumventing the active layer as depicted by the red and blue lines in "C" instead of the intended pathway (green line).

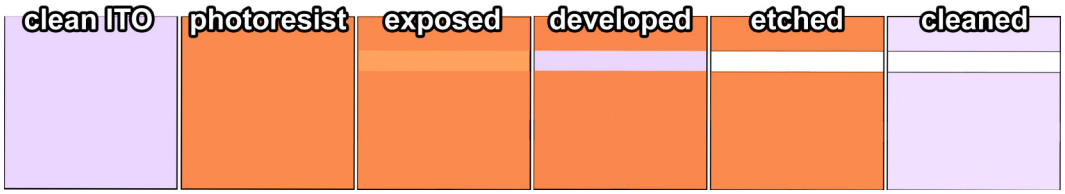

Figure 66 – The modified photolithography process for a one-device ITO tile configuration.

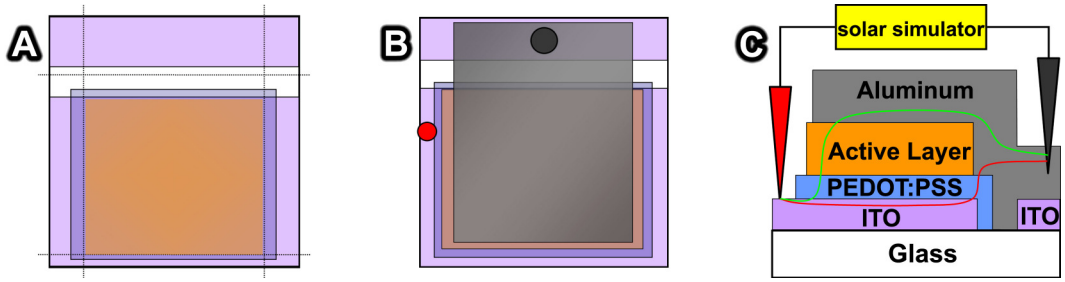

Figure 67 - Diagrams of the EPD coating on the simplified ITO tile (A) which eliminated the short circuit at the gaps between the four ITO islands. There is still a possible short at the top edge of the EPD layer (B) because it can not extend over the ITO edge, depicted by the red line in "C".

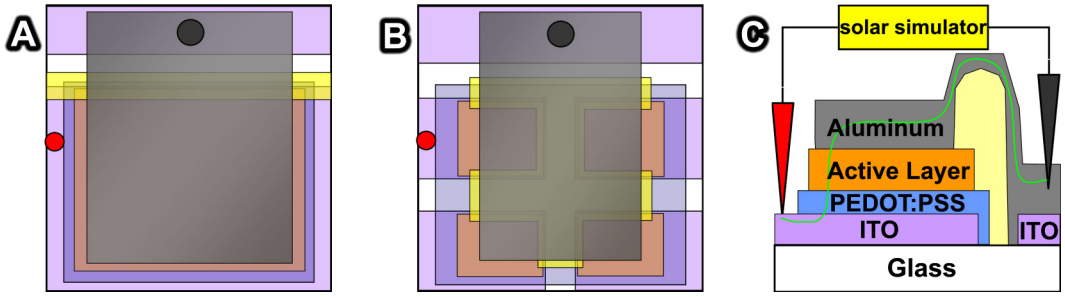

Figure 68 - Diagrams showing the addition of a barrier layer (yellow strip) at the active layer edge (A), and the resulting side view (C) showing only one possible circuit pathway. A four-device barrier configuration is also possible (B) but not practical for preliminary experimentation.

With the new device layout being theoretically functional, ITO tiles were etched to posses the one-device pattern, spin coated with PEDOT:PSS over a mask, and the active layer was deposited by EPD at 40 V for 2 min from a 0.125 $g \cdot L^{-1}$ solution in 96% ethanol. The substrate for each EPD session was a stainless steel base with the ITO tile firmly attached by copper tape to pass the electrical current to the ITO surface and scotch tape was used for the remainder of the masking. Six devices were prepared up to this point in the fabrication process with three using polymer containing functionalized nanotubes as the active layer and the other 3 using just the pure polymer. The resulting coatings were smooth and did not have any noticeable defects. After drying, the scotch tape barrier strip was applied and the tiles were then placed into a vacuum desiccator for transport to XRCC the following morning.

4.6.4 XRCC device fabrication and testing

At XRCC the best looking two out of three partially completed devices were selected to continue with the remaining fabrication steps. Both pure polymer and nanotube-containing types were prepared with and without the LiF layer. The deposition of the 5 Å LiF on the active layer for two devices occurred in one thermal evaporator while another one was utilized to deposit the aluminum. This second evaporator does not have in-situ measurement or precise control over the coating thickness but it was estimated that the aluminum coating was in the vicinity of 100 nm. When the devices with LiF were ready they were also coated with the aluminum electrode layer. Device testing with the solar simulator followed the fabrication.

During testing all the devices had problems with an incomplete and intermittent circuit. This was caused by the failure of the aluminum coating to fully connect over the tape barrier strip from the active layer area to the top contact pad on the other side of the

barrier. The thickness of scotch tape is in the vicinity of 50 μm, but the aluminum coating was only approximately 100 nm. This is a difference of 500x so the edge of the tape is thus a large wall for the aluminum to have to cover during deposition using only a linear vapor pathway. Attempts to salvage the devices involved gently placing copper tape over the aluminum at the tape edge in order to bridge the circuit gap but the results were very intermittent. Using a multimeter to test the resistance, often it would either show up as infinite which indicates the break in the electrical pathway, or it would be very low in the tens and low hundreds of ohms which indicates a short circuit. Even very light pressure on the copper tape was enough to penetrate the fragile sub-micron scale layers and contact the ITO layer. When a more appropriate resistance in the range of over tens thousand ohms was detected the devices were placed in the solar simulator tester.

All the devices that were able to be tested displayed an ohmic resistor characteristic in the I-V plot as a straight line through the origin with a positive slope. In the case of ohmic behavior the inverse of the slope of the I-V plot gives the resistance according to Ohm's law. Out of the three devices that were stable enough to attempt testing, the resistances from the plots were 280 Ω, 97 Ω, and 7900 Ω for the polymer device without LiF, the nanotube-containing device without LiF, and the polymer device with LiF respectively. A stable enough circuit to facilitate testing was not achieved with the nanotube-containing device with LiF. The first two resistances clearly indicate a short circuit from the top electrode straight to the ITO, likely caused by the attempts to establish a complete circuit with the copper tape. The third device with the 7900 Ω resistance is also likely a short because that is still low compared to typical resistances of polymer thin films but perhaps the short is simply less penetrating than the first two.

Due to the short circuits the testing of these devices did not provide any information about the photovoltaic properties of the device or even reliably indicate the resistance through the coating thickness. Additionally, nothing can be said about the differences between the four combinations of active layer material and the use of LiF.

4.6.5 Fabrication revision and testing

Two more partial devices were etched and prepared similarly to the previously described devices up to the EPD of the polymer functionalized nanotube active layer for the final attempt at XRCC the following day. Some revisions were made to the fabrication process to increase the likelihood of producing a functioning photovoltaic device. The 5 Å LiF layer was replaced with a 10 nm BCP layer. Since the standard size for a BCP layer is approximately 20x thicker than the standard LiF layer, it may provide better resistance to short circuiting. BCP is known to be an exciton and hole blocking layer and has been shown to improve the rectifying properties of the device. This was suspected to be an improvement in the device structure since there was no observed rectification in the devices that were previously discussed and only electrons should pass through to the aluminum electrode rather than holes and excitons.

The aluminum layer was also revised by switching to the slower thermal evaporator at the XRCC facilities because it enabled the use of more than one boat of source material and it also has a sensor to measure coating thickness. Two boats of pure aluminum material were loaded prior to the vacuum pump down and thermally deposited, one after the other. The resulting aluminum electrode layer was 320 nm, which is considerably thicker than the previous 100 nm and the typical 50 nm layer sizes. This much thicker layer was suspected to have a higher chance of being able to bridge the gap in the circuit at the tape barrier strip. At minimum it was likely to reduce the sensitivity to shorts

caused by handling, attempting to bridge the circuit gap with copper tape, and testing conductivity with a multimeter.

Following the deposition of the BCP and aluminum layers, the device was baked in a vacuum oven for 10 minutes at 100ºC. Annealing in this manner is fairly common practice for the organic solar cell researchers in the XRCC facility and has also been found by Kymakis and Amaratunga[66] to increase device performance in their P3OT:SWNT devices, apparently due to the increase in polymer crystallinity.

During testing it was found that one of the two devices contained a complete circuit, meaning the thicker aluminum layer successfully bridged the circuit over the tape barrier strip. The other device required the use of copper tape to bridge the connection but this time it was not as intermittent and the light pressure needed to apply the copper did not regularly cause spikes of low resistance. The switch to thicker top layers was therefore a useful revision and is recommended over the standard thicknesses. Adding a third boat of aluminum to the thermal evaporator to increase the thickness even more might further improve the success rate of obtaining a complete circuit.

From the solar simulator testing it was found that both devices behaved as resistors rather than photovoltaic devices. The I-V plots were again straight lines through the origin with a positive slope as shown in Figure 69. The resistances determined from the inverse of the slopes (averaged across four testing points each) were 850 Ω and 1380 Ω. Both these resistance values are too low for an organic solar cell so the devices likely contain a short circuit. This is also suggested by the fact that there was no significant difference between the electrical behaviour in the light vs. in the dark, and additionally because the device was non-rectifying.

With the improvements in the top electrode thickness it was not likely that the short circuit was a result of handling during testing as was suspected in the previous devices because of the need to manually bridge the gap over the barrier strip.

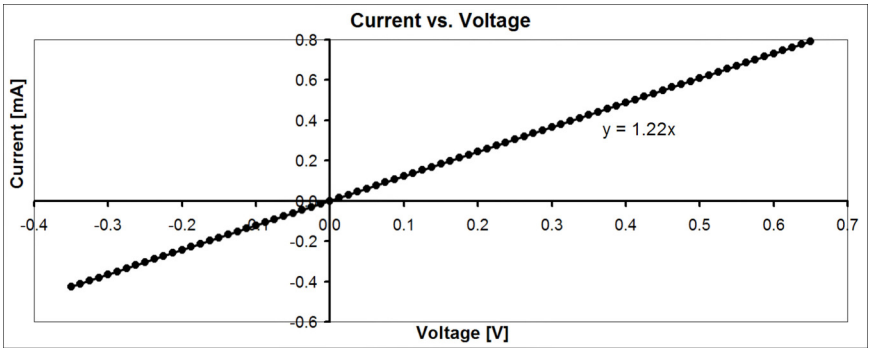

Figure 69 - A typical I-V plot from the non-functional photovoltaic device attempts.

4.6.6 Device cross section

With the expectation that it would reveal important information about possible flaws in the fabrication process, one of the attempted devices was prepared into an SEM specimen for cross sectional observation. The opposite side of the device was scored with a glass cutter followed by placing the device into a liquid nitrogen bath. The device was then fractured into pieces with care to avoid contacting the surface at the expected fracture area. The liquid nitrogen was used with the intention of making the fracture behaviour more brittle to preserve the layer morphology and create a sharp cross sectional cut. Unfortunately the fracture was not at all a clean break but there were enough useful pieces to continue with the microscopy.

Figure 70 is a typical SEM micrograph of the device cross section at a relatively sharp fracture surface. The layer thickness was determined by the average of measurements at multiple places over three similar images. The aluminum was 310 nm which is very close to the estimated thickness (320 nm) from the quartz crystal resonator sensor within the thermal evaporator. The BCP layer was too thin to measure with much

confidence due to the limits of SEM resolution and the lack of contrast compared to the polymer, but it appears to be approximately 15 nm which is close to the 10 nm estimated during deposition. The electrophoretically deposited layer of polymer and polymer functionalized carbon nanotubes was found to be approximately 360 nm, which is within the thickness range that was targeted when the deposition parameters were set. The PEDOT:PSS layer was not very uniform in thickness and the average was approximately 65 nm, which is below the expected value of roughly 100 nm. The ITO layer was found to average approximately 106 nm, which is normal.

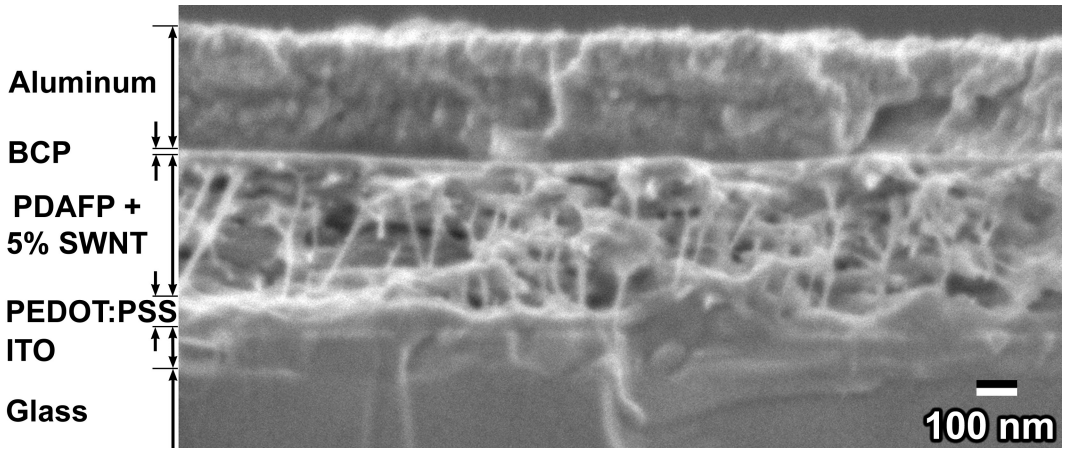

Figure 70 - SEM cross sectional micrograph of the attempted device. The image was captured at 50000x magnification using a 1.5 keV beam and 3.5 mm working distance. The layer thicknesses averaged over 3 similar images were 310 nm for aluminum, 15 nm for BCP, 360 nm for the electrophoretically deposited layer of polymer and SWNTs, 65 nm for the PEDOT:PSS, and the ITO coating was found to be approximately 106 nm.

4.6.7 Discussion of device performance

The failures of all the attempted photovoltaic devices with the active layer produced by EPD were most likely caused by short circuits. One of the indicators is that all of the devices were found to behave entirely as ohmic resistors without a trace of rectifying behaviour. Even in the dark, without a short circuit the device would still show some rectifying behaviour simply due to the electronic properties of the various layers which are meant to selectively control the flow of holes and electrons. When tested in the dark

the device should have had an I-V curve with a "hockey stick" shape showing nearly zero current in the reverse bias direction as in the P3HT:PCBM device of Figure 64.

Another short circuit indicator is the low resistance of all the attempted devices with values from one hundred ohms to less than ten thousand ohms. The resistance for a typical organic photovoltaic device from the ITO through the device layers to the aluminum is orders of magnitude higher. The successful P3HT:PCBM device that was created to learn the fabrication procedure had resistances in the 100 kΩ to 1000 kΩ range when probed with a multimeter.

Identifying the exact cause of the short circuit is a difficult task because there are many steps in the fabrication procedure that could be related to the cause. Additionally, it only takes one small place on the device to contain a pin hole short to ruin the whole device. This was one of the reasons the 4-island device construction used such small device areas and combining that area into one large device increases the risk of failure. An extensive series of additional device attempts would be necessary to make progress in identifying and eliminating short circuits in order to finally test the photovoltaic properties. Attempting this would have been well beyond time and resource limitations and also the limited duration contract with XRCC, but some potential sources of the short circuit problem can be identified.

The SEM cross section micrograph and measurements revealed a few concerns. Firstly, the PEDOT:PSS layer was thinner and also much less uniform in thickness than expected. A study by Friedel et. al.[120] determined that 70 nm was the optimum thickness of the PEDOT:PSS layer in an organic photovoltaic device to obtain the best photovoltaic properties and the result was independent of the material chosen for the active layer. The 65 nm average thickness of the PEDOT:PSS layer in the attempted device is therefore

close to the published optimum but there is significant variation in the thickness with some thin places below 40 nm. The cause of the non-uniform PEDOT:PSS layer might not be from the spin coating step itself but the EPD of the active layer that followed. PEDOT:PSS is water-soluble so perhaps some of it dissolved during EPD in the initial stage of deposition before it was fully covered by the electrophoretically deposited material. To combat this effect, the PEDOT:PSS layer could be spin coated with a higher target thickness in the range of 100-150 nm. This extra thickness would also help to counter any shorts that are caused by highly conductive carbon nanotubes poking through the PEDOT:PSS towards the ITO interface. It should be noted that the optimum thickness of 70 nm from the Friedel study was not tested in situations where the active layer contains long and highly conductive species such as carbon nanotubes where a thicker PEDOT:PSS layer might be more appropriate.

The morphology of the active layer is another concern revealed from the SEM results. The carbon nanotubes appear to span the entire thickness of the layer and with metallic nanotubes this could be a cause of low shunt resistance and even a short circuit. While the presence of true vertically aligned nanotubes is debatable and has been previously discussed, even in a completely random distribution of nanotube orientations there would be many nanotubes that are oriented perpendicular to the substrate. The fact that they are long enough to span the entire thickness is a problem that likely needs to be addressed in future work with this material. While the absorbance spectroscopy results suggested that there would be no gain in photon absorption for an active layer thickness above 400 nm, there could be some benefit to exceeding this thickness in order to increase the shunt resistance.

Another option that could be explored is to chemically shorten the carbon nanotubes prior to functionalization which would increase the percolation threshold and reduce the likelihood of a chain of metallic nanotube spanning the entire active layer thickness. Nanotube shortening typically involves the use of strong acids which leave defects in the molecular structure and also adds carboxyl groups to the defect sites. While the carboxyl groups increase solubility they may affect the polymer functionalization process and it is also important to remember that the presence of defects has a negative impact on the electronic properties of the nanotubes. Despite these concerns, the use of shortened nanotubes is common and the positive benefits may outweigh the negatives.

The use of semiconducting carbon nanotubes without the metallic chirality could also help to improve the shunt resistance through the active layer and to eliminate metallic short circuit paths. Methods of separation often involve chemical functionalization or attachment of nanoparticles and these modifications could have an impact on the polymer functionalization required in this application. The yield of such nanotube chirality separation is typically low, so to produce a useful yield of semiconducting nanotubes would require a significant investment in research and experimentation time. They can also be commercially purchased but the isolation of the semiconducting nanotubes is not widely commercialized at the moment and high purity semiconductor nanotubes can cost hundreds of dollars per milligram which is approximately 1000x the cost of regular SWNTs. While perhaps useful in the long term, the short term practicality of this option is probably too low to immediately consider.

The problems with long nanotubes and a rough PEDOT:PSS layer could also be mitigated by the addition of another layer. After the spin coating of the PEDOT:PSS layer and prior to the deposition of the active layer, a thin layer of pure polymer could be

deposited to prevent carbon nanotubes from directly contacting the PEDOT:PSS layer. The layer should significantly reduce the current of electrons traveling in the reverse bias direction, thus increasing rectification. If it is thin enough it should not have harmful effects on the device, assuming the polymer behaves properly as a p-type conjugated polymer, because only separated holes need to travel through it. This layer would need to be very thin because of the low conductivity of the polymer and because excitons generated within the layer would need to reach a carbon nanotube surface for charge separation to occur and this is limited by the exciton diffusion distance. The thickness of this pure polymer layer would likely be optimal in the range of 20-30 nm. To achieve such a thin coating with EPD would require a relatively low solution concentration with the applied voltage being at the bottom of the ideal voltage range and a short duration. An estimate for these deposition conditions is 35 V from a 0.1 $g \cdot L^{-1}$ solution concentration for 20 seconds.

There are a few other steps in the device fabrication process that could contribute towards the proliferation of a short circuit. The various baking and annealing treatments were based on practices that have been found to be effective in the fabrication of other organic photovoltaic devices but were not specifically tested for optimization with this scenario. It is not known what the optimal baking conditions are for each layer or whether any of them could have an unexpected detrimental affect. Also, while unlikely, one of the other steps in the fabrication process could be an unknown source of the problem and would be difficult to uncover without addressing all the suggested potential problem sources first.

4.6.8 Section summary

The main goal within the limited time of the device fabrication experiments was to develop and adapt procedures to fabricate a photovoltaic device using an active layer composed of electrophoretically deposited polymer and polymer functionalized carbon nanotubes. This was achieved by first learning the fabrication procedures that were utilized at XRCC in order to build a functioning organic photovoltaic device with an active layer composed of P3HT:PCBM.

It was found that the procedures required modifications to fit the needs of an electrophoretically deposited active layer. The EPD coating did not deposit on PEDOT:PSS without ITO underneath which would result in a short circuit. The ITO photolithography process was modified from the four device configuration to one device in order to eliminate the short. There was also a less obvious short at the top edge because the EPD coating will not extend beyond the ITO. This was addressed by the addition of a thin strip of scotch tape to act as an insulating barrier layer to cover the edge.

During device testing it was found that the barrier layer caused a break in the circuit because the thin aluminum electrode was unable to form a continuous path over the barrier. Attempts to repair the connection with copper tape were only partially effective and had a tendency to short circuit the device. This was addressed by increasing the aluminum layer thickness by a factor of approximately three. Additionally, the top buffer layer was switched from the ultra thin 5 Å LiF to 10 nm BCP in an attempt to improve device rectification. The increased aluminum thickness was found to increase the success rate of obtaining a complete circuit and it was recommended that further increasing the thickness would be beneficial. Unfortunately the devices remained non-functional and

behaved entirely as ohmic resistors with no rectifying behaviour and relatively low resistance values.

The cause of the device failure was most likely a short circuit and this was indicated by the lack of rectification, no difference between light and dark behaviour, and very low resistance measured between the opposite electrodes. The exact origin of the short circuit would not be identifiable without extensive investigation but the most likely potential causes were discussed.

SEM micrographs of the device cross section showed that the PEDOT:PSS layer was thin and non-uniform, which may be a symptom of degradation during the active layer deposition. It was suggested that the PEDOT:PSS thickness should be significantly increased. The SEM also revealed that the carbon nanotubes in the active layer appear to span the entire layer. Many of the nanotubes are metallic so this is a potential cause of a short circuit or at least a very low shunt resistance and it is a concern even if the nanotube orientation is completely random.

It was suggested that increasing the active layer thickness could help to increase the shunt resistance. Shortening the carbon nanotubes prior to functionalization was also recommended to increase the percolation threshold and reduce the possibility of metallic nanotube chains spanning the entire thickness. The use of high purity semiconducting carbon nanotubes would also be beneficial but not likely to be a practical solution in the short term. The addition of a very thin pure polymer layer deposited by EPD between the PEDOT:PSS and the active layer was suggested as a way to prevent the nanotubes from directly contacting the bottom electrode and to block electron transport in the reverse bias direction.

5. Conclusion and Recommendations

5.1 Conclusion

The electrophoretic deposition of soluble conjugated polymer functionalized carbon nanotubes from non-toxic solvents was achieved through an iterative process of experimentation and technique refinement. The initial attempts with both cationic and anionic strong polyelectrolyte material yielded poor quality deposits. The strong functional group was then replaced with a weak polyelectrolyte to utilize the high pH in the vicinity of the cathode in order to cause the polymer to become neutrally charged and insoluble. Using a strong acid to protonate the polymer was found to cause crater-like voids in the coating morphology due to the presence of bubbles attached to the coating surface during deposition. These voids were eliminated by switching to protonation with a minimized amount of weak acid because the combination of the low dissociation constant and Le Châtelier's principle resulted in very little excess ionic contribution to the solution. The coating quality was further improved by modifying the functionalization procedure which resulted in less agglomerated particles.

Throughout the EPD experimentation it was found that there is a range of applied voltages that create the best quality coatings and the range shifts upward to higher voltages when the solution concentration is lower. Smoother coatings were also produced with lower concentration solutions, and higher ethanol:water ratios.

Control over coating thickness was demonstrated by producing coatings that spanned the range of 100 nm to 10 μm. These coatings were produced by adjusting the applied voltage, solution concentration, and tuning the duration of deposition. The maximum ideal thickness of this electrophoretically deposited material in terms of photon absorption

in the active layer of a photovoltaic device was found with absorption spectroscopy to be approximately 400 nm.

Quartz crystal microbalance testing revealed that the concentration and voltage were found to have a greater than linear affect on the deposition rate and yield. The data also revealed that there appears to be three distinct stages of deposition that can be described in terms of the starting, middle, and ending behaviour. The length of the starting stage is voltage dependent and is the time to establish the conditions in the solution that enable deposition. The middle stage is a constant deposition rate. The ending stage is the decline in deposition rate due to the reduction in field strength across the solution caused by the voltage drop over the increasing thickness of the deposited coating.

With the electrophoretically deposited coatings of conjugated polymer and functionalized carbon nanotubes being refined to the point of appropriate coating quality and demonstrated control, the final objective was undertaken. The EPD coatings were applied to the active layer in a solid organic photovoltaic device. This required the modification through multiple iterations of general procedures to fabricate organic photovoltaic devices to fit the needs of the EPD technique and specific coating materials. The major modifications were the adaptation of fabrication procedures from the Xerox Research Center of Canada to the laboratory of the Adronov group at McMaster University, the redesign of the ITO etching pattern, the addition of an insulating barrier strip, the thickening of the aluminum layer, and the switch from LiF to BCP for the top buffer layer.

While the devices did not function during testing, the problem was identified as a short circuit. Several possible causes of the short were identified and several potential improvements were recommended: Increase the active layer thickness, shorten the

nanotubes prior to functionalization, increase the PEDOT:PSS layer thickness, insert a thin pure polymer layer between the PEDOT:PSS and active layer, and use only semiconducting carbon nanotubes if possible.

This research of this thesis was conducted with the intention of filling gaps in the literature by combining the materials of conjugated polymers and carbon nanotubes with the fields of electrophoretic deposition and organic solar cells. This unique combination of materials, technique, and application contributes towards expanding the applications of electrophoretic deposition and the advancement of organic solar cell technology. It also enables further investigations in these fields that may some day help our society become more environmentally sustainable.

5.2 Recommendations for Future Experimentation

The advances within this thesis have enabled at least three new paths for continued experimentation that are each the appropriate project scale for a masters or doctorate degree.

The first recommendation for future work is a deeper study into the electrophoretic deposition of the soluble conjugated polymer, PDAFP, and deposition of carbon nanotubes functionalized with the polymer. Further investigations could attempt to conclusively verify some of the explanations for various phenomena that were provided as probable reasons but not absolutely proven. A more thorough characterization of the deposition process and resulting coatings would be required using techniques such as electrochemical testing, additional QCM experimentation, conductivity measurements, transmission electron microscopy (TEM) to investigate the nanoscale structure, energy dispersive x-ray spectroscopy (EDX) or electron energy loss spectroscopy (EELS) to

learn more about elemental distribution and electronic states, and SEM would continue to be a valuable analysis tool.

More variables could be introduced to the deposition process to examine their effects on the resulting coatings such as the temperature of solution during deposition, the ratio of carbon nanotubes to the polymer, the length of the carbon nanotubes (via chemical shortening), the distance between the electrodes, and post-deposition practices such as accelerated drying and annealing methods.

Additional EPD techniques could be attempted such as constant current mode, pulsed DC deposition, and asymmetric wave AC deposition. Pulsed DC and asymmetric AC EPD have been demonstrated to reduce bubble formation in water with ceramic material.[121, 122] These techniques might be appropriate to reduce the size of the nanoscale pores within these polymer coatings and also to reduce the ethanol:water ratio or even eliminate the need for ethanol.

The second recommendation for future work is advancing the photovoltaic device fabrication that was initiated in this thesis. The first milestone would be to understand exactly why the attempted device did not function and then to solve the underlying problems in order to create a functioning solar cell. A good place to start is by investigating the suggestions that were proposed in the previous chapter: active layer thickness, nanotubes length, PEDOT:PSS layer thickness, addition of a thin pure polymer layer, and the use of high semiconducting purity nanotubes.

Beyond achieving a working device is the optimization of the materials and techniques in order to increase the power conversion efficiency. Device optimization would involve testing many variants of the active layer EPD step such as varying the nanotube concentration, nanotube length, and active layer thickness. Other gains in

efficiency may be obtained by optimizing the thickness of all the other layers, selection of the most ideal buffer layer materials, and perhaps even utilizing different electrophoretic deposition techniques. There is some synergy between this and the previous recommendation and both projects would benefit from some forms of discussion and collaboration.

The third recommendation for future work is to apply the techniques of EPD and photovoltaic device fabrication towards a different polymer from the four in Figure 24 that are intended to be eventually combined into one device for broad absorption capability. The best choice of polymer for experimentation is probably P3 because it closely resembles the polythiophene derivatives P3HT and P3OT that are among the most widely used polymers for organic solar cells at the moment. In addition, based on the predicted absorption peak of P3 it would likely appear deep blue or purple which may help when diagnosing coating quality by visual inspection compared to the somewhat transparent P1 variant that was used in this thesis.

Combination with the polymer used in this project (PDAFP) could involve co-deposition and multilayered deposition experiments. This could be applied to photovoltaic devices as the first step towards increasing the absorption range by utilizing two polymers with different absorption properties. If the deposition of P3 is successful without much variation from the techniques developed within this thesis, perhaps P2 and P4 from Figure 24 could also be adapted into the process. This project might be most effectively pursued after the first two recommendations have been undertaken in order to accelerate the process of adapting the new polymers to well established procedures.

In addition to those three main paths, some unanswered questions and new ideas have arisen that might be appropriate for smaller scale research such as that of a senior undergraduate thesis or the work of a summer research student.

It would be beneficial to find out whether the EPD process contributes to the device failure and this could be tested by temporarily removing the EPD process from the system. Using the same organic photovoltaic device procedure that led to a working device with a spin coated P3HT:PCBM active layer, a PDAFP:SWNT device could be attempted using spin coating. Preliminary spin coating attempts were unsuccessful due to the high surface tension and low vapor pressure of the ethanol-water solution and also because the concentration of solute was far too low. The spin coating process consumes a large amount of material because most of it flows off the substrate. It was therefore not investigated with highly concentrated solutions due to quantity limitations of the polymer and because even the saturated 6 $g \cdot L^{-1}$ concentrated polymer stock solution is still low concentration compared to the 20 $g \cdot L^{-1}$ solution of P3HT:PCBM that was used for spin coating. Perhaps higher concentrations can be achieved using other organic solvents that also have a low surface tension and high vapor pressure.

Further investigation could involve substituting PCBM for the carbon nanotubes. A PDAFP:PCBM mixture could be spin coated into the active layer of a photovoltaic device in order to test the viability of the polymer without convoluting the results with the viability of the carbon nanotubes. PCBM is a reliable electron acceptor material that is commonly used in organic solar cell literature.

Similarly, perhaps a mixture of P3HT and SWNTs could be spin coated if P3HT (or a slight variant of P3HT) can be used to functionalize the SWNTs to impart solubility. If this combination is possible then it could be a way to test the validity of functionalized

SWNTs as an electron acceptor separately from PDAFP and the EPD process. These spin coating device experiments could help to determined if the PDAFP, SWNTs, or the EPD process caused device failure by swapping multiple unknown variables for those that have been proven to function successfully.

Another alternative experiment with a similar purpose would be to attempt the electrophoretic deposition of a known photovoltaic polymer such as PH3T. The successful deposition would likely require a functional group modification to become a weak polyelectrolyte similar to what was done in the work of this thesis. If this is achievable then the next step would be to attempt to functionalize fullerenes with a weak polyelectrolyte or to also attach a weak electrolyte functional group to the fullerenes. If co-deposition of these two materials is successful, a photovoltaic device could be created to compare electrophoretic deposition with spin coating in absence of the materials used in this thesis because they have relatively unknown photovoltaic performance characteristics.

The exact nature of the polymer and polymer functionalized carbon nanotubes in solution is difficult to observe but there is a characterization technique available at the Canada Center for Electron Microscopy (CCEM) facilities that can enable this observation. Cryo-microscopy TEM can be used to prepare a thin sample of a rapidly frozen solution to study the morphology of the species within the solution. This technique could help to identify whether the carbon nanotubes are fully separated as individual nanotubes or whether they still persist in small bundles while functionalized. It could also provide information about how the macromolecules interact and the amount of natural agglomeration in solution. This type of information about the solution can help to further understand the EPD mechanism as well as the morphology of the deposited coatings.

The possible alignment of carbon nanotubes within the EPD coatings was discussed and the observation of true alignment was deemed inconclusive without additional investigation. The problem lies in the fact that when the coating is cleaved to produce a cross section specimen for SEM, the tension within the coating during the fracture causes nanotubes to be pulled out of the polymer matrix. They subsequently tend to hang in the same direction giving the appearance of nanotube alignment. If the tensile forces can be eliminated from the specimen preparation then the occurrence of true nanotube alignment can be verified. Also available at the CCEM, a focused ion beam (FIB) integrated into an SEM can cleanly expose a cross section without using any mechanical forces. Additionally, the machine can remove a thin cross section slice to prepare a TEM specimen if desired. The ion beam at its typical operating voltage is quite damaging to carbon-based materials thus it is suggested to use the much slower low voltage settings in order to preserve the morphology of the materials along the section cut. While some imaging can be done with the ion beam, it is suggested to block the beam and to instead use the secondary electron imaging system at similar conditions to the SEM data displayed in this thesis.

The reduction of ITO to metal was observed during EPD when it was used as a bare cathode counter electrode. However, it is unknown whether reduction also occurs when ITO is the cathodic substrate and that could potentially be a problem if it is the case. The substrate is uncoated during the start phase of deposition and even when the coating has been established it contains nanoscale pores that would allow ions to reach the substrate. These factors suggest that some ITO reduction might be possible during cathodic deposition. No visual signs of reduction were observed such as a grey color change, but that does not rule out small amounts of reduction or the reduction of indium atoms from

the +3 state to the +2 or +1 states. Analytical TEM techniques such as EELS could be used to detect the electronic states of the indium atoms in the ITO layer. This would conclusively verify whether the reduction of ITO takes place when it is used as a cathodic substrate during EPD. This information has consequences for device fabrication because reduced ITO is deemed deactivated and is less effective. A large amount of deactivation could prompt the need for development of an anionic version of the weak polyelectrolyte polymers so that the deposition on an ITO substrate can take place as an anode instead, which would eliminate the problem.

6. References

1. Bernstein L, Bosch P, Canziani O, Chen Z, Christ R, Davidson O, Hare W, Huq S, Karoly D, Kattsov V, Kundzewicz Z, Liu J, Lohmann U, Manning M, Matsuno T, Menne B, Metz B, Mirza M, Nicholls N, Nurse L, Pachauri R, Palutikof J, Parry M, Qin D, Ravindranath N, Reisinger A, Ren J, Riahi K, Rosenzweig C, Rusticucci M, Schneider S, Sokona Y, Solomon S, Stott P, Stouffer R, Sugiyama T, Swart R, Tirpak D, Vogel C, Yo G. Climate change 2007: Synthesis report - summary for policymakers. Valencia, Spain: Intergovernmental Panel on Climate Change. November 2007.
2. Working Group I. TS.6.1 changes in human and natural drivers of climate. IPCC Fourth Assessment Report: Climate Change 2007: Working Group I: The Physical Science Basis. Intergovernmental Panel on Climate Change; 2007.
3. Working Group I. FAQ 2.1 how do human activities contribute to climate change and how do they compare with natural influences? IPCC Fourth Assessment Report: Climate Change 2007: Working Group I: The Physical Science Basis. Intergovernmental Panel on Climate Change; 2007.
4. Working Group II. Summary of main findings. IPCC Fourth Assessment Report: Climate Change 2007: Climate Change 2007: Working Group II: Impacts, Adaption and Vulnerability. Intergovernmental Panel on Climate Change; 2007.
5. Working Group III. Executive summary. IPCC Fourth Assessment Report: Climate Change 2007: Working Group III: Mitigation of Climate Change. Intergovernmental Panel on Climate Change; 2007.
6. Green MA, Emery K, Hishikawa Y, Warta W. Solar cell efficiency tables (version 35). Prog Photovoltaics Res Appl 2010;18(2):144-50.
7. Shockley W, Queisser HJ. Detailed balance limit of efficiency of p-n junction solar cells. Journal of Applied Physics 1961;32(3):510-9.
8. Sanchez P, Fernandez B, Menendez A, Pereiro R, Sanz-Medel A. Pulsed radiofrequency glow discharge optical emission spectrometry for the direct characterisation of photovoltaic thin film silicon solar cells. J Anal at Spectrom 2010;25(3):370-7.
9. Green MA. Consolidation of thin-film photovoltaic technology: The coming decade of opportunity. Prog Photovoltaics Res Appl 2006;14(5):383-92.
10. - Morhardt JE, - Claremont McKenna College. Roberts Environmental Center. - Global climate change and natural resources : Summaries of the 2007-2008 scientific literature. .
11. Denholm P, Margolis RM. Evaluating the limits of solar photovoltaics (PV) in traditional electric power systems. Energy Policy 2007;35(5):2852-61.
12. Barnham KWJ, Mazzer M, Clive B. Resolving the energy crisis: Nuclear or photovoltaics? Nature Materials 2006;5(3):161-4.
13. Denholm P, Margolis RM. Evaluating the limits of solar photovoltaics (PV) in electric power systems utilizing energy storage and other enabling technologies. Energy Policy 2007;35(9):4424-33.

14. Dennler G, Sariciftci NS. Flexible conjugated polymer-based plastic solar cells: From basics to applications. Proc IEEE 2005 08;93(8):1429-39.

15. Hoppe H, Sariciftci NS. Organic solar cells: An overview. J Mater Res 2004;19(7):1924-45.

16. Pradhan B, Batabyal SK, Pal AJ. Functionalized carbon nanotubes in donor/acceptor-type photovoltaic devices. Appl Phys Lett 2006;88(9).

17. Tasis D, Tagmatarchis N, Bianco A, Prato M. Chemistry of carbon nanotubes. Chem Rev 2006;106(3):1105-36.

18. Casagrande T, Imin P, Cheng F, Botton GA, Zhitomirsky I, Adronov A. Synthesis and electrophoretic deposition of single-walled carbon nanotube complexes with a conjugated polyelectrolyte. Chemistry of Materials 2010;22(9):2741-9.

19. Sgobba V, Guldi DM. Carbon nanotubes as integrative materials for organic photovoltaic devices. Journal of Materials Chemistry 2008;18(2):153-7.

20. Rowell MW, Topinka MA, McGehee MD, Prall H, Dennler G, Sariciftci NS, Hu L, Gruner G. Organic solar cells with carbon nanotube network electrodes. Appl Phys Lett 2006;88(23).

21. Benanti TL, Venkataraman D. Organic solar cells: An overview focusing on active layer morphology. Photosynthesis Res 2006 01;87(1):73-81.

22. Nelson J. The physics of solar cells. Imperial College Press; 2003. 2005271257.

23. Photovoltaic principles. Elsevier; 2002. Compilation and indexing terms, Copyright 2011 Elsevier Inc.; M1: Compendex; T3: Physica E: Low-Dimensional Systems and Nanostructures.

24. Solar energy conversion. Physics of sustainable energy; 1-2 March 2008; USA: AIP; 2008. M1: Copyright 2009, The Institution of Engineering and Technology; T3: AIP Conf. Proc. (USA).

25. Hoertz PG, Staniszewski A, Marton A, Higgins GT, Incarvito CD, Rheingold AL, Meyer GJ. Toward exceeding the shockley-queisser limit: Photoinduced interfacial charge transfer processes that store energy in excess of the equilibrated excited state. J Am Chem Soc 2006;128(25):8234-45.

26. Green M, Wenham S, Ho J. Australian research council photovoltaics center of excellence: Annual report 2007. Sydney, Australia: The University of New South Wales; 2007.

27. Green MA. Third generation photovoltaics: Ultra-high conversion efficiency at low cost. Prog Photovoltaics Res Appl 2001;9(2):123-35.

28. Vic Physics - Australian Institute of Physics (Vic Branch) Education Committee [Internet] [cited 2010 . Available from: http://www.vicphysics.org/documents/events/stav2005/spectrum.JPG.

29. Design constraints of the quantum-dot intermediate band solar cell. Elsevier; 2002. Compilation and indexing terms, Copyright 2009 Elsevier Inc.; M1: Compendex; T3: Physica E: Low-Dimensional Systems and Nanostructures.

30. Quantum dot solar cells. Elsevier; 2002. Compilation and indexing terms, Copyright 2011 Elsevier Inc.; M1: Compendex; T3: Physica E: Low-Dimensional Systems and Nanostructures.

31. Solanki CS, Beaucarne G. Advanced solar cell concepts. Energy for Sustainable Development 2007;11(3):17-23.

32. Bosi M, Pelosi C. The potential of III-V semiconductors as terrestrial photovoltaic devices. Prog Photovoltaics Res Appl 2007;15(1):51-68.

33. Shah A, Torres P, Tscharner R, Wyrsch N, Keppner H. Photovoltaic technology: The case for thin-film solar cells. Science 1999;285(5428):692-8.

34. Spectrolab Inc. Triple-junction terrestrial concentrator solar cells. 2000.

35. Cowie JMKG, Arrighi V. Polymers: Chemistry and physics of modern materials. CRC Press; 2008. 2007005187.

36. Bredas JL, Street GB. Polarons, bipolarons, and solitons in conducting polymers. Acc Chem Res 1985 10/01;18(10):309-15.

37. Cao G, Brinker CJ. Annual review of nano research. World Scientific; 2008. .

38. Sirringhaus H, Brown PJ, Friend RH, Nielsen MM, Bechgaard K, Langeveld-Voss B, Spiering AJH, Janssen RAJ, Meijer EW, Herwig P, de Leeuw DM. Two-dimensional charge transport in self-organized, high-mobility conjugated polymers. Nature 1999;401(6754):685-8.

39. Kaiser AB. Electronic transport properties of conducting polymers and carbon nanotubes. Reports on Progress in Physics 2001 01;64(1):1-49.

40. Moliton A, Hiorns RC. Review of electronic and optical properties of semiconducting - conjugated polymers: Applications in optoelectronics. Polym Int 2004;53(10):1397-412.

41. Djurišić AB, Kwong CY. Chapter 20: The influence of the electrode performance of organic solar cells. In: S. S. Sun, N. S. Sariciftci, editors. Organic photovoltaics: Mechanism, materials, and devices. Taylor \& Francis; 2005. 2004059378.

42. Scholes GD, Rumbles G. Excitons in nanoscale systems. Nature Materials 2006;5(9):683-96.

43. Scully SR, Armstrong PB, Edder C, Frechet JMJ, McGehee MD. Long-range resonant energy transfer for enhanced exciton harvesting for organic solar cells. Adv Mater 2007;19(19):2961-6.

44. Chamberlain GA. Organic solar cells: A review. Solar Cells 1983 02;8(1):47-81.

45. Tang CW. Two-layer organic photovoltaic cell. Appl Phys Lett 1986 01/13;48(2):183-5.

46. Gunes S, Neugebauer H, Sariciftci NS. Conjugated polymer-based organic solar cells. Chem Rev 2007;107(4):1324-38.

47. Xue J, Rand BP, Uchida S, Forrest SR. Mixed donor-acceptor molecular heterojunctions for photovoltaic applications. II. device performance. J Appl Phys 2005;98(12):1-9.

48. Hong ZR, Liang CJ, Sun XY, Zeng XT. Characterization of organic photovoltaic devices with indium-tin-oxide anode treated by plasma in various gases. J Appl Phys 2006;100(9).

49. Xue J, Forrest SR. Carrier transport in multilayer organic photodetectors: II. effects of anode preparation. J Appl Phys 2004 02/15;95(4):1869-77.

50. Zhang F, Inganäs O. Chapter 21: Conduction and transparent polymer electrodes. In: S. S. Sun, N. S. Sariciftci, editors. Organic photovoltaics: Mechanism, materials, and devices. Taylor \& Francis; 2005. 2004059378.

51. Brabec CJ, Shaheen SE, Winder C, Denk P, Serdar S, N. Effect of LiF/metal electrodes on the performance of plastic solar cells. Appl Phys Lett 2002;80(7):1288-.

52. Gommans H, Verreet B, Rand BP, Muller R, Poortmans J, Heremans P, Genoe J. On the role of bathocuproine in organic photovoltaic cells. Advanced Functional Materials 2008 11/24;18(22):3686-91.

53. Veenstra SC, Loos J, Kroon JM. Nanoscale structure of solar cells based on pure conjugated polymer blends. Prog Photovoltaics Res Appl 2007;15(8):727-40.

54. Matsumura M, Osasa T, Matsui Y, Matsumura T. Determination of photo-active region in organic thin film solar cells with an organic heterojunction. Solar Energy Mater Solar Cells 2006 11/23;90(18-19):3136-42.

55. Tandem-type organic solar cells by stacking different heterojunction materials. ICMAT 03, december 7, 2003 - december 12; 2003; Elsevier; 2005. Compilation and indexing terms, Copyright 2011 Elsevier Inc.; M1: Compendex; T3: Thin Solid Films.

56. Terrones M, Hsu WK, Kroto HW, Walton DRM. Nanotubes: A revolution in materials science and electronics. In: Fullerenes and related structures. Heidelberg: Springer Berlin; 1999. .

57. Ajayan PM. Nanotubes from carbon. Chem Rev 1999;99(7):1787-99.

58. Endo M, Strano MS, Ajayan PM. Potential applications of carbon nanotubes. Top Appl Phys 2008:13-61.

59. Hirsch A. Functionalization of single-walled carbon nanotubes. Angew Chem Int Ed 2002;41(11):1853-9.

60. Star A, Stoddart JF, Steuerman D, Diehl M, Boukai A, Wong EW, Yang X, Chung S, Choi H, Heath JR. Preparation and properties of polymer- wrapped single-walled carbon nanotubes. Angew Chem Int Ed 2001;40(9):1721-5.

61. Cheng F, Imin P, Maunders C, Botton G, Adronov A. Soluble, discrete supramolecular complexes of single-walled carbon nanotubes with fluorene-based conjugated polymers. Macromolecules 2008;41(7):2304-8.

62. Foroutan M, Nasrabadi AT. Investigation of the interfacial binding between single-walled carbon nanotubes and heterocyclic conjugated polymers. J Phys Chem B 2010;114(16):5320-6.

63. Kymakis E, Amaratunga GAJ. Single-wall carbon nanotube/conjugated polymer photovoltaic devices. Appl Phys Lett 2002 01/07;80(1):112-14.

64. Kymakis E, Alexandrou I, Amaratunga GAJ. High open-circuit voltage photovoltaic devices from carbon-nanotube-polymer composites. J Appl Phys 2003;93(3):1764-8.

65. Kymakis E, Amaratunga GAJ. Carbon nanotubes as electron acceptors in polymeric photovoltaics. Reviews on Advanced Materials Science 2005;10(4):300-5.

66. Kymakis E, Koudoumas E, Franghiadakis I, Amaratunga GAJ. Post-fabrication annealing effects in polymer-nanotube photovoltaic cells. Journal of Physics D (Applied Physics) 2006 03/21;39(6):1058-62.

67. Rud JA, Lovell LS, Senn JW, Qiao Q, Mcleskey Jr. JT. Water soluble polymer/carbon nanotube bulk heterojunction solar cells. J Mater Sci 2005;40(6):1455-8.

68. Kazaoui S, Minami N, Nalini B, Kim Y, Hara K. Near-infrared photoconductive and photovoltaic devices using single-wall carbon nanotubes in conductive polymer films. J Appl Phys 2005;98(8):1-6.

69. Heeger AJ, Parker ID, Yang Y. Carrier injection into semiconducting polymers: Fowler-nordheim field-emission tunneling. Synth Met 1994;67(1-3):23-9.

70. Landi BJ, Raffaelle RP, Castro SL, Bailey SG. Single-wall carbon nanotube-polymer solar cells. Prog Photovoltaics Res Appl 2005 03;13(2):165-72.

71. Patyk RL, Lomba BS, Nogueira AF, Furtado CA, Santos AP, Mello RMQ, Micaroni L, Hummelgen IA. Carbon nanotube-polybithiophene photovoltaic devices with high open-circuit voltage. Physica Status Solidi - Rapid Research Letetrs 2007;1(1):R43-5.

72. Liang Y, Xu Z, Xia J, Tsai S, Wu Y, Li G, Ray C, Yu L. For the bright future-bulk heterojunction polymer solar cells with power conversion efficiency of 7.4%. Adv Mater 2010;22(20):E135-8.

73. Besra L, Liu M. A review on fundamentals and applications of electrophoretic deposition (EPD). Prog Mater Sci 2007;52(1):1-61.

74. Zhitomirsky I. Cathodic electrodeposition of ceramic and organoceramic materials. fundamental aspects. Adv Colloid Interface Sci 2002;97(1-3):279-317.

75. Zhitomirsky I. Electrophoretic deposition of organic-inorganic nanocomposites. J Mater Sci 2006;41(24):8186-95.

76. Zhitomirsky I, Petric A. Cathodic electrodeposition of polymer films and organoceramic films. Materials Science and Engineering B: Solid-State Materials for Advanced Technology 2000;78(2-3):125-30.

77. Zhitomirsky I, Niewczas M, Petric A. Electrodeposition of hybrid organic-inorganic films containing iron oxide. Mater Lett 2003;57(5-6):1045-50.

78. Tada K, Onoda M. Nanostructured conjugated polymer films by electrophoretic deposition. Advanced Functional Materials 2002;12(6-7):420-4.

79. Preparation and application of nanostructured conjugated polymer film by electrophoretic deposition. 5th international conference on nano-molecular electronics; 08/22; Switzerland: Elsevier; 2003. M1: Copyright 2003, IEE; T3: Thin Solid Films (Switzerland).

80. Tada K, Onoda M. Uniform film of conjugated polymer for light-emitting device by electrophoretic deposition. J Phys D 2008;41(3).

81. Tada K, Onoda M. Preparation of donor–acceptor nanocomposite through electrophoretic deposition. Current Applied Physics 2005;5(1):5-8.

82. Tada K, Onoda M. Nanostructured conjugated polymer films for electroluminescent and photovoltaic applications. Thin Solid Films 2005 04/22;477(1-2):187-92.

83. Tada K, Onoda M. Electrophoretic deposition of conjugated polymer: Deposition from dilute solution and PEDOT coating effect. Synth Met 2009 05;159(9-10):851-3.

84. Tada K, Onoda M. High material efficiency found in electrophoretic deposition of conjugated polymer. J Phys D 2009;42(17).

85. Tada K, Onoda M. Preparation of nanostructured conjugated polymer films from suspension-based technique and their applications. Thin Solid Films 2006 03/21;499(1-2):19-22.

86. Du C, Heldbrant D, Pan N. Preparation and preliminary property study of carbon nanotubes films by electrophoretic deposition. Mater Lett 2002;57(2):434-8.

87. Yamaguchi S, Yabutsuka T, Hibino M, Yao T. Development of novel bioactive composites by electrophoretic deposition. Materials Science & Engineering: C (Materials for Biological Applications) 2009 06/01;29(5):1584-8.

88. Barazzouk S, Hotchandani S, Vinodgopal K, Kamat PV. Single-wall carbon nanotube films for photocurrent generation. A prompt response to visible-light irradiation. J Phys Chem B 2004;108(44):17015-8.

89. Single wall carbon nanotube scaffolds for photoelectrochemical solar cells. capture and transport of photogenerated electrons. 2540 Olentangy River Road, P.O. Box 3337, Columbus, OH 43210-3337, United States: American Chemical Society; 2007. Compilation and indexing terms, Copyright 2011 Elsevier Inc.; M1: Compendex; T3: Nano Letters.

90. Kamat PV, Thomas KG, Barazzouk S, Girishkumar G, Vinodgopal K, Meisel D. Self-assembled linear bundles of single wall carbon nanotubes and their alignment and deposition as a film in a dc field. J Am Chem Soc 2004;126(34):10757-62.

91. Cho J, Konopka K, Rozniatowski K, Garcia-Lecina E, Shaffer MSP, Boccaccini AR. Characterisation of carbon nanotube films deposited by electrophoretic deposition. Carbon 2009;47(1):58-67.

92. Gao B, Yue GZ, Qiu Q, Cheng Y, Shimoda H, Fleming L, Zhou O. Fabrication and electron field emission properties of carbon nanotube films by electrophoretic deposition. Adv Mater 2001;13(23):1770-3.

93. Lima MD, De Andrade MJ, Bergmann CP, Roth S. Thin, conductive, carbon nanotube networks over transparent substrates by electrophoretic deposition. Journal of Materials Chemistry 2008;18(7):776-9.

94. Du C, Heldebrant D, Pan N. Preparation of carbon nanotubes composite sheet using electrophoretic deposition process. J Mater Sci Lett 2002 04/01;21(7):565-8.

95. Umeyama T, Fujita M, Tezuka N, Kadota N, Matano Y, Yoshida K, Isoda S, Imahori H. Electrophoretic deposition of single-walled carbon nanotubes covalently modified with bulky porphyrins on nanostructured SnO2 electrodes for photoelectrochemical devices. Journal of Physical Chemistry C 2007;111(30):11484-93.

96. Pieta P, Venukadasula GM, D'Souza F, Kutner W. Preparation and selected properties of an improved composite of the electrophoretically deposited single-wall carbon nanotubes, electrochemically coated with a C60-pd and polybithiophene mixed polymer film. Journal of Physical Chemistry C 2009;113(31):14046-58.

97. Casagrande T, Lawson G, Li H, Wei J, Adronov A, Zhitomirsky I. Electrodeposition of composite materials containing functionalized carbon nanotubes. Materials Chemistry & Physics 2008;111(1):42-9.

98. Grandfield K, Sun F, FitzPatrick M, Cheong M, Zhitomirsky I. Electrophoretic deposition of polymer-carbon nanotube-hydroxyapatite composites. Surf Coat Technol 2009 02/25;203(10-11):1481-7.

99. Bai Y, Neupane MP, Il SP, Lee MH, Tae SB, Watari F, Uo M. Electrophoretic deposition of carbon nanotubes-hydroxyapatite nanocomposites on titanium substrate. Materials Science & Engineering: C (Materials for Biological Applications) 2010 08/30;30(7):1043-9.

100. Boccaccini AR, Cho J, Subhani T, Kaya C, Kaya F. Electrophoretic deposition of carbon nanotube-ceramic nanocomposites. Journal of the European Ceramic Society 2010;30(5):1115-29.

101. Wu DC, Shen L, Low JE, Wong SY, Li X, Tjiu WC, Liu Y, He CB. Multi-walled carbon nanotube/polyimide composite film fabricated through electrophoretic deposition. Polymer 2010;51(10):2155-60.

102. Cho J, Schaab S, Roether JA, Boccaccini AR. Nanostructured carbon nanotube/TiO2 composite coatings using electrophoretic deposition (EPD). Journal of Nanoparticle Research 2008;10(1):99-105.

103. Itoh E, Suzuki I, Miyairi K. Field emission from carbon-nanotube-dispersed conducting polymer thin film and its application to photovoltaic devices. Japanese Journal of Applied Physics, Part 1 (Regular Papers, Short Notes & Review Papers) 2005 01;44(1):636-40.

104. Kanazawa KK, Melroy OR. The quartz resonator: Electrochemical applications. IBM Journal of Research and Development 1993;37(2):157-71.

105. Princeton Applied Research. QCM922 quartz crystal microbalance. Amtek 2009.

106. Srivastava AK, Sakthivel P. Quartz-crystal microbalance study for characterizing atomic oxygen in plasma ash tools. Journal of Vacuum Science and Technology A: Vacuum, Surfaces and Films 2001;19(1):97-100.

107. Dielectric constant of some common liquids [Internet]: The Engineering ToolBox [cited 2011 . Available from: http://www.engineeringtoolbox.com/liquid-dielectric-constants-d_1263.html.

108. Damodaran R, Moudgil BM. Electrophoretic deposition of calcium phosphates from non-aqueous media. Colloids Surf Physicochem Eng Aspects 1993;80(2-3):191-5.

109. Wikipedia. Surface tension values --- wikipedia, the free encyclopedia. 2009.

110. Electrochemical Redox Potential [Internet]; c2010 [cited 2011 . Available from: http://issuu.com/time-to-wake-up/docs/electrochemical_redox_potential.

111. Monk PMS, Man CM. Reductive ion insertion into thin-film indium tin oxide (ITO) in aqueous acidic solutions: The effect of leaching of indium from the ITO. J Mater Sci : Mater Electron 1999 04;10(2):101-7.

112. Zhitomirsky I, Petric A. Electrolytic deposition of zirconia and zirconia organoceramic composites. Mater Lett 2000 10;46(1):1-6.

113. Boccaccini AR, Biest O, Talbot JB, Electrochemical Society. Electrodeposition Division, United Engineering Foundation. Electrophoretic deposition, fundamentals and applications: Proceedings of the international symposium. Electrochemical Society; 2002. 2002116898.

114. Sarkar P, Nicholson PS. Electrophoretic deposition (EPD): Mechanisms, kinetics, and application to ceramics. J Am Ceram Soc 1996;79(8):1987-2002.

115. Quale SL, Talbot JB. Electrophoretic deposition of substrate-normal-oriented single-walled carbon nanotube structures. J Electrochem Soc 2007;154(8):K25-8.

116. Boccaccini AR, Shaffer MSP, Cho J, Roether JA, Thomas BJC, Minay EJ. Electrophoretic deposition of carbon nanotubes. Carbon 2006 12;44(15):3149-60.

117. Jin YW, Jung JE, Park YJ, Choi JH, Jung DS, Lee HW, Park SH, Lee NS, Kim JM, Ko TY, Lee SJ, Hwang SY, You JH, Ji-Beom Yoo, Chong-Yun Park. Triode-type field emission array using carbon nanotubes and a conducting polymer composite prepared by electrochemical polymerization. J Appl Phys 2002 07/15;92(2):1065-8.

118. Yamamoto K, Akita S, Nakayama Y. Orientation of carbon nanotubes using electrophoresis. Jpn J Appl Phys Part 2 Letter 1996;35(7):L917-8.

119. Ohshima H. Electrophoretic mobility of a cylindrical colloidal particle in a salt-free medium. J Colloid Interface Sci 2002;255(1):202-7.

120. Friedel B, Keivanidis PE, Brenner TJK, Abrusci A, McNeill CR, Friend RH, Greenham NC. Effects of layer thickness and annealing of PEDOT:PSS layers in organic photodetectors. Macromolecules 2009;42(17):6741-7.

121. Besra L, Uchikoshi T, Suzuki TS, Sakka Y. Bubble-free aqueous electrophoretic deposition (EPD) by pulse-potential application. J Am Ceram Soc 2008;91(10):3154-9.

122. Neirinck B, Fransaer J, Biest OVd, Vleugels J. Aqueous electrophoretic deposition in asymmetric AC electric fields (AC-EPD). Electrochemistry Communications 2009;11(1):57-60.